Fundamental Charge Transfer and Utilization Processes of CdS Photoanodes for Photoelectrochemical Hydrogen Production from H_2O and H_2S Splitting

by

Elif Öykü ALAGÖZ

A Dissertation Submitted to the
Graduate School of Sciences and Engineering
in Partial Fulfillment of the Requirements for
the Degree of

Master of Science

in

Chemistry

KOÇ
ÜNİVERSİTESİ

August 2023

Fundamental Charge Transfer and Utilization Processes of CdS Photoanodes for Photoelectrochemical Hydrogen Production from H_2O and H_2S Splitting

Koç University

Graduate School of Sciences and Engineering

This is to certify that I have examined this copy of a master's thesis by

Elif Öykü Alagöz

and have found that it is complete and satisfactory in all respects,
and that any and all revisions required by the final
examining committee have been made.

Committee Members:

Assoc. Prof. Sarp Kaya (Advisor)

Assoc. Prof. Damla Eroğlu Pala

Assist. Prof. Pınar Aydoğan Göktürk

Date: August 8, 2023

Biricik annem Gülten'e

Ve çok erken kaybettiğim canım babam İlhan'a

ABSTRACT

Fundamental Charge Transfer and Utilization Processes of CdS Photoanodes for Photoelectrochemical Hydrogen Production from H_2O and H_2S Splitting

Elif Öykü Alagöz

Master of Science in Chemistry

August 2023

Photoelectrochemical (PEC) green hydrogen production is one of the most important clean energy technologies as an efficient, facile, and promising approach to produce green hydrogen which is a carbon neutral, storable, and transportable alternative to fossil fuels. There are different reactions which are utilized for hydrogen production and the most important one is H_2O splitting as a non-toxic and available source. Another very important, yet less studied reaction is H_2S splitting which is a thermodynamically less hindered process than H_2O. However, its applications remained unconsidered due to experimental difficulties and its high toxicity. H_2S is a very critical subject for refinery industry, and it will be even more important as green hydrogen production gains more attention. Over time, serious consequences of global warming and the rising energy demand of the society have initiated extensive research on semiconductor materials that can be utilized as photoelectrodes. Among all, CdS is suitable as a photoanode for solar to hydrogen energy conversion because of its narrow bandgap, suitable band-edge alignment for H_2O and H_2S splitting half reactions, and facile fabrication. However, it suffers from photocorrosion and instability due to surface charge recombination. Extensive PEC characterization studies showed that improving hole extraction and utilization on the CdS surface is crucial for efficient PEC conversion. So far, the research on CdS was more focused on modifying it with different materials to benefit from its superior qualities rather than understanding the reasons behind activity loss.

In this dissertation, the fundamental charge carrier dynamics at photoanode/electrolyte interface and possible pathways for light-induced deactivation of pristine CdS were studied in detail by using transient photocurrent (TPC) measurements. H_2O and H_2S were used as hydrogen sources. For the H_2O splitting, we showed that hexadecyltrimethylammonium bromide (CTAB) coordinated to surface sulfur vacancies facilitates the charge separation and utilization by passivating the electron trapping on the surface. Tuning the surface characteristics of the CdS photoanodes with the CTAB diminished the surface hole accumulation and increased the injection efficiency from 0.61 to 0.99 at 1 V by a surface passivation mechanism where Br^- of CTAB occupies surface sulfur vacancies and acts like a hole-extracting layer on the CdS surface, passivates the surface charge recombination, and improves efficiency.

Secondly, atomic layer deposition (ALD) was used to deposit a thin layer of TiO_2 on CdS surface, which can be used to suppress electron trapping. Although ultrathin passivation overlayers are well-known for their positive effect on PEC activity of photoelectrodes, TiO_2 on CdS is an inefficient way to passivate charge trapping according to the findings of this study. In fact, it exhibited negative effect on PEC water splitting activity especially with high overlayer thickness. We used X-ray photoelectron spectroscopy (XPS) and energy dispersive X-ray spectroscopy (EDX) to monitor the TiO_2 overlayer growth and investigated the surface, optical and crystal structure properties by UV-vis spectroscopy and X-ray diffraction (XRD) analysis. Chronoamperometry (CA) measurements at different potentials were used to investigate the change in TPC behavior with different TiO_2 overlayer thickness.

For the H_2S splitting, we tested bare and TiO_2 modified CdS photoanodes and analyzed the stability and charge transfer processes by using surface sensitive and PEC characterization methods such as the XPS, CA and TPC in H_2S feeded alkaline electrolyte. The stability and PEC activity of CdS were rather promising in the presence of H_2S considering its poor stability in H_2O splitting. After providing an electron trapping mechanism for CdS where surface sulfur vacancies and light-induced S^{2-} dissolution play an important role in the deactivation process, H_2S feeded electrolyte was found to have a recovery effect for CdS photocorrosion. Furthermore, TiO_2 overlayers showed a reversed effect in H_2S splitting by increasing the photocurrent density of bare CdS by 53% at 0.8 V.

This work might be an important contribution for further studies on CdS and other photoelectrodes to enhance the understanding of charge utilization processes at photoanode-electrolyte interfaces by providing a detailed and systematic analysis of the charge carrier dynamics.

ÖZETÇE

H_2O ve H_2S Ayrıştırması ile Fotoelektrokimyasal Hidrojen Üretimi için CdS Fotoanotların Temel Yük Transferi ve Kullanım Süreçleri

Elif Öykü Alagöz

Kimya, Yüksek Lisans

Ağustos 2023

Fotoelektrokimyasal (PEC) yeşil hidrojen üretimi, fosil yakıtlara karbon nötr, depolanabilir ve taşınabilir bir alternatif olan yeşil hidrojen üretmek için verimli, kolay ve gelecek vaat eden bir yaklaşım olarak en önemli temiz enerji teknolojilerinden biridir. Hidrojen üretimi için kullanılan farklı reaksiyonlar vardır ve en önemlisi toksik olmayan ve erişilebilir bir kaynak olarak su ayrıştırmasıdır. Bir başka çok önemli, ancak daha az çalışılan reaksiyon, termodinamik olarak H_2O'dan daha az zorlu bir reaksiyon olan H_2S ayrıştırmasıdır. Ancak deneysel zorluklar ve yüksek toksisite nedeniyle uygulamaları gereken ilgiyi görmemiştir. H_2S rafineri endüstrisi için çok kritik bir konudur ve yeşil hidrojen üretimi daha fazla ilgi gördükçe o da daha çok önem kazanacaktır. Zamanla küresel ısınmanın ciddi sonuçları ve ciddi sonuçları ve toplumun artan enerji talebi, fotoelektrot olarak kullanılabilen yarı-iletken malzemeler üzerinde kapsamlı araştırmaları başlattı. Bunların arasında CdS, dar bant aralığı, H_2O ve H_2S ayrıştırma yarı reaksiyonları için uygun bant-kenar hizalanması ve kolay üretimi nedeniyle güneşten hidrojene enerji dönüşümü için bir fotoanot olarak uygundur. Bununla birlikte yüzey yük rekombinasyonu nedeniyle fotokorozyon ve istikrarsızlıktan müzdariptir. Şimdiye kadar, CdS üzerine yapılan araştırmalar, aktivite kaybının arkasındaki nedenleri anlamaktan çok, üstün niteliklerinden faydalanmak için onu farklı malzemelerle modifiye etmeye odaklanmıştı.

Bu tezde fotoanot/elektrolit arayüzündeki temel yük taşıyıcı dinamikleri ve bozulmamış CdS'nin ışık kaynaklı deaktivasyonu için olası yollar, geçici fotoakım (TPC) ölçümleri kullanılarak ayrıntılı olarak incelenmiştir. Hidrojen kaynağı olarak H_2O ve H_2S kullanılmıştır. H_2O ayrıştırması için, yüzeydeki kükürt boşluklarına koordine edilen hekzadesiltrimetilamonyum bromürün (CTAB), yüzeydeki electron yakalamayı pasifleştirerek yük ayrılmasını ve kullanımını kolaylaştırdığını gösterdik. CdS fotoanotlarının yüzey özelliklerinin CTAB ile ayarlanması, yüzeyde pozitif delik birikimini azalttı ve CTAB'in Br^- bileşeninin yüzey kükürt boşluklarını doldurduğu ve

bir pozitif delik çıkarıcı katman gibi davrandığı bir yüzey pasivasyon mekanizması ile 1 V'de enjeksiyon verimliliğini 0.61'den 0.99'a yükseltti, yüzey yük rekombinasyonunu azalttı ve yüzeyi pasifleştirdi.

İkinci olarak, electron yakalamayı bastırmak için kullanılabilecek başka bir hafif yüzey işleme yöntemi sağlamak için CdS yüzeyi üzerinde incre bir TiO2 tabakası biriktirmek için atomik katman biriktirme (ALD) kullanıldı. Ultra ince pasivasyon üst katmanları, PEC aktivitesi üzerindeki olumlu etkileriyle bilinmesine ragmen, CdS üzerindeki TiO_2'nin yük yakalamayı pasifleştirmenin verimsiz bir yolu olduğu kanıtlanmıştır. Aslında, özellikle yüksek üst tabaka kalınlığı ile PEC aktivitesi üzerinde olumsuz bir etkiye sahiptir. TiO_2 üst katman büyümesini izlemek için XPS, raman spektroskopisi ve enerji dağılımlı X-ışını spektroskopisi kullandık ve UV spektroskopisi ve X-ışını kırınımı (XRD) ile optic, kristal yapı ve yüzey özelliklerini Analiz ettik. Farklı TiO_2 üst katman kalınlığı ve TPC davranışındaki değişikliği araştırmak için farklı potansiyellerde kronoamperometri (CA) ölçümleri kullanıldı.

H_2S ayrıştırması için TiO_2 ile modifiye edilmiş CdS numunelerini test ettik, CdS'nin H_2S beslemeli alkalin alektrolit içindeki geliştirilmiş stabilitesini analiz etmek için XPS ve kronoamperometri (CA) sonuçlarını analiz ettik. CdS'nin istikrarı ve PEC aktivitesi, H_2O ayrıştırmasındaki zayıf istikrarı dikkate alındığında, H_2S varlığında oldukça umut vericiydi. Yüzey kükürt boşluklarının ve ışıkla indüklenen S^{2-} çözünmesinin deaktivasyon sürecinde önemli bir rol oynadığı CdS için bir electron yakalama mekanizması sağladıktan sonra, H_2S ile beslenen elektrolitin CdS fotokorozyonu için bir geri kazanım etkisine sahip olduğu bulundu. Ayrıca TiO_2 üst katmanları, bozulmamış CdS'nin fotoakım yoğunluğunu 0.8 VRHE'de %53 arttırarak H_2S bölünmesinde ters bir etki göstermiştir.

Bu çalışma, yük taşıyıcı dinamiklerinin ayrıntılı ve sistematik bir analizini sağlayarak fotoanot/elektrolit arayüzlerinde yük kullanım süreçlerinin anlaşılmasını geliştirmek için CdS ve diğer yarı iletken fotoelektrotlar üzerine yapılacak daha ileri çalışmalar için önemli bir katkı olabilir.

AKNOWLEDGEMENTS

I cannot believe that two years have passed that quickly. When I look back, I can clearly say that it was the most important two years of my life. When I first started, I remember that I had so many worries about coming to a new environment, working with people that I do not know at all. Now I am leaving with so many good memories and amazing friends.

Firstly, I would like to thank my advisor, my mentor Prof. Sarp Kaya who has an extremely important impact in my academic journey. Besides his academic contribution during my master's, I am extremely thankful that I have worked with a kind and good-hearted person which is very difficult to find at the early stages of your career. I really appreciate that he was always very supportive when things get bad or unexpected. Thank you hocam, for always trusting me and making me a confident person about my research. As a person who can easily get demotivated, I had many ups and downs during these two years, and I don't know how I would survive without your guidance and continuous support. I am more than happy that I have learnt not only the science of photo-electrochemistry from you but also academic ethics and working discipline. Your hardworking and dedication to your job will always be an inspiration to me for the rest of my academic career.

We were one of the most crowded labs in the school and I am more than thankful that I met the most amazing people here, all contributed to the joyful working environment we had in the lab. I am so grateful for everyone I met here, both in our lab and the neighbour lab in KUTEM. I would like to mention my special thanks for Dr. Hamaneh Zarenezhad, aka Hana the queen, my project supervisor who treated me like a sister always. She was not only a colleague but like a sister to me too. I really appreciate that she was also one of my references for my PhD applications. Saeede Tafazoli my food buddy, I hope to visit you for our Amsterdam lahmacun date, thank you for being so supportive all the time and coming to lunch with me no matter what time I ask :D

Emrecim, you are the best mentor any newcomer student can ever wish for. I am sooo lucky that I have learnt the fundamentals of photo-electrochemistry from an expert like you. More important than that, you are one of the kindest, most gentlemen people I know, and I am so grateful to have a friend like you to work with.

Amin joon, even the idea of saying goodbye to you makes me burst into tears but here we are. You are the most kind-hearted, smartest, most creative person in this world,

and I think no one who worked with you would disagree with that. I am extremely thankful that I was blessed with a friend like you here and I hope I was a good friend to you too. I can write many more things but let me put it this way, every lab needs a scientist like you and every person needs a friend like you. I am looking forward to seeing both you and Emre become the most amazing scientists in your research.

I would also want to thank my committee members Assist. Prof. Pınar Aydoğan Göktürk, and Assoc. Prof. Damla Eroğlu Pala. It was an honor for me to have them in my thesis committee. I also want to thank KUYTAM scientists who contributed to our characterization studies and my special thanks for Dr. Hadi Jahangiri for teaching me using many different characterization instruments and being so kind and supportive all the time. Additionally, I would like to thank TÜPRAŞ for the financial support of my master's project.

Finally, the most important thank you for me, my family. I would like to start with my mother, my superhero, my best friend, my idol. We did not just share a mother-daughter relationship, we shared a life together, we fight for everything we had together, and unfortunately, we shared a timeless pain together. I know that she does not like this sentence, but I own everything to her. She is the bravest, kindest and the strongest woman I know. Annecim, thank you for supporting me at every step of my life, thank you for giving me the trust that no matter how bad things get, you will be there for me. My biggest luck in this world is to be your daughter.

I want to thank my father, the second person I dedicated my thesis to. It is amazing that someone who is not even in this world anymore can be a huge support when things get bad. His personality, which my mother says he 100% passed on to me, his achievements and all the good things I have heard about him have always been a great motivation to me at every stage of my academic life while I was working to pursue my dreams. If I had hundred more chances in this life, hundred times I would choose to be his daughter. Babacım, I am so proud that you were, you are my father and I know that you are proud of me while I am following your footsteps. Just keep watching me through the stars I will make you even more proud than you are now:)

TABLE OF CONTENTS

List of Tables xii

List of Figures xii

Abbreviations xvi

Chapter 1: Introduction 1

1.1 Fundamentals of Photoelectrochemical H_2O Splitting 1

1.1.1 The Concept of Band Bending and Space Charge Layer 2

1.1.2 Properties of Semiconductor Photoelectrode Materials 5

1.1.3 Charge Carrier Dynamics of Photoanodes 6

1.2 Fundamentals of Photoelectrochemical H_2S Splitting 7

1.3 Literature Review on CdS Photoanodes for Photoelectrochemical H_2 Production: Synthesis Methods, Strategies to Enhance PEC Activity and Reasons of Activity Loss 9

1.3.1 Synthesis Methods and General Properties 9

1.3.2 Possible Reasons for Activity Loss 11

1.3.3 Strategies to Enhance the PEC Activity 11

1.3.4 Superiority of CdS Among Semiconductor Photoanodes 13

1.4 Aim and Summary of This Study 14

Chapter 2: Methodology 15

2.1 PEC Characterization Experiments 15

2.1.1 Voltamperometric Methods 15

2.1.2 Impedance Spectroscopy 17

2.2 Structural Characterization Experiments 19

2.2.1 Spectroscopic Methods 19

2.2.2 Imaging Microscopy Techniques 22

Chapter 3: Efficient Photogenerated Hole Utilization on 23

3.1 Introduction 23

3.2 Experimental 25
3.2.1 Materials and Chemicals 25
3.2.2 Synthesis of CdS Photoanodes 25
3.2.3 Photoelectrochemical Characterization 26
3.2.4 Structural and Surface Characterization 27
3.3 Results & Discussion 27
3.4 Conclusion 40
Chapter 4: Effect of Ultrathin ALD TiO_2 Overlayer on Charge Transfer and Utilization Properties of CdS Photoanode 42
4.1 Introduction 42
4.2 Experimental 43
4.2.1 Fabrication of FTO/CdS Photoanodes 43
4.2.2 Photoelectrochemical Characterization 44
4.3 Results & Discussion 44
4.4 Conclusion 54
Chapter 5: Photoelectrochemical H_2 Production from H_2S by Using CdS Photoanode with ALD TiO_2 Overlayer 55
5.1 Introduction 55
5.2 Experimental 56
5.2.1 Fabrication of FTO/CdS Photoanodes 56
5.2.2 Photoelectrochemical Characterization 56
5.3 Results & Discussion 56
5.4 Conclusion 64
Chapter 6: Summary and Future Work 65
References 67
Appendix A: Supporting Information for Chapter 3 81
Appendix B: Supporting Information for Chapter 4 88
Appendix C: Supporting Information for Chapter 5 91

List of Tables

Table 3A.1 Potential versus R_{CT} data of bare CdS, CdS/CTAB1, and CdS/CTAB2. ... 85
Table 3A.2 Surface sulfur vacancy content of bare CdS and CdS_S_v calculated by Cd and S atomic percent on the surface. ... 86

List of Figures

Figure 1.1 Energy band diagram of intrinsic, n-type, and p-type semiconductors. ... 2
Figure 1.2 Band bending in n and p-type semiconductors before and after electrolyte contact. ... 3
Figure 1.3 Band-energy diagrams of most frequently used semiconductor materials. ... 5
Figure 1.4 E(k) diagram of direct (left side) and indirect (right side) band gap transition. ... 5
Figure 1.5 Lifetime scale of electron-hole pairs within different processes of charge carrier dynamics ... 6
Figure 1.6 Pourbaix diagram of sulfide ions at different pH values and potentials. ... 8
Figure 1.7 PEC H_2S splitting reaction under acidic and alkaline conditions. ... 8
Figure 1.8 Hexagonal wurtzite crystal structure of CdS. ... 10
Figure 2.1 Randles model circuit with constant phase element. ... 17
Figure 2.2 XRD instrumentation scheme ... 20
Figure 3.1 XPS of (a) Br 3d, and (b) FTIR spectrum of bare CdS, CdS/CTAB1, and CdS/CTAB2. (c) HRTEM image of CdS/CTAB2 powder sample, (d) EDX elemental mapping of Br, Cd, and S, and (e) Br $K_{\alpha 1}$ elemental mapping. ... 28
Figure 3.2 (a) Chopped-light illumination LSV, (b) decay rates of the photocurrent after the anodic spike, (c) η_{inj} of are CdS, CdS/CTAB1, and CdS/CTAB2. (d) The schematic representation of the adsorption model of CTAB on CdS after dip coating. ... 31
Figure 3.3 (a) Nyquist plots recorded at 0.8 V and (b) the potential dependent R_{CT} plots of bare CdS, CdS/CTAB1, and CdS/CTAB2. (c) LSV and In-situ PL emission plots of Bare CdS and CdS/CTAB2. The PL measurements were done by using the same 3-electrode configuration of PEC experiments in a quartz spectroscopy cuvette. The PL

emission intensities were normalized with respect to the emission at 0.3 V by peak area integration. 33
Figure 3.4 (a) Transient OCP measurements with chopped illumination and (b) Mott-Schottky (measured in dark) plots of bare CdS, CdS/CTAB1, and CdS/CTAB2. 35
Figure 3.5 (a) CA at 0.7 V with 250 ms white LED light pulse of bare CdS and CdS/CTAB2, (b) stacked inset of the wiggle behavior during steady state, (c) schematic representation of the effect of CTAB on surface charge trapping passivation. 37
Figure 4.1 (a)Cd 3d, (b) S 2p, (c) Ti 2p, and (d) O 1s of bare CdS and CdS samples with 10-30-50-70-90 layers of ALD TiO_2 coating. 44
Figure 4.2 Relative band-edge alignment of CdS and TiO_2. 45
Figure 4.3 (a)Chopped illumination LSV of bare CdS, and 20,30, 40, 50, 70, and 90 ALD cycle TiO_2 coated CdS in 0.1 M NaOH, (b) decay rates and (c) cathodic spikes (when light is off) of bare CdS, CdS/50TiO_2, and CdS/90TiO_2. 45
Figure 4.4 SEM images of (a) bare CdS, (b) CdS/50TiO_2, and (c) CdS/90TiO_2. (d) EDX spectra of CdS/50TiO_2, and CdS/90TiO_2. 47
Figure 4.5 (a) UV-Vis absorbance spectra and Tauc plots of bare CdS, CdS/50TiO_2, and CdS/90TiO_2. 47
Figure 4.6 (a) Nyquist plots recorded at 1V and (b) R_{CT} and (c) C_{int} versus potential plots of bare CdS, CdS/50TiO_2, and CdS/90TiO_2. 49
Figure 4.7 1200 ms chopped light CA-TPC plots of bare CdS, CdS/50TiO_2, and CdS/90TiO_2 at (a) 0.4 V, (b) 0.7 V, and (c) 1 V. 50
Figure 4.8 (a) 250 ms on 250 ms off CA-TPC at 0.7 V and (b) stacked inset image of the wiggle behavior of bare CdS, CdS/50TiO_2, and CdS/90TiO_2. 51
Figure 4.9 Mott Schottky plots and of bare CdS, CdS/50TiO_2, and CdS/90TiO_2. 52
Figure 4.10 (a) Chopped illumination OCP plots and (b) photovoltage change of bare CdS, CdS/50TiO_2, and CdS/90TiO_2. 53
Figure 5.1 (a) CA of bare CdS in 0.1M NaOH (H_2O) and 0.1M NaOH feeded with H_2S for 30 min, (b) pictures of the CdS samples after CA with and without H_2S. 58
Figure 5.2 (a) Cd 3d, (b) S 2p, and (c) O 1s spectra of fresh CdS and CdS after CA experiment at 0.8 V in 0.1M NaOH and 0.1M NaOH/H_2S electrolytes. 59
Figure 5.3 (a) Continuous illumination and (b) chopped light illumination LSV of bare CdS in 0.1M NaOH and 0.1M NaOH/ H_2S electrolytes and LSV of 15-25-50 cycles TiO_2 coated CdS in 0.1M NaOH/H_2S. 60

Figure 5.4 ECSA plots of bare CdS in 0.1M NaOH and H_2S/0.1M NaOH electrolytes and 15-25-50 cycles TiO_2 coated CdS in 0.1M NaOH/H_2S. 61
Figure 5.5 R_{CT} versus potential plots of only (a) bare CdS and 15-25-50 cycles TiO_2 coated CdS in 0.1M NaOH/H_2S and (b) comparison of these plots with that of bare CdS in 0.1M NaOH. (c)Interfacial capacitance versus potential plots of bare CdS in 0.1M NaOH and 0.1M NaOH/ H_2S/ electrolytes and 15-25-50 cycles TiO_2 coated CdS in 0.1M NaOH/H_2S. 62
Figure 5.6 (a) Chopped illumination OCP plots and (b) photovoltage change bare CdS in 0.1M NaOH and H_2S/0.1M NaOH electrolytes and 15-25-50 cycles TiO_2 coated CdS in 0.1M NaOH/H_2S. 63
Figure 5.7 MS plots of bare CdS in 0.1M NaOH and H_2S/0.1M NaOH electrolytes and 15-25-50 cycles TiO_2 coated CdS in 0.1M NaOH/H_2S. 64
Figure 3A.1 (a) Cd 3d, (b) S 2p, (c) C 1s, and (d) O 1s XPS spectra of bare CdS, CdS/CTAB1, and CdS/CTAB2. 81
Figure 3A.2 XRD spectra of bare CdS, CdS/CTAB1, and CdS/CTAB2. 82
Figure 3A.3 FESEM images of (a) bare CdS, (b) CdS/CTAB1, and (c) CdS/CTAB2. EDS spectra of (d) CdS/CTAB1 and (e) CdS/CTAB2. 83
Figure 3A.4 Tauc plots and IPCE efficiencies of (a) bare CdS, (b) CdS/CTAB1, and (c) CdS/CTAB2. 83
Figure 3A.5 CV measurements at different scan rates of (a) bare CdS, (b) CdS/CTAB1 and (c) CdS/CTAB2. (d) ECSA plots of the photoanodes. 84
Figure 3A.6 LSV of bare CdS, CdS/CTAB1, and CdS/CTAB2 in (a) 0.1M NaOH and (b) 0.1M NaOH / 0.25 M Na_2SO_3. Measurements were performed with a 50 $mV.s^{-1}$ potential scan rate under continuous illumination. 84
Figure 3A.7 (a) Randles model circuit used for Nyquist plot fittings of bare CdS, CdS/CTAB1, and CdS/CTAB2. EIS fittings of (b) bare CdS, (c) CdS/CTAB1, and (d) CdS/CTAB2. 85
Figure 3A.8 Chopped light LSV of (a) bare CdS after and CdS_S_v, (b) CdS_S_v and CdS_S_v/CTAB. MS plots of (c) bare CdS and CdS_S_v, (d) CdS/CTAB1 and CdS_S_v/CTAB. 86
Figure 3A.9 (a) Cd 3d and (b) S 2p spectra of bare CdS and CdS_Sv, and (c) Br 3d spectra of CdS/CTAB1 and CdS_S_v/CTAB. 86
Figure 3A.10 TPC of bare CdS at different illumination times by LED light at 0.7 V. 87
Figure 4B.1 XRD spectra of bare CdS, CdS/50TiO_2, and CdS/90TiO_2. 88

Figure 4B.2 (a) Raman spectra of bare CdS, CdS/50TiO_2, and CdS/90TiO_2, and (b) inset of 3LO. 88
Figure 4B.3 Potential dependent Nyquist fittings of (a) bare CdS, (b) CdS/50TiO_2, and (c) CdS/90TiO_2. 88
Figure 4B.4 R_{CT} versus potential plots of (a) bare CdS, (b) CdS(50TiO_2, and (c) CdS/90TiO_2..... 89
Figure 4B.5 (a)Ti 2p and (b)S 2p XPS spectra of CdS/50TiO_2 before and after consecutive front illumination LSV measurements. 89
Figure 4B.6 CV of (a)bare CdS, (b)CdS/50TiO_2, (c) CdS/90TiO_2 at different scan rates and (d) ECSA comparison. 89
Figure 4B.7 Potential dependent 1200 ms light pulse TPC measurements of (a) bare CdS, (b) CdS(50TiO_2, and (c) CdS/90TiO_2. 90
Figure 5C.1 (a) CV scans of electrolytes with different Na_2S concentrations in 0.1 M NaOH and 30 min H_2S feeded 0.1 M NaOH, (b) calibration curve obtained by dissolved Na_2S concentration versus current at 0.94 V during anodic scan. 91
Figure 5C.2 FESEM images of fresh CdS and CdS after CA experiment at 0.8 V in 0.1M NaOH and 0.1M NaOH/ H_2S electrolytes. 91
Figure 5C.3 XRD spectra of fresh CdS and CdS after CA experiment at 0.8 V in 0.1M NaOH and H_2S/0.1M NaOH electrolytes. 91
Figure 5C.4 (a) UV-Vis and (b) Raman spectra of fresh CdS and CdS after CA experiment at 0.8 V in 0.1M NaOH and 0.1M NaOH/ H_2S electrolytes. 92
Figure 5C.5 CV scans of (a) Bare CdS, (b) CdS/15TiO_2, (c) CdS/25TiO_2, (d) CdS/50 TiO_2 in 0.1M NaOH/H_2S. 92
Figure 5C.6 Nyquist fittings of (a) bare CdS, (b) CdS/15TiO_2, (c) CdS/25TiO_2, (d) CdS/50 TiO_2 in 0.1M NaOH/H_2S at different potentials. 93

Abbreviations

PEC	Photoelectrochemical
VB	Valance Band
CB	Conduction Band
HOMO	Highest Occupied Molecular Orbital
LUMO	Lowest Unoccupied Molecular Orbital
SCL	Space Charge Layer
HER	Hydrogen Evolution Reaction
OER	Oxygen Evolution Reaction
TPC	Transient Photocurrent
EIS	Electrochemical Impedance Spectroscopy
PV	Photovoltaic
CTAB	Hexadecyltrimethylammonium bromide
LSV	Linear Sweep Voltammetry
CV	Cyclic Voltammetry
OCP	Open Circuit Potential
CA	Chronoamperometry
IPCE	Incident Photon-to-Current Efficiency
ECSA	Electrochemical Surface Area
MS	Mott-Schottky
XPS	X-ray Photoelectron Spectroscopy
PL	Photoluminescence
XRD	X-ray Diffraction
FTIR	Fourier-Transform Infrared
FESEM	Field Emission Scanning Electron Microscopy
EDX	Energy Dispersive X-ray Spectroscopy
HRTEM	High Resolution Transmission Electron Microscopy
FTO	Fluorine doped tin oxide
S_V	Surface sulfur vacancy
V_{fb}	Flat band potential
N_d	Donor density

Chapter 1:

Introduction

Through the years, the increase in anthropogenic CO_2 levels in the atmosphere caused harmful effects on human health and environment, which prompted scientists to investigate alternative solutions to provide a sustainable, accessible, green, and affordable energy source to satisfy the ever-growing energy demand of the society. Hydrogen is one of the most promising options as a carbon neutral, storable and transportable energy source. There are various ways to produce hydrogen such as thermal treatment of natural gas, catalytic decomposition of methanol, biomass conversion, hydrocarbon reforming, and electrolysis of H_2O[1]. Among all hydrogen production technologies, light-driven photoelectrochemical (PEC) water splitting using semiconductor materials has superior qualities such as low cost, facile construction, and high efficiency[2]. Moreover, it is more appealing than other methods mentioned above because it utilizes sunlight which is the most available energy source. There is no doubt that this technology will gain even more attention in near future as a more sustainable energy source than fossil fuels.

1.1 Fundamentals of Photoelectrochemical H_2O Splitting

The idea of splitting water into H_2 and O_2 by using PEC hydrogen production through semiconductor materials goes back to 1972 when Fujishima and Honda used TiO_2 photoanode in an electrochemical cell[3,4]. Their discovery has initiated extensive research on various materials that can be utilized for PEC water electrolysis. There are three main processes taking place in PEC water splitting. Photo-induced excitation of charge carriers (electron-hole pairs), separation of these charge carriers and their injection to the electrolyte for water splitting half reactions. Depending on the type of abundant defect or dopant, a semiconductor material can be classified as either n-type or p-type.

For the n-type semiconductors, there should be a dopant which acts like an electron donor since the majority charge carriers of n-type semiconductors are electrons. Meanwhile p-type semiconductors have positively charged holes as the majority charge carriers. Semiconductor materials can take n or p-type characteristics not only from different dopants or impurities but also from their native defects. For example, oxygen

vacancies are intrinsic defects which give n-type character to the metal oxide semiconductor materials such as $BiVO_4$, TiO_2, Fe_2O_3, and WO_3[5]. These defects or dopants determine the energy band positions of the semiconductor materials which are shown in Figure 1.1 where E_{VB}, E_{CB}, and E_F are the energy levels of valance band (VB), conduction band (CB), and Fermi level, respectively.

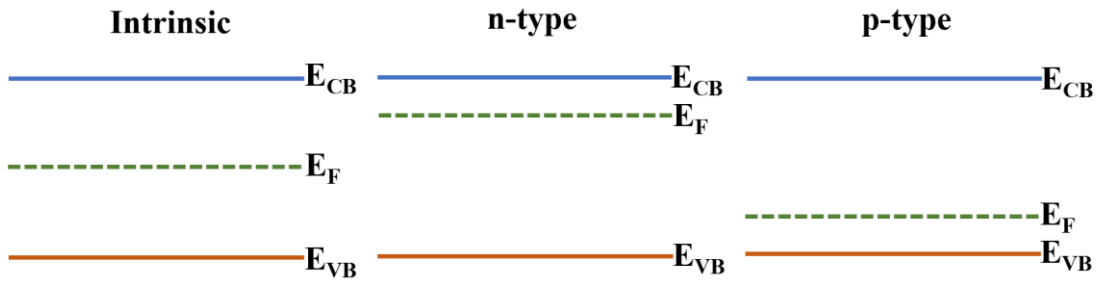

Figure 1.1 *Energy band diagram of intrinsic, n-type, and p-type semiconductors.*

In an intrinsic semiconductor, also known as pure semiconductor without any doping, the density of electrons is equal to the density of positively charged holes. Fermi level is defined as the highest energy level an electron can occupy at 0 K and it is expected to locate in the middle of E_{VB} and E_{CB} of an intrinsic semiconductor which are equivalent to highest occupied molecular orbital (HOMO) and lowest unoccupied molecular orbital (LUMO). In the case of an n-type semiconductor where the relative density of charge carriers is disturbed by a dopant or impurity which contributes to the electron density, Fermi level shows an upward shift towards the CB and vice versa for p-type semiconductors[6]. This band alignment is very important to understand the fundamental principles behind PEC water splitting mechanism.

1.1.1 The Concept of Band Bending and Space Charge Layer

One of the most important phenomena for PEC water splitting is the concept of band bending. As explained before, n-type and p-type semiconductors show differences in their energy band diagram due to their different majority charge carriers. This difference also affects the behavior of E_{VB} and E_{CB} when the semiconductor photoelectrode is in contact with an electrolyte.

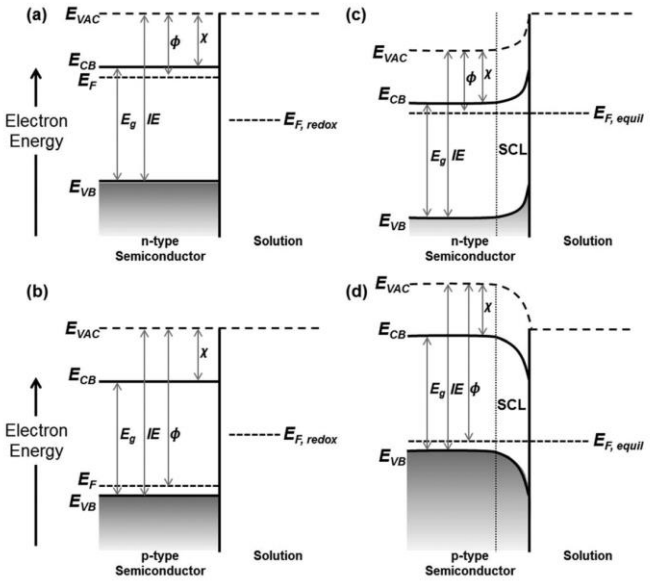

***Figure 1.2** Band bending in n and p-type semiconductors before and after electrolyte contact*[7].

When the photoelectrode is in contact with the electrolyte, there is an ionic interaction at the interface where they try to align their Fermi levels and form band bending structure. In Figure 1.2, the band bending of n and p-type semiconductors are shown with the energy levels where E_{VB}, E_{CB}, E_{VAC}, E_F, $E_{F,redox}$, and $E_{F,equil}$ are the energies of VB, CB, vacuum level, Fermi level of the semiconductor itself, and the equilibrium Fermi level. At the photoelectrode/electrolyte interface, there is a flow of electrons from the photoelectrode to the electrolyte or vice versa depending on the n/p type characteristics. As a result of this electron flow, a space charge layer (SCL) forms at the photoelectrode/electrolyte interface. Since the majority charge carriers are electrons in n-type semiconductors, the direction of this flow is from the photoelectrode to the electrolyte, which results in upward band bending and vice versa for the p-type semiconductors. This ionic interaction explains the utilization of electrons and holes in their respective water splitting half reactions which are hydrogen evolution reaction (HER), and oxygen evolution reaction (OER) where reduction and oxidation reactions take place. Therefore, semiconductor materials that are going to be used in HER and OER should be chosen from p-type and n-type materials, respectively. These half reactions follow different paths depending on the pH of the medium. See the HER and OER reaction in alkaline and acidic electrolytes below[8]:

Alkaline Water Splitting

$4H_2O + 4e^- \rightleftharpoons H_2 + 4OH^-$ **(HER)** $\mathbf{E^0_{red} = -0.83\ V\ (vs\ RHE)}$

$4OH^- + 4h^+ \rightleftharpoons 2H_2O + O_2$ **(OER)** $\mathbf{E^0_{ox} = -0.4\ V\ (vs\ RHE)}$

Acidic Water Splitting

$4H^+ + 4e^- \rightarrow 2H_2$ **(HER)** $\mathbf{E^0_{red} = 0\ V\ (vs\ RHE)}$

$2H_2O + 4h^+ \rightarrow O_2 + 4H^+$ **(OER)** $\mathbf{E^0_{ox} = -1.23\ V\ (vs\ RHE)}$

The thermodynamically required potential of overall water splitting potential is 1.23 V which is rather higher than self-driven built-in potentials of the semiconductor materials. This can be tuned by applying a bias to have enhanced band bending and charge separation.

The semiconductor photoelectrodes used in HER and OER are named photocathode and photoanode, respectively. These reactions simultaneously take place in a PEC cell.

A PEC cell can be constructed by using either single semiconductor material as photoanode/photocathode or one n-type material as photoanode and one p-type material as photocathode, which is called as tandem cell. In the first version, a metal counter electrode, usually Pt, is the cathode or anode depending on the n/p characteristics of semiconductor photoelectrode. For example, if an n-type photoanode is used in the cell, the metal counter electrode serves as the cathode and vice versa for p-type photocathode. The role of counter electrode in PEC cell is to have a complete circuit for charge flow. If we consider an n-type photoanode, while photogenerated holes are migrating to surface with upwards band bending, electrons are transferred to the counter electrode. In the second version, 2 semiconductor materials, one n-type one p-type, are utilized as photoanode and photocathode instead of using a metal electrode, which is considered to be more efficient. This type of configuration is called tandem cell which will be discussed later in section 1.3.3.

In the following subsection, important parameters about the electronic and optical structure of the semiconductor photoanode/photocathode materials will be discussed.

1.1.2 Properties of Semiconductor Photoelectrode Materials

Valance and conduction band positions of the semiconductor materials are very important when choosing a photoanode or photocathode. In Figure 1.2, the energy difference between the VB and CB is shown as E_g which stands for the band-gap energy, a very important property for the PEC activity. It is defined as the energy needed to excite an electron from the VB to the CB by leaving positively charged holes at VB[9]. In Figure 1.3, band-energy diagrams of well-known semiconductor materials are shown with the water splitting half reaction potentials.

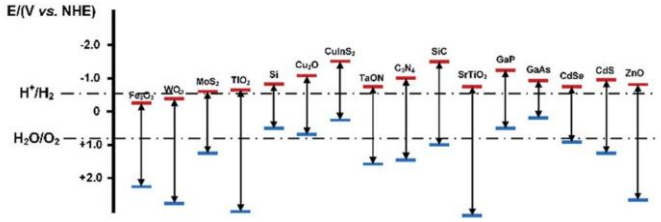

Figure 1.3 *Band-energy diagrams of most frequently used semiconductor materials[10].*

For a material to be considered as an efficient semiconductor for PEC water splitting, it should have a narrow band gap energy, which is generally between 2 and 2.5 eV, to have a high absorption of visible light[11]. Moreover, for an ideal semiconductor, the VB must be located at a more positive potential than OER and CB must be located at a more negative potential than HER potential.

Another important property to mention about band gap is the direct or indirect characteristics which is explained by E(k) diagram in Figure 1.4.

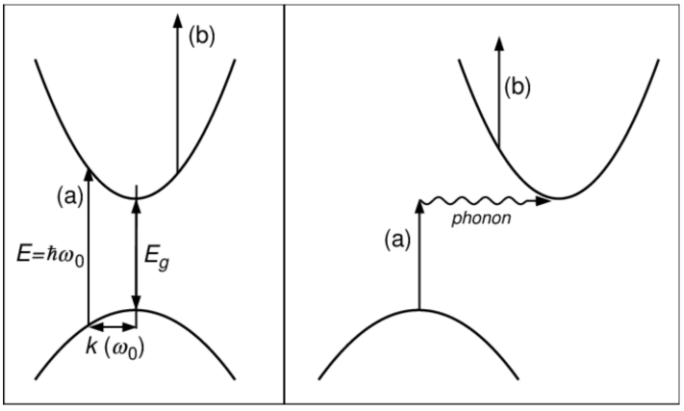

Figure 1.4 *E(k) diagram of direct (left side) and indirect (right side) band gap transition[12].*

In a direct band gap semiconductor material, the maximum energy level of VB and the minimum energy level of CB align within the same k-vector. On the other side, there is no such alignment for an indirect band gap semiconductor. Therefore, excitement of an

electron from VB to CB of a direct band-gap semiconductor is possible by a photon with an energy which is equal to the band-gap energy. However, such transition requires an intermediate momentum transfer to occur in indirect semiconductors, which is why direct band gap semiconductors are considered to be more efficient in terms of photon absorption ability [13]. However, the intermediate momentum transfer in indirect band-gap semiconductors makes them more appealing in terms of charge separation.

1.1.3 Charge Carrier Dynamics of Photoanodes

To understand the complex reactions at photoanode/electrolyte interface, it is important to know the benchmarks in charge carrier dynamics. Being the primary interest in semiconductor materials, metal oxides are the most frequently studied photoanodes for the investigation of reaction kinetics in PEC water splitting. In Figure 1.5, fundamental charge carrier dynamics processes are demonstrated.

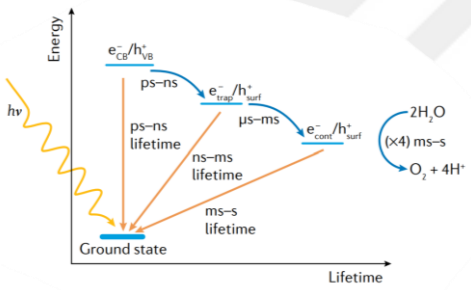

Figure 1.5 *Lifetime scale of electron-hole pairs within different processes of charge carrier dynamics*[14] .

The figure shows the time scale of fundamental processes that take place in PEC water splitting, such as charge separation and extraction. As it is shown in the figure the charge carriers lose their energy from separation to extraction. This deactivation is caused by the difference in time scales of these 2 processes and charge trapping. It is often observed in metal oxide photoanodes due to their strong ionic character which leads to interaction of photogenerated carriers with the lattice structure to form polorons. These polorons can trigger electron trapping by localization and cause charge recombination. Especially for metal oxide semiconductors with low carrier mobility, trapping puts a kinetic barrier on charge extraction, and it can be tuned by applying overpotential to boost band bending. In this study, we provided a trapping-induced activity loss mechanism for CdS, which is a much less studied concept compared to metal oxide photoanodes, by performing transient photocurrent (TPC) measurements at

different time scales. We believe that this can be an important contribution to promote research on charge carrier dynamics of metal sulfide photoanodes.

1.2 Fundamentals of Photoelectrochemical H_2S Splitting

H_2S is a very harmful and toxic by-product which is produced mainly by refineries and biogas production plants. Moreover, it is found in oceans and underground waters resulting from acid rains caused by SO_x emissions. So far, different methods have been evaluated to get rid of H_2S such as chemical filters, thermal treatment, and chemical decomposition [15–17]. In refineries, H_2S is formed in the hydrodesulfurization units where the sulfur in crude oil is removed by using gray hydrogen and the exhausted H_2S is partially oxidized to form elemental sulfur and H_2O via "Claus Process" which is shown below [18]:

$$2H_2S + 3O_2 \rightarrow 2SO_2 + 2H_2O$$

$$SO_2 + 2H_2S \rightarrow 3S + 2H_2O$$

This process has been widely used in refineries over the years and has a sulfur recovery efficiency of 98%. However, it can produce other toxic tail gas which is not environmentally friendly and H_2S is not utilized as a potential green hydrogen source in this method. This process has been improved by using a catalytic material which consists of iron and chromium oxides on alpha-alumina support. It is called Superclaus process because it provides highly selective oxidation of H_2S to produce bulk sulfur by 99% efficiency without oxidizing other gases [19].

Although H_2 production via H_2O splitting is still one of the most extensively researched topics in the literature, H_2S remains as an unconsidered area because it is extremely corrosive, toxic, and difficult to work with since it is in gas phase at room temperature and atmospheric pressure. It must be noted that H_2S has the potential to be even a more promising candidate for green hydrogen production than H_2O considering that these reactions have theoretical similarities, which means that the already existing technologies for H_2 production from H_2O can be utilized for H_2S as well. The reason why H_2S can be more appealing than H_2O is that the thermodynamic potential of overall H_2S splitting reaction is 0.27 V which is significantly lower than that of H_2O. Therefore, more H_2 can be produced with less energy in H_2S splitting[20].

Similar to H_2O splitting, H_2 production from H_2S by solar PEC energy conversion is expected to have different reaction routes in acidic and alkaline electrolyte. Even though H_2S splitting and H_2O splitting are very similar in theory, H_2S splitting has a much more complex reaction model than that of H_2O splitting because of the pH and potential dependent transformation between sulfide species which is shown in Figure 1.6.

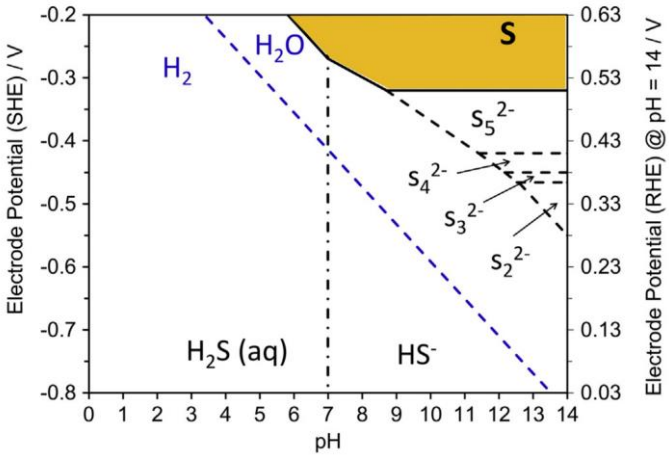

Figure 1.6 Pourbaix diagram of sulfide ions at different pH values and potentials[21].

It is important to consider the pH and potential dependence of these ions while choosing an electrolyte to investigate the reaction mechanism. These ions can affect the oxidation products and the stability of the catalyst. One of the most important studies on this topic has been reported by Zong et.al. in Angewandte Chemie where they performed PEC H_2S splitting in both alkaline and acidic conditions with an n-type photoanode[22]. Both alkaline and acidic H_2S splitting have their own advantages and disadvantages with different requirements. A simple schematic representation of the reactions is shown in Figure 1.7.

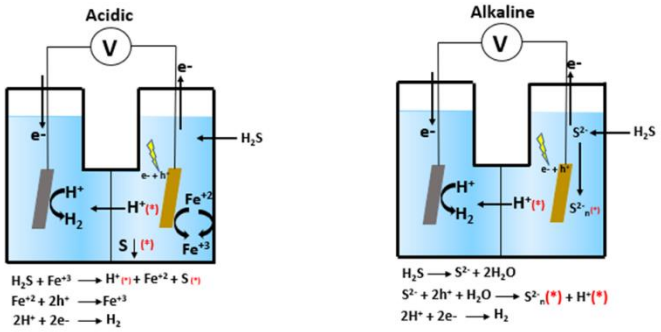

Figure 1.7 PEC H_2S splitting reaction under acidic and alkaline conditions.

Different from H_2O, there are multiple reactants and products that can be included in the oxidation and reduction reactions of H_2S splitting. According to the Pourbaix diagram

of sulfide species, dissolved H_2S can be found in HS^- at moderate pH values. The H_2S:HS^- ratio increases as the electrolyte becomes more acidic. The complexity of H_2S splitting and the variety of sulfide ions can bring additional requirements such as using an H-cell configuration with a proton selective membrane instead of a single cell, so that the sulfide ions do not interfere with the reduction reaction on the cathode surface.

One of the advantages of acidic H_2S splitting is that the H^+ ions in the electrolyte can promote the H_2 production at the cathode chamber. However, it requires utilization of a redox couple to maintain a chemical loop between H^+ and H_2. Most frequently used redox couples are Fe^{+2}/Fe^{+3} and I^-/I_3^-. Although these redox couples are necessary to drive H_2S splitting reaction under acidic conditions, they are not very suitable for PEC applications since they have very intense colors which can block the light absorption of the photoelectrode, but they can be easily utilized for electrochemical H_2S splitting. Therefore, depending on the stability of the photoelectrode, alkaline electrolytes can be preferred for PEC H_2S splitting. Another disadvantage of these redox couples is that they can penetrate through the proton selective membrane, which causes interference between anodic and cathodic reactions and reduce the overall reaction efficiency. Ma *et.al*. have reported this problem and suggested the utilization of phosphomolybdic acid which has a larger size than other redox couples and it does not cause crossover between oxidation and reduction reactions by passing through the proton selective membrane [23].

1.3 Literature Review on CdS Photoanodes for Photoelectrochemical H_2 Production: Synthesis Methods, Strategies to Enhance PEC Activity and Reasons of Activity Loss

1.3.1 Synthesis Methods and General Properties

Among all semiconductor photoanode candidates CdS is a very strong option because of its narrow band-gap energy (2.4 eV), efficient visible light absorption, and suitable band-edge alignment for H_2O splitting half reactions. However, because of its high toxicity and light-caused stability problems, it is not as widely researched as other semiconductors. It is an n-type direct band gap semiconductor material with a tetrahedron chemical bonding structure which can be found in 2 different crystal structures namely cubic zinc blende and hexagonal wurtzite [24].

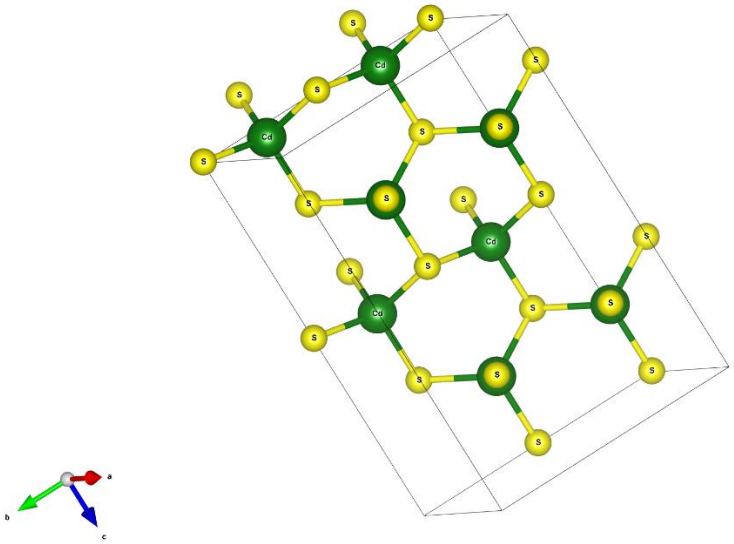

Figure 1.8 Hexagonal wurtzite crystal structure of CdS.

It has been reported that the hexagonal wurtzite structure, shown in Figure 1.8, is thermodynamically more stable than cubic zinc blende at high temperatures [25]. Depending on the synthesis method, post-synthesis heat treatment etc. CdS can be synthesized in both crystal structures. In the literature, various synthesis methods have been reported for CdS thin films such as electrodeposition[26], chemical bath deposition [27,28], spin coating [29], and hydrothermal deposition [30–33]. Among all methods, hydrothermal deposition is one of the most suitable methods as an easy and cheap way to deposit CdS on different substrates. The procedure details will be explained later in section 3.2.2.

It is a simple method where Cd and S precursors, which are typically cadmium nitrate and thiourea, are dissolved in H_2O and heated in an autoclave reactor to give a reaction above ambient pressure. High temperature and pressure of hydrothermal deposition method allows synthesis of high crystallinity materials within a one-step process [34]. The advantage of this method is that both powder synthesis and thin film deposition can be done simultaneously by adding a substrate material to the autoclave. The same method can be performed by using an organic solvent instead, which is referred as solvothermal synthesis [35]. In the hydrothermal and solvothermal synthesis, there are different reaction parameters such as temperature, reaction time and molar ratio of the precursors which can be tuned to manipulate the structural properties and PEC performance of CdS. For example, a sulfur vacancy rich CdS photoanode can be synthesized by decreasing the S: Cd precursor ratio. Moreover, changing the reaction

temperature or time can significantly affect the morphology of the final product, which plays a critical role in charge carrier dynamics [36,37].

1.3.2 Possible Reasons for Activity Loss

Although CdS is still one of the most promising photoanodes, its potential and superior qualities are not fully utilized. The reason behind this problem is the light-induced activity loss of CdS. One of the reasons that differentiates CdS from metal oxide semiconductors is that its photo-corrosion mechanism includes sulfur species with different oxidation states which are electrochemically active and very unstable. The details and the pH dependence of these species are discussed more in detail in section 1.2. It has been reported that in alkaline electrolytes, CdS can dissolve in the electrolyte, forming Cd^{2+} and S^{2-} ions, when the photoanode is irradiated to produce charge carriers. The interaction of photogenerated holes is mostly through S^{2-} since it can be oxidized to SO_4^{2-}, SO_3^{2-}, S^0, or polysulfides. These oxidation products can block the active sites or limit the light absorption ability [38–40]. In Chapter 3, the effect of sulfide oxidation is investigated by using PEC characterization methods.

Another reason for activity loss of CdS is the recombination of photogenerated electrons and holes at the photoanode surface. As explained in section 1.1.1, band bending is the key process for the charge separation to utilize electrons and holes in their respective water splitting reaction. If the charge separation is not good enough, the charge carriers give recombination at the surface instead of going to OER or HER. One of the important parameters that contribute to charge recombination is the surface states that can act like electron trap centers. For CdS, sulfur vacancies are the possible trap centers since they are electron poor and can trap photogenerated electrons [41].

In this study, the effect of surface sulfur vacancies is analyzed to investigate the trapping mechanisms on CdS surface and the possible activity loss paths.

1.3.3 Strategies to Enhance the PEC Activity

Despite the drawbacks mentioned earlier, CdS is a very promising photoanode candidate because of its relatively high activity and strong visible light absorption. Therefore, the research on CdS photoanodes was mostly focused on combining CdS with different materials to benefit from its superior qualities rather than understanding the fundamentals of its charge carrier transfer and utilization properties. Although

utilization of CdS to achieve high efficiencies is very important, analysis of the charge carrier dynamics is an important insight to provide a better understanding about the processes that might trigger photo-corrosion and contribute to the research on different semiconductor photoanode materials.

Heterojunctions

One of the most widely used applications of CdS is theheterojunction fabrication by using different semiconductor materials with suitable band-edge alignment. Depending on the material type, heterojunction structures can be classified as n-n, p-p, or n-p type. The main goal of heterojunctions is to have enhanced charge separation and utilization which is difficult to obtain with a single semiconductor [42]. WO_3/CdS heterojunctions are extensively studied as a type II heterojunction where E_{CB} and E_{VB} of WO_3 are lower than those of CdS to facilitate the transfer of photogenerated electrons from CdS to WO_3 [43]. Additionally, $BiVO_4$, TiO_2, and Fe_2O_3 was also utilized as relatively more stable semiconductor materials to benefit from the strong light absorption of CdS [44–46].

Surface Modification & Bulk Doping

Another method is to modify CdS with OER co-catalysts such as noble metals, metal hydroxides and carbon-based materials. The idea of co-catalysts is to promote hole utilization for OER so the light-induced activity loss can be suppressed [47]. Similarly, using a hole scavenger in the electrolyte can also diminish photocorrosion by preventing the interaction of photogenerated holes with the photoanode itself [48]. In the literature, CdS was modified with NiOOH, CoPi, Pt and MoS_2 [33,46,49–51] . Utilization of a co-catalyst on the photoanode surface can enhance the activity and stability significantly by introducing active OER sites on the surface and enhance the charge injection efficiency, which means that more holes can be included in water oxidation reaction without giving recombination at the surface or oxidizing photoanode material itself.

CdS does not have poor light absorption or short diffusion length problem so generally surface modifications are more suitable for it rather than tuning bulk properties. However, there are such examples in literature. Bulk modifications can be performed by different strategies such as controlling the morphology of the material, introducing defects, or doping. Fang et.al. reported synthesis of CdS with different morphologies and investigated the effect of morphology on the activity [38]. PEC performance of a photoanode can be tuned by enhancing light absorption or charge carrier mobility through different morphologies. Secondly, defects are also crucial for

the PEC activity which is widely studied for metal oxide semiconductors because of their tunable oxygen vacancies. The abundant defect of CdS is sulfur vacancies and they affect many important parameters such as donor density (N_d), electron mobility and more importantly, they are possible electron trap sites. He *et.al.* demonstrated synthesis of sulfur vacancy rich CdS and they proved that sulfur vacancy triggers the formation of spin polarization electric field which provides enhanced charge separation [52]. As mentioned before, the n-p type characteristics come from the defects or dopants. Similar to defect engineering, doping is also used to control PEC performance. For example, Pareek *et.al.* used Zn-doped CdS photoanode by integrating zinc sulphate in chemical bath deposition solution and their electrochemical impedance spectroscopy (EIS) studies demonstrated less charge recombination and boosted charge separation [53].

Utilization of Tandem Cells

In addition to the strategies which are used to modify CdS itself, PEC configuration can also be modified for higher efficiency. Construction of tandem cells is one of the most crucial approaches to obtain a self-driven water splitting system. The two main types of tandem cells are PEC/PEC cells which consist of an n-type photoanode and a p-type photocathode, and PEC/PV cell where a photovoltaic (PV) device is used to drive the reaction. PEC/PEC type tandem cell allows absorption of a wide range of photons to increase the overall efficiency of the system. On the other hand, PEC/PV tandem cell is an alternative way as an unassisted PEC system with the integration of a photovoltaic device for the potential bias [54,55].

1.3.4 Superiority of CdS Among Semiconductor Photoanodes

There are many photoanode materials which have been studied more in detail than CdS. On the other side, CdS was utilized with different materials very often because it has a long charge carrier diffusion path which is critical for extraction of photogenerated charge carriers from bulk phase, and its strong visible light absorption to produce more electron-hole pairs. The reason why fundamental charge carrier dynamics of other semiconductor photoanodes, especially metal oxides, has been more prevailing than CdS was not their exclusive properties but the downsides of CdS itself. However, when the overall performance is considered, CdS can be more worthy to work on. For example, TiO_2 and Fe_2O_3 are known for their stability, but TiO_2 has a larger band-gap energy than most of the semiconductor photoanodes (3.2 eV) which makes it

less appealing due to poor visible light absorption and Fe_2O_3 suffers from poor hole mobility [56,57]. $BiVO_4$ has a poor electron diffusion ability which limits its utilization foe OER [58,59]. What makes CdS superior to other photoanodes is that the problems mentioned above require more complex solutions such as building heterojunctions to facilitate charge carrier extraction or bulk doping. Meanwhile the activity of CdS can be tuned even by a post-synthesis surface modification as we present in Chapter 3.

1.4 Aim and Summary of This Study

Although CdS has the ability to reach significantly high efficiencies, PEC water splitting is a complicated process with different charge transfer and utilization mechanisms taking place simultaneously. Therefore, understanding the fundamental charge carrier dynamics is as important as searching for different methods to provide insight for further research and different semiconductor materials.

In this study, fundamental charge carrier dynamics of CdS was investigated by using structural and PEC characterization techniques. Different mild surface modification methods were applied to improve the charge separation and injection properties of CdS. TPC behavior of the samples is extensively studied, and different charge utilization mechanisms are proposed.

In Chapter 3, CdS surface was modified with a cationic surfactant cetyltrimethylammonium bromide (CTAB) overlayer which showed an enhancement in PEC activity and hole extraction. The role of surface sulfur vacancies on the activity loss of CdS has been investigated via TPC measurements and XPS analysis.

In Chapter 4, the effect of ultrathin TiO_2 overlayer on CdS was investigated as another mild surface modification method. Inspired by the findings from Chapter 3, we analyzed the effect of relative band-edge alignment of TiO_2 and CdS.

In Chapter 5 we investigated the potential of CdS for H_2S splitting and tried TiO_2 overlayer to enhance the activity of CdS for H_2S splitting. The effect of H_2S on the stability of CdS was analyzed by using XPS and CA measurements.

Chapter 2:
Methodology

2.1 PEC Characterization Experiments

2.1.1 Voltamperometric Methods

Voltamperometric methods are widely used in electrochemistry to investigate the response of photoelectrodes to applied potential. The most frequently used voltamperometric methods are summarized below.

Linear Sweep Voltammetry (LSV)

LSV, also known as linear polarization, is one of the most important performance testing experiments used in PEC water splitting. It is performed by increasing or decreasing the applied potential, which are called anodic sweep and cathodic sweep respectively. After the measurement, the data is plotted as current versus applied potential. It can be done at dark, front illumination, and back illumination. Another version of LSV which has an important place in PEC water splitting research is chopped illumination LSV where TPC behavior is analyzed. It provides important information about charge transfer and utilization processes and how they change with respect to applied potential.

Injection Efficiency Measurement (η_{inj})

Injection efficiency is a measure of how effectively photogenerated holes are being utilized in OER. It is affected by many factors such as applied bias or surface modifications. It can be calculated by using the formula below:

$$\eta_{inj} = \frac{j_{NaOH}}{j_{NaOH/Na_2SO_3}} \quad (2.1)$$

Where j_{NaOH} is the photocurrent density in the scavenger free electrolyte and j_{NaOH/Na_2SO_3} is the photocurrent density in hole scavenger containing electrolyte which are 0.1M NaOH and 0.1M NaOH/ 0.25M Na_2SO_3 in this study.

Cyclic Voltammetry (CV)

CV is also a very commonly used electrochemical method like LSV. Differently, the applied potential is not only in one direction. A potential window is scanned in both anodic and cathodic direction. It is used to investigate oxidation and reduction processes

taking place in an electrochemical system. Progress of these processes can be analyzed by increasing the number of CV scans [60].

Moreover, CV at different scan rates can be used to investigate electrochemical surface area (ECSA) which is a measure of double layer capacitance [60]. It is calculated by taking CV at different scan rates and taking half of the difference between anodic current density and cathodic current density at the same potential which should be in the non-faradaic region.

Open Circuit Potential (OCP)

OCP is defined as the potential difference between the working and reference electrode when there is no current flowing through the cell. It is also called the self-driven potential of the system. It is measured under dark or illuminated conditions and the change in OCP from dark to illuminated condition is defined as photovoltage [61]. Similar to LSV, it can be measured by chopped illumination as well. In this study, we used OCP measurement with chopped illumination to see how photovoltage changes.

Chronoamperometry (CA)

CA is performed by applying a constant potential to analyze the stability of a photoelectrode. It is also used to perform electrodeposition experiments to drive the deposition reaction. In addition to stability measurements at constant illumination, it can be done under chopped illumination to get TPC data which can be very informative about the charge carrier dynamics at photoelectrode/electrolyte interface. TPC analysis by chopped illumination LSV and CA has an important part in this study, which will be shown in chapter 3, 4, and 5.

Incident Photon-to-Current Efficiency (IPCE)

IPCE is an expression of how efficiently the incident photons at a certain wavelength are converted to photocurrent density per electron transfer. It is calculated by the formula given below:

$$IPCE = \frac{|j_p - j_d| \times 1240}{\lambda \times P_{in}} \qquad (2.2)^{62}$$

Where j_p is the photocurrent under illumination, j_d is the dark current, λ is the wavelength of the incident light and P_{in} is the power of the incident light. IPCE is defined by the efficiency of photon absorption, e^-/h^+ pair generation, charge separation and transfer. Therefore, it can provide information about all these important processes [63]. The effectiveness of the strategies which are explained in section 1.3.3 can be tested by using IPCE. For example, if the photon absorption behavior of a sample does not

change after a modification but IPCE is improved, the activity increase can be associated with enhancement of charge separation or charge transfer. In addition to charge carrier dynamics, IPCE can be used to interpret changes in the band-gap energy [53].

Electrochemical Surface Area Measurement (ECSA)

ECSA is used to estimate the double layer capacitance and compare the performance of electrocatalysts. CV at different scan rates within a non-faradaic potential window where there is no significant current. For photoelectrodes, it should be performed at dark, between 2 potentials where there is no significant current so the non-faradaic charging-discharging can be measured [64].

In ECSA analysis, the difference between the anodic and cathodic scan current at one potential is taken and divided by 2 which is shown in the formula below.

$$\frac{j_{anodic} - j_{cathodic}}{2} \tag{2.3}$$

In this study, ECSA analysis was conducted using this method. The double layer capacitance is found by using linear fitting for $(j_{anodic}-j_{cathodic})/2$ versus scan rate plot.

2.1.2 Impedance Spectroscopy

Electrochemical Impedance Spectroscopy (EIS)

EIS is one of the most important techniques in electrochemistry where electrical circuit elements such as resistors, capacitors, and inductors are used to make a model of the PEC system. In this technique alternating current (AC) is used as the input and the interruptions in the current flow is measured by changing the frequency of applied AC [65]. EIS provides valuable information about the charge carrier dynamics, such as the charge transfer resistance and capacitive behavior at the electrode/electrolyte interface. Depending on the electrode structure, EIS data can be modeled by different electrical circuits [66,67]. One of the most frequently used circuits is Randles circuit which consists of 2 resistors and a capacitor shown below.

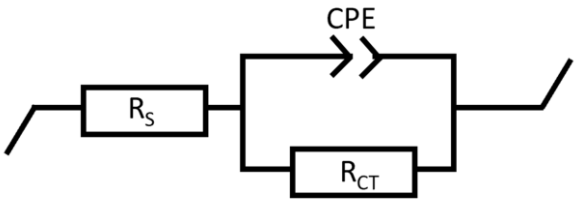

Figure 2.1 *Randles model circuit with constant phase element.*

In Figure 2.1, R_S represents the resistance of the electrolyte and the circuit elements such as connections, cables etc., R_{CT} is the charge transfer resistance at the electrode/electrolyte interface, and CPE is called constant phase element which is an "imperfect capacitor". It is used instead of a regular capacitor when the photoelectrode surface has roughness, pin holes, or imperfections like colloid particles [68]. Depending on the number of overlayers, surface modifications or the electronic structure of the photoelectrode, the equivalent electrical circuit might change.

EIS analysis of a photoelectrode can be performed in dark and under illumination at different potentials. One way of analyzing EIS data is Nyquist plot which is the outcome of EIS measurements where the negative imaginary part of the impedance ($-Z_{im}$) is plotted with respect to real part of the impedance (Z_{re}) at different frequencies. It is used for the interpretation of capacitance and interfacial resistance. For example, the first and second x-intercept of a Nyquist plot fitted by Randles model represents the resistance coming from the electrolyte and interfacial charge transfer resistance. Moreover, capacitance over modulated frequencies can be interpreted from the plateau of C_{re} (real component of the capacitance) versus frequency plot [69].

Mott Schottky Analysis (MS)

MS is an impedance-based technique which is used to measure the flat band potential (V_{fb}) and donor/acceptor density ($N_{d/a}$). The theoretical explanation of this technique is given in section 1.1.1 where the process of band bending and SCL formation is explained in detail. It measures the capacitive behavior through SCL by varying the applied bias and plotting the reciprocal of the square capacitance versus potential by the MS equation shown below.

$$\frac{1}{C^2} = \frac{2}{\epsilon\epsilon_0 A^2 e N_{d/a}} \left(V - V_{fb} - \frac{k_B T}{e}\right) \qquad (2.4)$$

Where C is the capacitance at the photoelectrode/electrolyte interface, ϵ is the dielectric constant of the photoelectrode, ϵ_0 is the vacuum permittivity constant, A is the area of the photoelectrode, e is the elementary charge and $N_{d/a}$ is the donor or acceptor density, V is the applied bias, V_{fb} is the flat-band potential, k_B is the Boltzman constant, and T is the temperature. Since $N_{d/a}$ is inversely proportional to the slope of the MS plot, positive slope and negative slope are interpreted as n and p type characteristics, respectively. On the other hand, V_{fb} can be determined from the x-intercept of the MS plot. It is a measure of potential required to make depleted bands go back to the flat band edge position [70].

2.2 Structural Characterization Experiments

2.2.1 Spectroscopic Methods

X-ray Photoelectron Spectroscopy (XPS)

XPS is a surface sensitive technique which is used for the investigation of the elements present on the surface of a sample, their binding states, and their percentage. It has a probe depth of 3-10 nm which makes it suitable for the thickness determination of thin film samples. The working principle behind XPS is the photoelectric effect where a metal surface is bombarded by an X-ray beam and electrons which have binding energies lower than that of X-ray beam are ejected from the surface. It measures the kinetic energy and the number of electrons ejected. Since the energy of the X-ray beam is already known from the source, the binding energy can be calculated. It does not only give information about the elemental composition and oxidation states but also the electron environment that can affect the binding energy of the emitted electron and cause peak shifts. Depending on the orbital where electron is located, the XPS peaks can be either singlet or doublet which is determined by the degeneracy of the electrons. For example, p and d orbitals give doublets coupling whereas s orbital electrons are singlets due to lack of spin-orbit coupling [71,72]. XPS analysis takes an important part in this study to investigate the elemental composition of photoanode surface after different treatments. Since the surface modifications in this study are mild treatments, XPS is the most informative characterization tool to analyze the surface composition.

Photoluminescence Spectroscopy (PL)

PL spectroscopy is a very commonly used method to investigate the charge carrier recombination and lifetime which are very important for a photoelectrode and photocatalyst. In PL spectroscopy, the sample is irradiated by a light source and the electrons are excited to a higher energy state. After the photoexcitation, the electrons are turning back to the ground state, releasing photons in the visible light region. The intensity and wavelength of the emission provides information about the charge carrier recombination of the photocatalysts [73,74]. In this study, PL spectroscopy was used in Chapter 3 with an in-situ configuration to show the potential dependence of electron-hole recombination at CdS surface.

X-ray Diffraction Spectroscopy (XRD)

XRD is one of the most important characterization tools in material science to analyze the crystal structure and atomic spacing of materials. In Figure 2.2, a schematic representation of XRD instrumentation is shown.

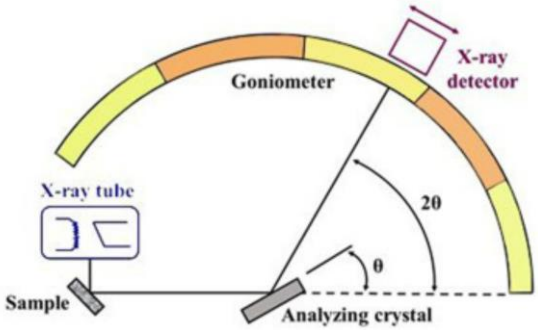

Figure 2.2 *XRD instrumentation scheme* [75].

Here, the analyzing crystal is bombarded by x-rays which are produced by a cathode ray and filtered through a monochromator. The incident beam is scattered from the crystal lattice with angle θ. If the path difference and the order of diffraction satisfies the Bragg's Law, constructive interference and X-ray diffraction take place. The Bragg's equation is shown below:

$$n\lambda = 2dsin\theta \tag{2.5}$$

Where n is the order of diffraction, λ is the wavelength of the incident radiation, d is the interplanar distance, and θ is the angle of diffraction. XRD measurement is conducted by scanning a range of 2θ and rotating the sample which is controlled by the goniometer. The XRD spectrum of intensity of the diffracted rays versus 2θ is a fingerprint of a crystal structure, showing the peaks of the crystal planes present in the lattice structure.

UV-Vis Spectroscopy

UV-Vis spectroscopy is used to investigate the photon absorption characteristics of a sample from UV to visible light range, which is very important for photocatalysts and photoelectrocatalysts. It is based on the Beer's law which is used to explain the ratio of the light passed through the sample with respect to the wavelength of the incident light. UV-Vis data is used to calculate the band-gap energy of a photoelectrode by using the Tauc equation shown below:

$$(\alpha h\nu)^n = B(h\nu - E_g) \tag{2.6}$$

Where α is the absorption coefficient, h is the Planck's constant, ν is the frequency of the incident photon, n is the number of allowed transitions, B is the proportionality constant and E_g is the band-gap energy. For direct semiconductors and indirect semiconductors, n is taken as 2 and ½ respectively [76]. In this study, UV-Vis spectroscopy was used to measure the reflectance of thin film samples to measure their band-gap energy. The reflectance versus wavelength data was converted to absorbance to use in Tauc equation. The Kubelka Munk calculation is shown below.

$$F(R_\infty) = \frac{K}{S} = \frac{(1-R_\infty)^2}{2R_\infty} \quad (2.7)$$

Where R_∞ is $\frac{R_{sample}}{R_{standard}}$, K is the absorption coefficient and S is the scattering coefficient [77].

Raman Spectroscopy

Raman spectroscopy is a qualitative and quantitative characterization tool which is used to investigate the chemical structure and molecular interactions based on the vibrational modes of molecules. This technique uses a laser beam to illuminate the sample and analyzes the light scattered from the sample. When the light scattered from the sample it can be either elastic or inelastic which are referred to as Rayleigh and Raman scattering, respectively. In the first one, the scattered light has the same energy as the incoming beam whereas in Raman scattering it is scattered with a different energy and frequency. Raman spectroscopy is used to identify the vibrational movements within a molecule which all have their own frequency like a fingerprint. When the energy of the incoming beam is matched with the vibration energy of a bond in the molecule, some of the light is used for vibration and rest is scattered and used to create a spectrum. It is used to investigate the bonds and the molecules present in the sample by the frequency of the peaks in the spectrum [78].

Fourier Transform Infrared Spectroscopy (FTIR)

FTIR is a common spectroscopy technique which is used to identify the vibration or rotations of chemical bonds and it is very informative about the different functional group present in the molecule. In this method, IR radiation is sent to a sample, some of it is absorbed by the sample and some of it passes through it. When the energy of the IR radiation matches with the energy of vibrational or rotational mode and a characteristic

signal is created. FTIR is an advanced version of classical IR with Michelson interferometer which allows much faster measurement [79].

2.2.2 Imaging Microscopy Techniques

Field Emission Scanning Electron Microscopy (FESEM) &

FESEM-Energy Dispersive X-Ray Spectroscopy (FESEM-EDX)

FESEM utilizes a focused electron beam produced by the electrons produced from a field emitter gun which makes it differ from the regular scanning electron microscope. The beam scans the surface of the sample, and an image is formed by the detection of electrons and photons emitted from the surface from the interaction between the sample and electron beam. FESEM provides many advantages such as imaging of the very small (up to 1 nm) structures with 3 to 6 times better resolution and 500000x magnification by using a brighter and focused electron beam [80].

EDX is a technique which is applied within FESEM by detecting the energy of the emitted X-rays from the sample. Since the X-rays form in a depth around 2 μm, EDX is not considered as a surface sensitive characterization. However, depending on the energy and intensity of the emitted X-rays can be useful to investigate the elemental composition of the sample [81].

High Resolution Transmission Electron Microscopy (HRTEM)

HRTEM is a high magnification version of TEM which allows to see the direct images of the atomic structure with a magnification up to 1,500,000x. Different from SEM, HRTEM is based on detection of electrons transmitted through the sample. The high contrast image is formed by bombarding the sample with an electron beam first. Electrons which are transmitted and scattered give bright and dark images, respectively. It is a useful tool to identify defect sites such as vacancies, crystal lattice distances, and chemical composition [82,83].

Chapter 3:

Efficient Photogenerated Hole Utilization on CdS Photoanode Surface via CTAB Overlayer

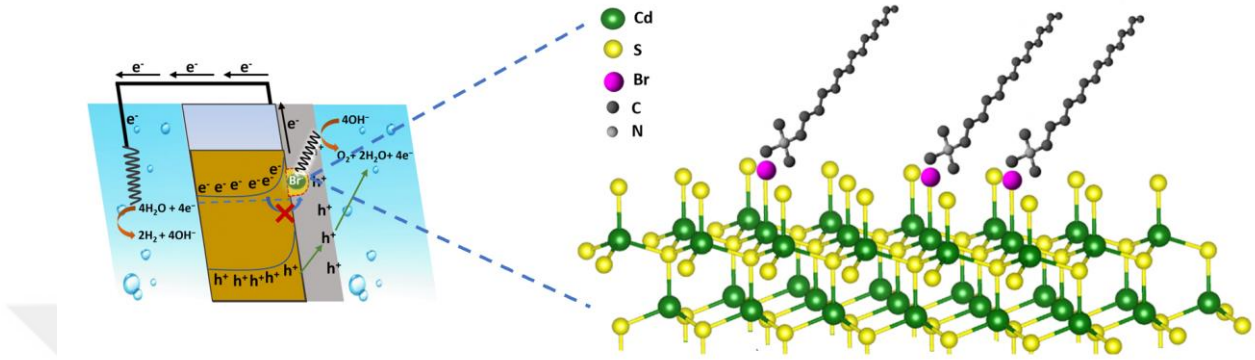

3.1 Introduction

PEC energy conversion by splitting water using semiconductor materials is one of the most promising clean energy technologies as a facile and effective strategy for converting solar energy into green hydrogen. Among all semiconductor photoanodes, CdS is an excellent choice owing to its superior qualities, such as appropriate band positioning, narrow band-gap energy, and efficient visible light absorption characteristics [84]. Despite the advantages, its widespread utilization is still limited by poor charge separation and instability issues due to surface charge recombination, which results in photocorrosion [85].There have been several attempts to enhance the OER activity and photo-stability of CdS, such as building heterojunction structures with other semiconductors to improve hole extraction [43,50,86], using OER co-catalysts for better charge utilization at the photoanode-electrolyte interface [87–89], and modification of the photoanode surface with passivation overlayers to prevent photocorrosion [90,91]. Although such surface engineering strategies can increase the photocurrent values and boost the oxygen evolution kinetics, the photostability issues, and the fundamental understanding of the charge transfer and utilization mechanisms remain a matter of debate.

In addition to these possible solutions, it has been reported that tuning the morphology and particle growth of semiconductors with the help of surface-active

reagents can also have an impact on its photocatalytic and PEC activities [92]. It is known that surfactants such as polyethylene glycol , sodium dodecyl sulfide, thioglycerol, and hexadecyltrimethylammonium bromide (CTAB) are used as stabilizing reagents in order to control the direction and the extent of the particle growth and to manipulate the optical and structural characteristics of the nanomaterials [93–95]. In comparison to other surfactants, CTAB is less toxic and a cheaper alternative as a capping agent which is significantly utilized for the synthesis of CdS colloidal particles. It is cationic consisting of a hydrophobic tail and a positively charged ammonium (NH_4) head group with bromide anion (Br^-) [96]. Although it shows promising results for the synthesis of photocatalysts and extensively studied in the literature as a simple option to manipulate photocatalytic behavior, its potential as an overlayer is not promoted enough. Li *et al.*[97] used CTAB on Fe_2O_3 photoanode by a hydrothermal deposition method followed by a post-annealing. They reported impressive results for photocurrent density increase and enhanced charge separation. They proposed a working mechanism where Br^- of CTAB acts like a redox mediator at the photoanode-electrolyte interface via attaching to the surface through a hydrogen bonding interaction formed on the Fe_2O_3 surface. They supported this hypothesis by TPC and EIS where photocurrent density of pristine Fe_2O_3 showed a significant increase and a lower charge transfer resistance. A different approach was reported by Sun *et al.*[98] where they designed a 2D WSe_2 p-n junction by electron doping with CTAB. They conducted computational studies on both Wse_2 and WS_2 to study the adsorption behavior of CTAB on transition metal dichalcogenides. Their calculations showed that the carrier density of CTAB treated WS_2 was higher than that of pristine one and they attributed this result to the sulfur vacancy (S_v) sites occupied by Br^- which acted like an electron dopant to give p-type characteristic to the junction structure.

Inspired by these studies, we report a simple synthesis route of bare CdS and CTAB treated CdS photoanodes using hydrothermal deposition and dip-coating methods to enhance the OER activity of CdS. We aim to discuss the potential-dependent charge transfer and utilization properties of the photoanodes by probing the transient behavior with LSV under chopped illumination. Results demonstrate that CTAB has a positive effect on inhibiting hole accumulation by acting like a hole-collecting layer on the surface. Several PEC and structural characterization techniques were applied to propose an adsorption mechanism for CTAB. We synthesized 2

different CdS/CTAB photoanodes to investigate the effect of the CTAB overlayer amount by changing the dip-coating time. We studied the surface reaction kinetics of CdS by in situ photoluminescence, EIS, and TPC measurements to provide a detailed analysis on the reactions taking place at the photoanode/electrolyte interface and how these reactions affect the OER efficiency.

3.2 Experimental

3.2.1 Materials and Chemicals

$Cd(NO_3)_2.4H_2O$ (≥98%) , NH_2CSNH_2 (≥99.0%) , $C_{16}H_{33}N(CH_3)_3Br$ (≥98%), NaOH, Na_2SO_3, and H_2O_2 (34.5-36.5%) were purchased from Sigma-Aldrich. Fluorine doped tin oxide (FTO)-coated glass substrates were purchased from Ossila. All electrolytes and solutions used in the synthesis and characterization experiments were prepared with deionized (DI) water.

3.2.2 Synthesis of CdS Photoanodes

Fabrication of FTO/CdS Photoanodes

The CdS photoanodes were prepared using a surfactant-free hydrothermal deposition method inspired by the procedures reported elsewhere [99,100]. 0.8543 $Cd(NO_3)_2.4H_2O$ (1.2 mmol) and 0.3875 g thiourea (2.4 mmol) were dissolved in 40 ml DI water and stirred for 20 min. until the mixture became homogeneous. The FTO substrate was cleaned by sonication in acetone, ethanol, and DI water for 10 min. each. The cleaned FTO substrate was placed on its conductive side facing down in a Teflon sealed stainless-steel autoclave. The reaction solution was transferred to the autoclave and kept at 200 °C for 8 h. Subsequently, the resulting sample was washed with DI water multiple times and annealed at 400 °C for 1 h at a heating rate of 5 $°C.min^{-1}$ under continuous nitrogen flow in a tubular furnace.

Fabrication of FTO/CdS/CTAB Photoanodes

As prepared CdS photoanodes were coated with CTAB by using a facile dip-coating method[101]. 0.03 M CTAB solution was prepared by dissolving 0.34 g CTAB in 30 ml DI water. The mixture was stirred until it was completely homogeneous. The hydrothermally deposited CdS photoanodes were placed vertically in the CTAB solution during continuous stirring to prevent the precipitation of CTAB. The amount of

CTAB overlayer was controlled by increasing the dip coating time. After the dip-coating, the photoanodes were dried at 60 °C for 8 h.

Fabrication of CTAB Treated Powder CdS for TEM

CdS nanorod powder samples were prepared using the same hydrothermal synthesis procedure. After the synthesis, CdS dispersed in DI water was collected from the bottom of the autoclave. The mixture was washed and centrifuged with ethanol and DI water to remove impurities or unreacted precursors. Subsequently, the powder was dried in the oven at 60 °C for 8 h. The resulting product was annealed at 400 °C for 1 h with a heating rate of 5 °C.min^{-1} under continuous nitrogen flow. 65 mg CdS powder was weighed and kept in 1.5 ml 0.03 M CTAB solution stirring continuously at 90 rpm for 6 h. After CTAB treatment, the CTAB/CdS powder was collected and dried in the oven at 60 °C for 8 h.

Creating S_vs on CdS Photoanode Surface

To confirm the proposed adsorption behavior of CTAB on CdS surface, a simple method [102] was used to create S_v on the CdS surface. As prepared bare CdS photoanodes were dipped in 5 M H_2O_2 solution for 60 s and left air drying overnight.

3.2.3 Photoelectrochemical Characterization

All PEC experiments were performed using a Biologic VSP300 potentiostat and a 3-electrode configuration where Ag/AgCl is the reference electrode, Pt is the counter electrode, and CdS is the working electrode in a quartz cell purchased from Pine Research. 0.1 M NaOH (pH = 12.87) was used as electrolyte in all experiments. All potentials in the graphs were converted to the reversible hydrogen electrode (RHE) scale using the Nernst Equation [103]. ECSA of the photoanodes were determined by double layer capacitance measurements. CV scans were recorded in dark using different potential scan rates between 25 and 400 mV/s. Current density differences in cathodic and anodic cycles were plotted against the potential scan rates and the slope of this plot was used to compare the ESCA .An Oriel LCS-100 solar simulator with a 1.0 Sun AM 1.5G filter and a 100 W Xe lamp was used as the light source for LSV, EIS, and OCP experiments. IPCE measurements were performed by using a 300 W Xe lamp with a Newport monochromator as the light source.

3.2.4 Structural and Surface Characterization

Bruker D2 Phaser X-Ray Diffractometer was used to identify crystal phase purity of the photoanodes via XRD. Surface electronic structure of the photoanodes were analyzed by using a Thermo K-alpha XPS instrument with a Al Kα light source. FTIR measurements were done by using a Thermo Scientific iS10 FT-IR instrument. A Shimadzu UV-3600-UV-Vis-NIR Spectrophotometer was used to measure the reflectance of the photoanodes. The reflectance values were transformed to absorbance by using Kubelka-Munk calculation [104]. The absorbance data was used to determine the band-gap energy of the photoanodes. In-situ PL emission experiments were performed by using a FLS1000 spectrometer from Edinburgh Instruments. A Zeiss Evo LS15 field emission scanning electron microscope and energy dispersive EDX was used to analyze morphology of the photoanodes and their elemental composition. HRTEM images and HRTEM-EDX spectroscopy were performed for elemental mappings by using a Hitachi HF5000 200kV high resolution transmission electron microscope.

3.3 Results & Discussion

Surfactant-free hydrothermal synthesis of CdS photoanodes and modification of the CdS surface with CTAB after the synthesis by dip-coating method was successfully performed. Dip-coating time of CdS/FTO photoanodes was set as 2 and 6 h to see how the amount of CTAB overlayer changes with dip-coating time. The successful deposition of CdS and CTAB was investigated by XPS, FTIR analysis and HRTEM imaging, which is shown in Figure 3.1.

The control over the CTAB overlayer growth is verified by the Br 3d spectrum in Figure 3.1a where the intensity of Br 3d peak located at 68.3 eV [105] increases with longer dip-coating time. The atomic percent of Br was calculated as 10.5% after 2 h, and 22.4% after 6 h of dip-coating. The photoanode with lower and higher atomic percentage of Br will be denoted as CdS/CTAB1 and CdS/CTAB2, respectively. Figure 3A.1a and 3A.1b demonstrates Cd 3d and S 2p XPS spectra of bare CdS after hydrothermal deposition and the effect of CTAB adsorption on their intensities. The spin-orbit split Cd 3d peaks at 411.8 eV (Cd $3d_{5/2}$) and 405.3 eV (Cd $3d_{5/2}$) and S 2p peaks at 162.6 eV (S $2p_{3/2}$) and 161.4 eV (S $2p_{1/2}$) confirm the stoichiometric CdS formation. In addition to the evolution of Br 3d peaks, the gradual decrease in Cd 3d

and S 2p peak intensities also shows the presence of CTAB overlayer on the CdS surface[106]. Notice that the Br 3d peak intensity difference between CdS/CTAB1 and CdS/CTAB2 is higher than that of S 2p and Cd 3d. This might be the case if CTAB molecules are not covering the surface as a well distributed monolayer.

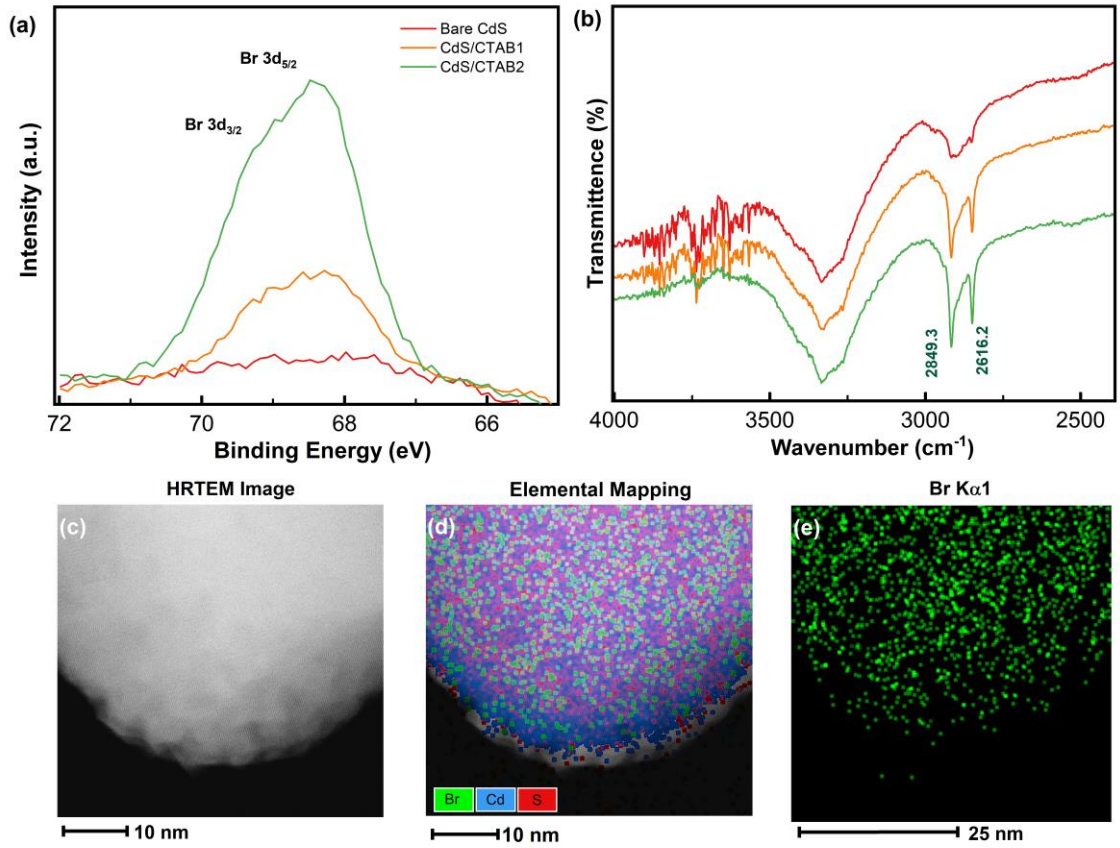

Figure 3.1 *XPS of (a) Br 3d, and (b) FTIR spectrum of bare CdS, CdS/CTAB1, and CdS/CTAB2. (c) HRTEM image of CdS/CTAB2 powder sample, (d) EDX elemental mapping of Br, Cd, and S, and (e) Br $K_{\alpha 1}$ elemental mapping.*

The increase in C 1s peak intensity presented in Figure 3A.1c and the appearance of symmetric and asymmetric C-H stretching bands at 2616.2 and 2849.3 cm^{-1} in Figure 3.1b show the presence of the hydrophobic tail of CTAB[107]. It can be anticipated that CTAB is adsorbed on the CdS surface together with Br^- and hydrophobic tail. It is known that CdS is sensitive to surface oxidation even if it is kept in the dark. The peak located at 168.4 eV in S 2p spectrum must be considered to investigate the effect of CTAB on surface oxidation of CdS. This peak is attributed to SO_4^{2-} which is an oxidation product of S^{2-} on the surface [108]. Note that SO_4^{2-} peak intensity is the highest in bare CdS and lowest in CdS/CTAB2. This is an indication that CTAB decreases

surface oxidation of CdS. The disappearance of CO_3^{2-} peak at 288.5 eV [109] after CTAB treatment also confirms suppressed surface oxidation.

The homogeneity of surface coverage by CTAB is further confirmed by HRTEM and elemental mapping done by EDX. A CTAB treated powder CdS was prepared for HRTEM analysis. HRTEM image, the elemental mapping, and Br $K_{\alpha 1}$ mapping are shown in Figure 3.1. Elemental mapping results showed the homogeneous distribution of Br on the CdS surface.

The phase purity of the photoanodes was determined by XRD (Figure 3A.2). All photoanodes showed the characteristic peaks of the hexagonal wurtzite crystal structure of CdS with a preferential growth in the (002) plane direction[110] which is consistent with the FESEM images presented in Figure 3A.3 where vertical growth of CdS nanorods on the FTO surface is shown. CTAB dip coating did not change the morphology of the photoanodes, but it made the surface rougher and granular. The change in overall surface texture can be attributed to homogeneous surface coverage by CTAB. FESEM-EDX analysis was performed for the CTAB treated photoanode. The EDX spectra of CdS/CTAB1 and CdS/CTAB2 are in strong agreement with the elemental mapping analysis. However, the difference of Br peak intensities is not as prominent as in XPS due to the longer probing depth of FESEM-EDX.

PEC activities of the photoanodes were determined by chopped-light illumination LSV in 0.1 M NaOH electrolyte with a 10 $mV.s^{-1}$ scan rate where a mechanical chopper was used to cut the light with 5 second on/5 second off intervals. The reason why a hole scavenger-free electrolyte was preferred is that sacrificial agents can mask the important information in PEC characterization experiments since the reaction with photogenerated holes and scavenger species is more dominant than other charge utilization processes. Na_2SO_3/Na_2S is the widely accepted electrolyte couple for CdS photoanodes to benefit from the corrosion recovery effect of Na_2S on CdS and effective carrier extraction with Na_2SO_3 as a hole scavenger [111,112]. Although this electrolyte suppresses the photo-corrosion by preventing the reaction of holes with CdS, monitoring the accumulation of charge carriers or charge-trapping processes at the photoanode-electrolyte interface can be challenging.

As can be seen in Figure 3.2a, adsorption of CTAB on CdS the surface leads to a gradual increase in the photocurrent. This improvement might have different origins, i.e. increased surface activities in terms of charge utilization and improved light absorption properties upon CTAB absorption. For this reason, UV-Vis Spectroscopy was first performed to investigate the effect of CTAB on the light absorption characteristics of CdS. Band-gap energies of the photoanodes were calculated by using Tauc analysis which was explained in Chapter 2. Tauc plots of the photoanodes are given in Figure 3A.4a with their band-gap energies. Results show that CTAB modification does not have a significant effect on the band gap energy. It is calculated as 2.42 for the bare CdS which is consistent with the literature [113]. IPCE of all photoanodes were measured at 1.2 V, within the same wavelength range as UV-Vis spectroscopy (Figure 3A.4b). We note that IPCE can be defined as a function of photon absorption efficiency (η_{abs}), charge carrier transport efficiency (η_{tr}), and interfacial charge injection efficiency (η_{inj}) [63]. Since CTAB does not create a significant change in the band-gap energy of bare CdS, IPCE drop shows similar wavelength dependence suggesting that CTAB adsorption had no effect on η_{abs}. A relatively small increase in IPCE for CdS/CTAB1 and CdS/CTAB2 above the absorption edge could then be associated with η_{tr} and η_{inj}. In order to investigate how double layer capacitance changes with CTAB treatment, ECSA was measured by CV measurements at different scan rates and CTAB adsorption appears to reduce ECSA of the photoanodes, which can be attributed to the occupation of the surface sites (Figure 3A.5).

In Figure 3.2a, the hole transfer, accumulation, and extraction behavior of the photoanodes can be monitored from the transient behavior of photocurrent density. Starting from 0.2 V, there is an anodic spike every time the photoanode is illuminated, and these spikes are followed by a decay in photocurrent density. The anodic spikes are continuously increasing as more holes are being utilized with the anodic potential sweep and the photocurrent reaches to 2.47 $mA.cm^{-2}$ at 1.1 V which is rather promising for bare CdS photoanodes in a scavenger-free alkaline electrolyte. Results demonstrate that as the CTAB amount increases, the photocurrent density at anodic spikes also increases. In the reported TPC experiments, these anodic jumps and the subsequent decay is associated with the formation of photogenerated charge carriers and accumulation of holes at the photoanode-electrolyte interface, respectively [114]. After the positively charged holes are produced by CdS, they start to migrate to the surface with the band

bending effect [115]. However, especially in photoanodes with strong light absorption properties like CdS, charge carrier formation goes to a high extent which can result in surface charge recombination. Depending on the surface states, this type of behavior can be attributed to an electron trap center on the photoanode surface. This will be discussed later in the text. In Figure 3.2b, the hole accumulation kinetics was investigated by estimating the photocurrent decay rates after each anodic jump. For the bare CdS, the photocurrent decay rate increases up to 0.77 V and then it becomes slower as the potential increases. The potential where the decay rate starts to decrease shows a cathodic shift for the CTAB treated photoanodes indicating the enhanced OER kinetics. At potentials below 0.66 V, the decay rate of CdS/CTAB1 and CdS/CTAB2 are close to each other. Whereas above 0.66 V, the decay rate of CdS/CTAB2 is the lowest at all potentials with higher applied bias. In the proposed adsorption mechanism of CTAB which is shown in Figure 3.2d, Br− occupies the surface sulfur vacancies as mentioned before. Therefore, the decreased decay rate with CTAB shows that sulfur vacancies has an important role for the activity loss of CdS.

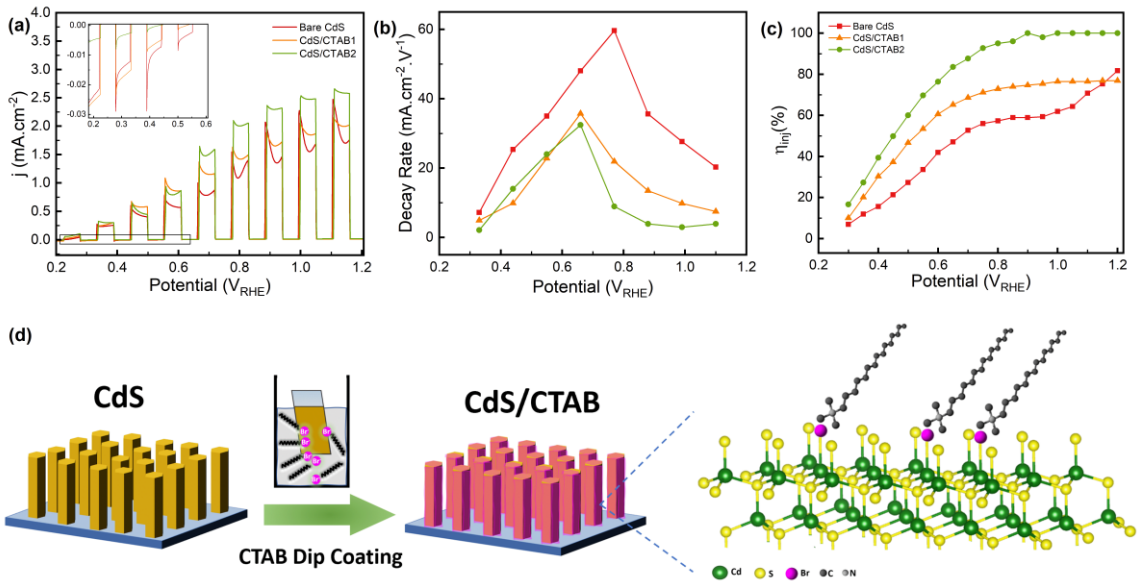

Figure 3.2 *(a) Chopped-light illumination LSV, (b) decay rates of the photocurrent after the anodic spike, (c) η_{inj} of are CdS, CdS/CTAB1, and CdS/CTAB2. (d) The schematic representation of the adsorption model of CTAB on CdS after dip coating.*

Generally, photocurrent density is expected to reach a steady state after this decay when the production of charge carriers and the injection of holes to the electrolyte are in equilibrium. However, starting from 0.2 V, another anodic increase after the initial

photocurrent decay is observed. This pattern, photocurrent density going through a dip, repeats itself between 0.2 V to 1.2 V which means that there is a change either on the photoanode surface or the ionic species at photoanode/electrolyte interface. This type of behavior has been reported for different photoanodes before [116,117], but very little information regarding its potential dependence is available. It is known that CdS is sensitive to chemical and light-induced corrosion during PEC experiments. Especially in electrolytes without a hole scavenger, it can dissolve to the electrolyte as Cd^{2+} and S^{2-} [51,118]. S^{2-} are electrochemically unstable ions, and they can easily undergo oxidation under applied anodic bias. Caliari *et al.* [119]reported that electrochemical oxidation of S^{2-} to SO_4^{2-} takes place at potentials between 0.475 V and 1 V during anodic potential sweep which is consistent with Figure 3.2a where the anodic increase after the decay starts from 0.7 V Since the oxidation peak after the photocurrent decay is in the same potential window, we attribute this behavior to the oxidation of sulfide which is dissolved from the CdS due to photocorrosion.

In addition to this anodic behavior after photocurrent dipping under illumination, there is a cathodic spiking between 0.2 and 0.7 V when light is turned off (inset of Figure 3.1a). This overshoot can be explained by the recombination of holes and electrons at the surface when photoexcitation is interrupted. It starts from 0.2 V in bare CdS and shows a gradual decrease until it disappears completely at 0.7 V. There is a correlation between these cathodic cathodic spikes and S^{2-} oxidation peaks because as mentioned above, lesser overpotential required for S^{2-} oxidation so holes can be consumed more rapidly to react with dissolved S^{2-} in the electrolyte It means there is no unreacted holes remaining on the surface to give a cathodic spike when light is off. and Another factor that contributes to suppressed cathodic spikes is the enhanced charge separation at higher potentials which facilitates water oxidation. However, the cathodic spikes disappear as the sulfide oxidation peaks start to form. This can be an indication that sulfide S^{2-} oxidation contributes to this trend of cathodic spikes when light is off. The intensity of cathodic spikes decreases significantly in CdS/CTAB1 and they almost disappear in CdS/CTAB2. It shows the improvement in surface charge recombination with CTAB overlayer corresponding to boosted charge separation and utilization. This effect of CTAB on cathodic overshoots can be associated with less surface charge recombination as well.

In addition to chopped-light LSV measurements, photoanodes were tested under continuous illumination in the presence and absence of Na_2SO_3 hole scavenger (Figure 3A.6a and 3A.6b) to investigate potential dependent evolution of η_{inj}. In Figure 3.2c, more efficient utilization of photogenerated holes in the presence of CTAB is evident. CTAB acts like a hole extracting layer on the surface, suppressing the accumulation of holes at the photoanode/electrolyte interface, however, this role appears to be valid up to 0.7 V. The possible reason for steady η_{inj} at higher potentials could be provided by EIS investigations.

EIS was performed to investigate the change in charge transfer resistance at the photoanode/electrolyte interface (R_{CT}) with the anodic and cathodic spikes through the anodic sweep. The details of the measurements and fittings of the Nyquist plots are given in Figure 3A.7. In Figure 3.3a, it is shown R_{CT} of bare CdS decreases with CTAB treatment and CdS/CTAB2 has the lowest R_{CT}, which is consistent with the LSV measurements. However, the potential dependent behavior of R_{CT} of the photoanodes shows a surprising trend.

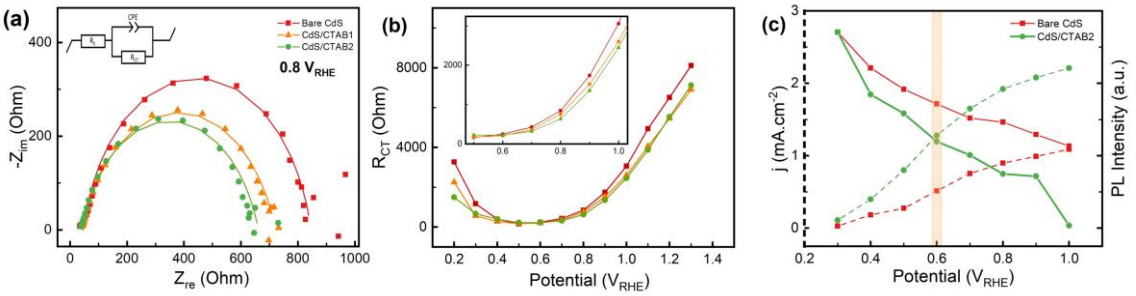

Figure 3.3 *(a) Nyquist plots recorded at 0.8 V and (b) the potential dependent R_{CT} plots of bare CdS, CdS/CTAB1, and CdS/CTAB2. (c) LSV and In-situ PL emission plots of Bare CdS and CdS/CTAB2. The PL measurements were done by using the same 3-electrode configuration of PEC experiments in a quartz spectroscopy cuvette. The PL emission intensities were normalized with respect to the emission at 0.3 V by peak area integration.*

Figure 3.3b demonstrates that R_{CT} starts to decrease from 0.2 V and reaches to a plateau at 0.5 V for all photoanodes. This steady resistance continues until 0.7 V and starts to increase gradually with applied potential. Through the anodic scan, R_{CT} of the bare CdS is higher than that of CdS/CTAB1 and CdS/CTAB2 except the 0.5 – 0.7 V region. However, R_{CT} is generally expected to decrease with increasing applied potential due to enhanced charge separation and utilization[120]. Since the plots are very close to each other, the comparison of R_{CT} values can be seen more clearly in Table 3A.2. Even though the photocurrent density of all photoanodes increases through the

whole potential range, R_{CT} shows an increase starting from 0.7 V. Note that the change in R_{CT} behavior falls into the same region in LSV measurements where the anodic spikes after the photocurrent dipping under illumination starts. This behavior might have the same origin that S^{2-} ions are highly reactive and they tend to donate their electrons to the photoanode to give an oxidation reaction. The increase in the charge transfer resistance can be associated with the additional resistance resulting from the S^{2-} oxidation products accumulating on the surface. Note that more than one process, such as charge accumulation, OER, and S^{2-} oxidation, take place simultaneously whenever light is on in the chopped light LSV measurements. We consider the S^{2-} oxidation as an activity diminishing factor that is happening simultaneously with OER.

PL emission spectroscopy was used to provide a supporting characterization study for the effect of CTAB. It is a characterization technique which is often used to investigate charge carrier recombination characteristics [121]. In Figure 3.3c the photocurrent density and the in-situ PL emission intensity of bare CdS and CdS/CTAB2 are presented as a function of applied potential. Results demonstrate that the PL emission intensity of CdS/CTAB2 is lower than that of bare CdS at all potentials. Both photoanodes show a gradual decrease in emission intensity as photocurrent density increases, which is expected since the electron-hole recombination is less at higher potentials due to enhanced charge separation. Between 0.3 V and 0.6 V, the emission intensity of CdS/CTAB2 decreases 1.5 times faster than that of bare CdS. After 0.6 V, the normalized emission intensity of CdS/CTAB2 decreases by 4.1% up to 1 V while bare CdS decreases by 2% within the same potential range. This result is consistent with the chopped illumination LSV data where the effect of CTAB is more dominant at potentials above 0.6 V.

Transient behavior of OCP was also investigated to probe the effect of CTAB on photovoltage. The photovoltage change for CdS photoanodes are shown in Figure 3.4a. The OCP of bare CdS is 0.67 V and it decreases with CTAB overlayer. Generally, it is considered as a negative effect for photoanodes, because lower OCP means less self-driven potential for the OER. However, it has been reported elsewhere that the modification of photocatalyst with hydrophilic surface passivation overlayers might result in interfacial dipole formation which shifts the band-edge position and causes lower OCP [122]. After the light is switched on, all photoanodes show a fast OCP decay

with photoexcitation of electrons in VB and subsequent formation of electron-hole pairs [123]. CdS/CTAB2 reaches the lowest potential compared to bare CdS and CdS/CTAB1. Higher photovoltage upon illumination can be attributed to strong light utilization and more photogenerated charge carriers migrating to space-charge region. Notice that, although bare CdS has the highest photovoltage change, it shows a slight decrease during illumination while CTAB treated photoanodes remain flat. It is an indication of lower surface charge recombination and improved injection of photogenerated holes to the electrolyte [124].

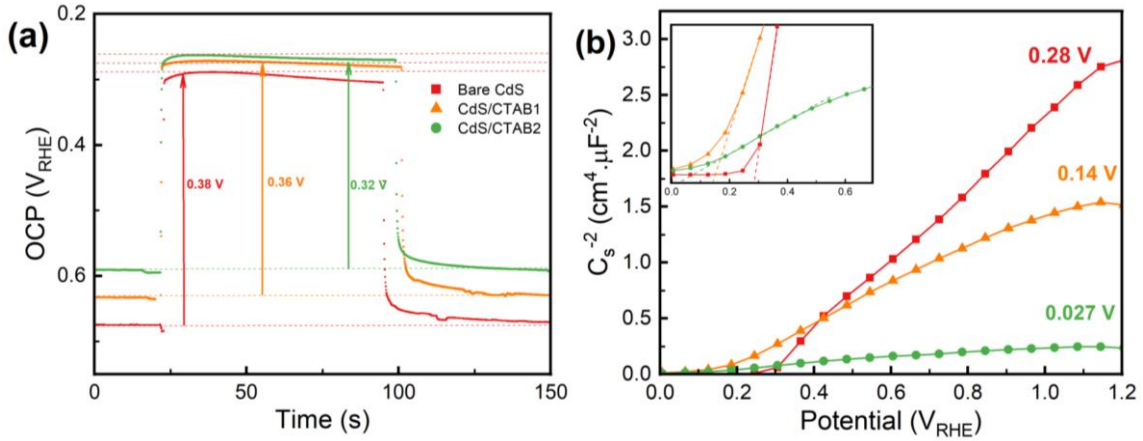

Figure 3.4 *(a) Transient OCP measurements with chopped illumination and (b) Mott-Schottky (measured in dark) plots of bare CdS, CdS/CTAB1, and CdS/CTAB2.*

In Figure 3.4b, MS plots show positive slopes characteristic to n-type semiconductors. Analysis results demonstrate that the V_{fb} displays a cathodic shift from 0.28 to 0.027 V with CTAB treatment in agreement with cathodic shifts in the onset potentials of LSV curves. A more negative V_{fb} upon CTAB adsorption provides a higher quasi-Fermi level of electrons ($E_{F,n}$). Photovoltage then increases due to a greater separation between the quasi-Fermi level of holes ($E_{F,p}$) and $E_{F,n}$. The slope of the MS plot for bare CdS shows a significant decrease with the CTAB treatment. Among all photoanodes, CdS/CTAB2 reveals the smallest MS slope, therefore the highest N_d [125]. For metal oxide semiconductors, it has been reported that increased N_d might be a result of oxygen vacancy defects [126], which can be considered as a similar situation for sulfur vacancies of CdS. We hypothesize that Br^- of CTAB acting as an electron donor fills the surface sulfur vacancies in the surface [127].

Another set of chopped-light LSV measurements was performed to investigate the relation of CTAB adsorption mechanism to surface sulfur content by using the H_2O_2

treated CdS samples. In Figure 3A.8a, chopped-light LSV results show that H_2O_2 treatment decreases the PEC activity of CdS photoanodes (CdS_S_v). S_vs are the abundant n-type defects of CdS [128]. At an optimum level, they can enhance the charge carrier mobility in bulk phase [52]. However, surface S_vs can act like electron trap centers and cause surface charge recombination which decreases the photocurrent density. This can be the reason for deactivation after H_2O_2 treatment. After the surface S_v formation, the photoanodes were kept in 0.03 M CTAB solution for 2 h like CdS/CTAB1 (CdS_S_v/CTAB). According to the chopped-light LSV results, at 1.1V 2h CTAB treatment increases the photocurrent density of CdS_S_v and bare CdS by 98% and 52% respectively. It is consistent with our hypothesis where CTAB is adsorbed on the surface by occupation of surface S_v with Br^-. Additional S_vs created make more binding sites available for CTAB adsorption, and it can further enhance the charge utilization. In Figure 3A.9a and S9b, Cd 3d and S 2p XPS spectra and the change in Cd and S species after H_2O_2 treatment are given, respectively. The gradual decrease in the S 2p and Cd 3d peaks, and the shift towards higher binding energy is attributed to sulfur vacancy formation [129]. The S_v content is calculated based on a method reported for CdS [42] and an increase in the amount of surface S_v with H_2O_2 treatment is shown in Table S1. Br 3d XPS spectra in Figure 3A.9c show that the amount of Br on CdS_S_v/CTAB is higher than that of CdS/CTAB1. This is in strong agreement with our adsorption hypothesis of Br^- on CdS surface.

For CdS_S_v, the photocurrent decay observed after the anodic spikes upon illumination is less intense than the pristine CdS. In Figure 3A.8a, 0.7 V and 0.8 V are given as highlighted regions. Notice that, in the first area, CdS_Sv does not show the anodic peak after the photocurrent decay, which was defined as the dip behavior. It indicates that H_2O_2 treatment leads to a cathodic shift in the dip behavior which is associated to dissolved S^{2-} oxidation. In region, the photocurrent decay after the anodic jump is highlighted and the decay rates were calculated as in Figure 3.2b. Results showed that the decay rate of bare CdS is 2 times higher than that of Cd_Sv which is in strong agreement with the interpretation of TPC behavior in chopped light LSV measurement. Moreover, the photocurrent density after the dip increases by 9.4% and 40% for CdS_S_v and bare CdS, respectively. Since the CdS_Sv surface has an increased number of S_vs, less photo-corrosion induced S^{2-} is released to the electrolyte and thus less S^{2-} undergoes oxidation reaction on the photoanode surface to cause faster

photocurrent decay and increased interfacial R_{CT}. Moreover, MS analysis results shown in Figure 3A.8c and 8d reveal that CdS_S_v and CdS_S_v/CTAB photoanodes have higher N_d than bare CdS and CdS/CTAB1, respectively. Therefore, N_d is correlated with the amount of surface S_vs and coverage of CTAB overlayer.

Within the light of PEC and structural characterization experiments, S^{2-} oxidation hypothesis was tested in detail by transient chronoamperometric measurements to reveal the mechanistic fingerprints of the elementary steps. Chronoamperometric (CA) TPC experiments were conducted to further analyze the photocorrosion and photocurrent density decay behavior by using 250 ms on 250 ms off light pulses with an LED light source at 0.7V. The CA-TPC results of bare CdS and CdS/CTAB2 is shown in Figure 3.5. Notice that the anodic jump, subsequent decay, the second anodic event which we associated with sulfide oxidation, and the cathodic overshoot when light is off are consistent with the chopped illumination LSV results. However, what is unexpected is the wiggle-like periodic cathodic events during steady state photocurrent.

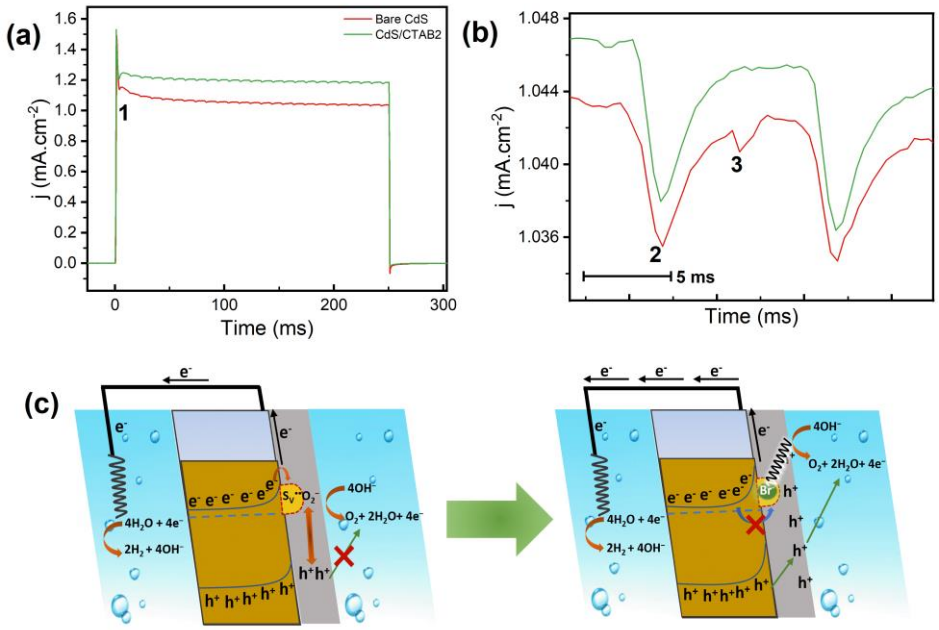

Figure 3.5 *(a) CA at 0.7 V with 250 ms white LED light pulse of bare CdS and CdS/CTAB2, (b) stacked inset of the wiggle behavior during steady state, (c) schematic representation of the effect of CTAB on surface charge trapping passivation.*

In Figure 3.5.b, a stacked inset of one wiggle which takes almost 10 ms is shown with 2 cathodic events numbered as 2 and 3. We propose the trapping mechanism

below, which can explain the periodicity of 2 cathodic events and the relation between S^{2-} dissolution and activity loss.

Water Oxidation Mechanism

$$CdS \rightarrow e^- + h^+$$

$$* + OH^- + h^+ \rightarrow *OH$$

$$*OH + OH^- + h^+ \rightarrow *O + H_2O$$

$$*O + OH^- + h^+ \rightarrow *OOH$$

$$*OOH + OH^- + h^+ \rightarrow O_{2\,(g)} + H_2O$$

Photocorrosion and Electron Trapping Mechanism

$$CdS \rightarrow Cd^{2+}_{(aq)} + S^{2-}_{(aq)}$$

$$CdS \rightarrow CdS\text{-}S_v^{\bullet\bullet} + S^{2-}_{(aq)} \quad \textbf{(1)}$$

$$S^{2-}_{(aq)} + 2h^+ \rightarrow S^0$$

$$2S^{2-}_{(aq)} + 3O_{2\,(g)} + H_2O + 4h^+ \rightarrow 4SO^{2-}_{4\,(aq)}$$

$$CdS\text{-}S_v^{\bullet\bullet} + e^- \rightleftharpoons CdS\text{-}S_v^{\bullet} \quad \textbf{(2)}$$

$$CdS\text{-}S_v^{\bullet} + O_{2\,(g)} \rightleftharpoons CdS\text{-}S_v^{\bullet}\text{-}O_2$$

$$CdS\text{-}S_v^{\bullet}\text{-}O_2 \rightleftharpoons CdS\text{-}S_v^{\bullet\bullet}\text{-}O_2^-$$

$$CdS\text{-}S_v^{\bullet\bullet}\text{-}O_2^- + e^- \rightarrow CdS\text{-}S_v^{\bullet\bullet}\text{-}O_2^{2-} \quad \textbf{(3)}$$

$$CdS\text{-}S_v^{\bullet\bullet}\text{-}O_2^{2-} \rightarrow CdS\text{-}S_v^{\bullet\bullet} + O_2^{2-}$$

$$O_2^{2-} + 2h^+ \rightarrow O_{2\,(g)} \quad \textbf{(4)}$$

As mentioned before, the dip behavior in TPC is related to light-induced sulfide dissolution and oxidation at the photoanode surface which is shown in equation 1 above. When the photoanodes reach to steady state, there are 2 cathodic events which are shown in equations 2 and 3. In our proposed mechanism, we included the S_vs formed by photo-etching when sulfide ions dissolve to the electrolyte. These S_vs are possible sites for electron trapping and can contribute to activity loss. However, it has been reported that the energy level of S_v is located between Fermi level and the

conduction band minimum which makes them unstable trap sites meaning that the trapped electron can go to CB easily by thermal excitation [41,116]. Moreover, equation 2 itself does not explain 2 cathodic events and the periodic trend of the wiggle movements. At this point, O_2 coming from OER which can sit on the electron trapped in S_v is included in the mechanism. The reason why oxygen is included is that, after taking the trapped electron and becoming a superoxide which is known to be very reactive, it can take a second electron to go to peroxide as the second cathodic event shown in equation 3. Notice that this event disappears in CdS/CTAB2 because of the occupancy of sulfur vacancies with Br^-. In this way, photogenerated holes and electrons can go for OER and HER instead of giving recombination at the surface due to electron trapping. What makes this process periodic is that, after taking −2 valancy, O_2^{2-} can leave the vacancy and give OER reaction via equation 4.

In the photocorrosion and electron trapping mechanism, there are 3 important parameters that can change the extend of trapping: potential, light intensity, and illumination time. The change in potential can manipulate the amount of oxygen coming from OER and the last 2 parameters can be used to tune the amount of S_vs which are the primary trap states. In order to show the effect of these parameters 3 CA experiments were conducted by using bare CdS as the control sample. In Figure 3A.10.a, 250 ms on 250 ms off pulse experiment at 3 different potentials is shown. Notice that as the potential increases the intensity of cathodic events increase as well. Normally, if there is a trapping event which is caused only by a trap state, it is expected to decrease with applied potential. However, it is vice versa for CdS, which is consistent with our hypothesis where the O_2 coming from OER is a part of the trapping mechanism. At high potentials, OER goes to a higher extend which means that there are more O_2 near the photoanode surface to go for the electron trapped sulfur vacancies. Secondly, we performed the same experiment at 2 different light intensities. Since the sulfur vacancy formation on the surface depends on light-induced etching, it can be said that more sulfur vacancy sites form after higher light intensity illumination. More sulfur vacancies are possible trap sites to increase surface charge recombination and cathodic events. The result in Figure 3A.10.b and the PEC activity decrease after H_2O_2 treatment in Figure 3A.8a are confirming this hypothesis as they both show the negative effect of surface sulfur vacancies. Lastly, the effect of light-induced sulfur vacancy formation is investigated by changing the illumination time at 0.7 V. Similar to light intensity

dependent experiment, it is expected to have more sulfur vacancies as the sample is illuminated for longer time. In this experiment, the light intensity is increased to see the change in steady state photocurrent with longer illumination time.

For 50 ms and 150 ms long illumination measurements, there was no cathodic spike when light is off, which is consistent with the chopped-light LSV measurements. However, a cathodic spike appears at 500 ms and continues to increase until 1200 ms at where it reaches a maximum. The reason for the cathodic overshoots when light is off is explained as the recombination of remaining holes on the surface with electrons. Notice that the photocurrent density at each anodic jump, and the steady state photocurrent are decreasing between 50 to 1200 ms. Both lowered photocurrent density and increasing cathodic overshoot are the signs of surface charge recombination caused by electron trapping. The result confirms Figure 3A.10b which shows that when more surface sulfur vacancies form by photoetching, electron trapping goes to a high extent. Another finding of this TPC experiment is that the cathodic overshoots start to decrease after 1200 ms illumination meanwhile the steady state photocurrent starts to increase. For the chopped illumination LSV experiment, we associated the anodic event after photocurrent decay with the S^{2-} oxidation. It is important to note that longer illumination time not only creates sulfur vacancies on the surface but also causes more dissolution of S^{2-} ions which can undergo electrochemical oxidation at 0.7 V. This reversed trend of cathodic overshoot and the steady state photocurrent density can be attributed to this electrochemical process which was also confirmed by EIS measurements.

3.4 Conclusion

In summary, the effect of CTAB overlayer amount on CdS photoanode surface and the fundamental charge transfer and utilization mechanisms of bare CdS was investigated in detail by TPC and potential dependent EIS measurements. We proposed a surface charge trapping mechanism for TPC decay behavior, which was further confirmed by short light pulse CA measurements. CTAB overlayer coating was presented as a facile approach to passivate the surface charge trapping and electron-hole recombination processes, which was proved by LSV, TPC, and in-situ PL spectroscopy. To investigate the adsorption mechanism of CTAB on CdS surface, both bare and surface sulfur vacancy rich CdS photoanodes were analyzed by XPS before and after

CTAB treatment to see the change in surface composition. We believe that this work can be an important insight for research on CdS photoanodes by providing a fundamental understanding of key processes taking place at photoanode/electrolyte interface.

Chapter 4:

Effect of Ultrathin ALD TiO_2 Overlayer on Charge Transfer and Utilization Properties of CdS Photoanode

4.1 Introduction

Surface charge recombination is one of the most critical processes that contribute to PEC activity loss of CdS. It can be resulted from poor charge separation of the photoanode material where electrons and holes recombine on the surface instead of transferring to the electrolyte to drive HER or OER. It can be the indication of a trap state on the surface as well. This issue is demonstrated for different photoanodes such as Fe_2O_3, $BiVO_4$, and WO_3 [130–132]. One of the most widely studied surface modification strategies to overcome these challenges is the passivation overlayers which can be chosen from inorganic materials such as Al_2O_3, TiO_2, ZnS, CeO_x [133–136] or organic materials [137]. The main purpose of passivation overlayers is to reduce the number of defect sites on the surface which is the bottle neck of improving the light-induced activity loss. There are different ways to deposit passivation overlayers such as dip-coating, chemical bath deposition, plasma enhanced deposition, and atomic layer deposition (ALD) [138–140]. Among all options, ALD is a good choice since it allows deposition of ultrathin, controllable, and uniform layers [141].

In the literature, passivation overlayers are mostly used with metal oxide semiconductors because of their oxygen vacancy defects which serve as recombination centers between VB and CB [142]. As an example, $BiVO_4$ is often combined with passivation overlayers since it is a simple post-synthesis surface modification method. Ahmed et.al. reported utilization of TiO_2 passivation overlayer on Fe_2O_3 photoanode to enhance the charge transfer and utilization at photoanode/electrolyte interface where they proposed that TiO_2 overlayer blocks the defect sites on Fe_2O_3 and reduce electron-hole recombination [143]. Other than successful studies, there are also papers that reported negative effects of passivation overlayers. Wan *et. al.* studied Al_2O_3 overlayer on $BiVO_4$ which is known for poor charge carrier mobility and surface charge recombination. The results showed that Al_2O_3 deposition decreases the photocurrent density due to high resistance and low conductivity of amorphous Al_2O_3 overlayer [139]. Other than metal oxide surface overlayers, different materials were also utilized for surface passivation such as Nafion. Zheng *et.al.* used polydopamine modified Nafion on

CdS surface to passivate the surface where the surface defects are disabled by Nafion and the surface charge recombination is reduced [90]. TiO_2 is a less studied material for CdS modification as a passivation overlayer. However, TiO_2/CdS heterojunctions have an important place in the literature because their characteristics are completing each other. For example, CdS is a very good light absorber with poor stability and TiO_2 is known for its photo-stability but also its large band-gap energy. When the CdS is deposited on TiO_2 their relative band-edge alignment allows fast charge transfer and injection to the electrolyte, which is very critical to improve activity and stability [144,145].

In Chapter 3 of this study, we proposed a surface charge trapping mechanism for CdS caused by surface sulfur vacancies, both abundant and produced by light induced photocorrosion. Inspired by the application of metal oxide passivation overlayers on different photoanodes and the findings from Chapter 3, we utilized ALD TiO_2 layer with different thicknesses to provide a simple surface modification method to improve the stability and PEC activity of CdS.

4.2 Experimental

4.2.1 Fabrication of FTO/CdS Photoanodes

FTO/CdS photoanodes were synthesized by using the same hydrothermal deposition method described in section 3.2.2.

Fabrication of FTO/CdS/TiO_2 Photoanodes by ALD

Ultrathin TiO_2 layer was deposited on CdS photoanodes by using ALD method. ALD is a deposition method which allows ultrathin coatings by using different precursors in vapor phase [141]. In this study, titanium bis(acetylacetonate) chloride and H_2O were used as Ti and O precursors. In the recipe, H_2O is pulsed for 0.15 s and the surface is sweeped by N_2 with 20 sscm. Afterwards, Ti precursor is pulsed for 1 s with another subsequent sweeping to get rid of the acetylacetonate groups. This process was repeated for different number of cycles to see the effect of TiO_2 overlayer amount on CdS. The deposition was performed at 200 ˚C reactor inlet and outlet temperature.

Structural Characterization Experiments

All instrumental details of the structural characterization experiments in this section are the same as in section 3. Different from Chapter 3, Raman spectroscopy was performed by using a Renishaw Invia- Raman microscope and 532 nm laser light.

4.2.2 Photoelectrochemical Characterization

All PEC experiments were performed with the PEC cell configuration described in Chapter 3. The same experiment parameters were used for chopped light LSV experiments, EIS, MS, and OCP measurements.

4.3 Results & Discussion

Firstly, the successive overlayer deposition of ALD method was confirmed by XPS analysis. Cd 3d, S 2p, Ti 2p, and O 1s spectra of bare and 10-30-50-70-90 cycles of TiO_2 coated CdS samples are shown in Figure 4.1.

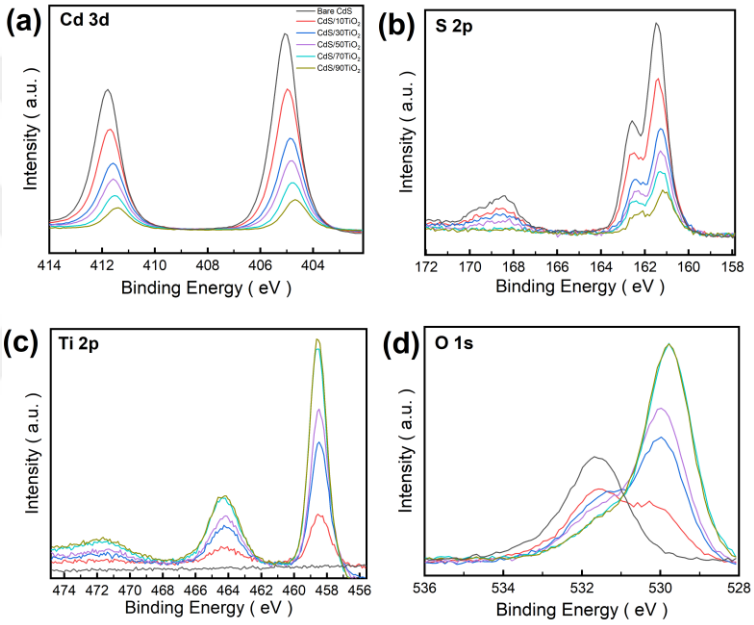

Figure 4.1 *(a)Cd 3d, (b) S 2p, (c) Ti 2p, and (d) O 1s of bare CdS and CdS samples with 10-30-50-70-90 layers of ALD TiO_2 coating.*

As the number of ALD cycles increases, there is a gradual increase in the Ti $2p_{3/2}$ and $2p_{1/2}$ spin orbit coupling peaks located at 458.6 and 464.2 eV. There is also formation of a satellite peak at 471.8 eV which has been reported as a characteristic peak for TiO_2 before [146]. On the other side, the drop in the intensity of Cd 3d and S 2p peaks due to successive surface coverage by ALD TiO_2. In O 1s spectra, there are 2 peaks located at 531.6 and 529.7 eV. The second peak increases as the thickness of TiO_2 overlayer increases. On the other side the O 1s peak located at 531.6 eV decreases as the peak assigned to oxide ion of TiO_2 increases. That peak was assigned to different surface states such as CO_3^{2-} SO_4^{2-},or OH^- resulting from surface oxidation[147,148]. Considering the sensitivity of CdS towards air oxidation, it is expected to have such adsorbed oxygen

species. TiO_2 can be considered as a surface protection layer against CdS oxidation. The second important point about the XPS results is the shift towards negative binding energy in Cd 3d, S 2p and O 1s spectra. This can be attributed to a charge transfer process from TiO_2 to CdS. In the literature, there are examples of electron transfer from TiO_2 to CdS. However, Ti 2p must show a shift towards higher binding energy if there was such electron transfer but it remains unchanged. Considering their relative E_{VB} alignment, which is shown in Figure 4.2 below, the potential scenario is hole transfer from CdS to TiO_2 after ALD deposition.

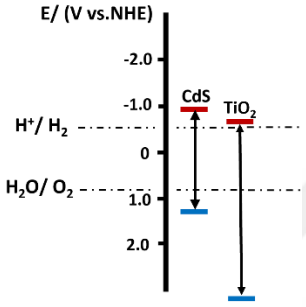

Figure 4.2 *Relative band-edge alignment of CdS and TiO_2.*

After confirming the successive ALD TiO_2 deposition, samples were tested for the PEC activity by chopped illumination LSV at 10 $mV.s^{-1}$ scan rate in 0.1 M NaOH. According to the chopped illumination LSV in Figure 4.3a, a certain amount of TiO_2 increases the activity of bare CdS, which is more visible between 0.4 and 0.8 V when we consider the maximum photocurrent values reached every time light is on. However, this improvement continues till the 50 cycle TiO_2 coated CdS and starts to decrease with thicker TiO_2 on the surface.

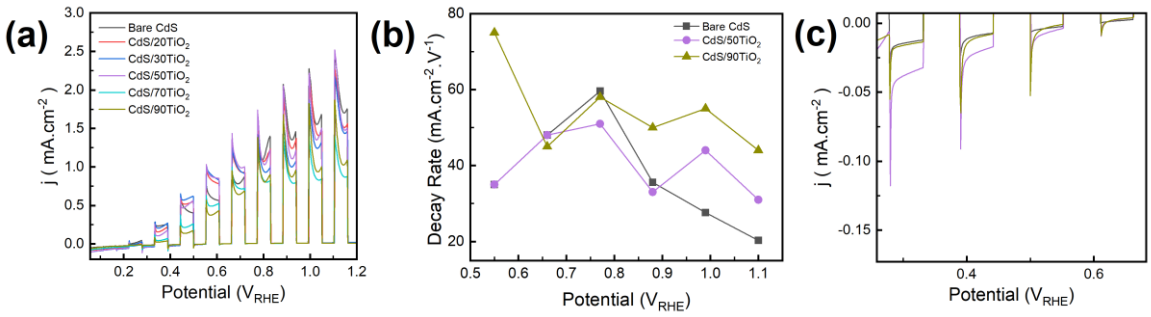

Figure 4.3 *(a)Chopped illumination LSV of bare CdS, and 20,30, 40, 50, 70, and 90 ALD cycle TiO_2 coated CdS in 0.1 M NaOH, (b) decay rates and (c) cathodic spikes (when light is off) of bare CdS, CdS/50TiO_2, and CdS/90TiO_2.*

In the previous chapter, we explained the anodic jumps when light was on as the generation of electron hole pairs and their utilization in HER and OER. Therefore, it can

be said that an optimum thickness of TiO_2 can enhance the charge extraction of bare CdS especially at moderate potentials. It can be anticipated by the boosted charge separation and injection efficiencies at high potentials which can mask the effect of TiO_2 overlayer. However, the effect of TiO_2 after the anodic jump does not match with the hypothesized scenario where TiO_2 can suppress the electron trapping and improve the activity loss. For further PEC and structural characterization, 50 and 90 cyles TiO_2 coated samples were chosen to compare with bare CdS. The samples will be denoted as CdS/50TiO_2 and CdS/90TiO_2. In Figure 4.3b, the decay rate comparison of bare CdS, CdS/50TiO_2, and CdS/90TiO_2 is shown where CdS/90TiO_2 and bare CdS have the fastest and slowest decay rates. Moreover, a similar relation is given in Figure 4.3c where CdS/90TiO_2 has the most intense cathodic spikes when light is off and bare CdS has the lowest. The photocurrent decay behavior was explained by an electron trapping process before. However, it is unlikely that TiO_2 overlayer increases the extent of trapping because the cathodic overshoot of CdS/50TiO_2 is more intense than that of bare CdS, even at the potentials where the photocurrent density of bare CdS is lower. The cathodic overshoot caused by surface charge recombination is expected to be higher when the steady state photocurrent is lower.

The crystal structure of the samples is confirmed by XRD in Figure 4B.1 where all samples showed the characteristic peaks of hexagonal wurtzite structure. No peaks are observed for TiO_2 because of the detection limit of XRD. After the crystal structure analysis, the morphology was checked as well by FESEM in Figure 4.4. The results show that TiO_2 overlayer is not visible in FESEM images because ALD gives a very thin overlayer even with 90 cycles of ALD TiO_2 deposition. However, EDX results of the SEM samples confirm the presence of TiO_2 for both 50 and 90 cycle samples. The increase in Ti peaks and the drop in Cd and S peaks are consistent with the XPS results.

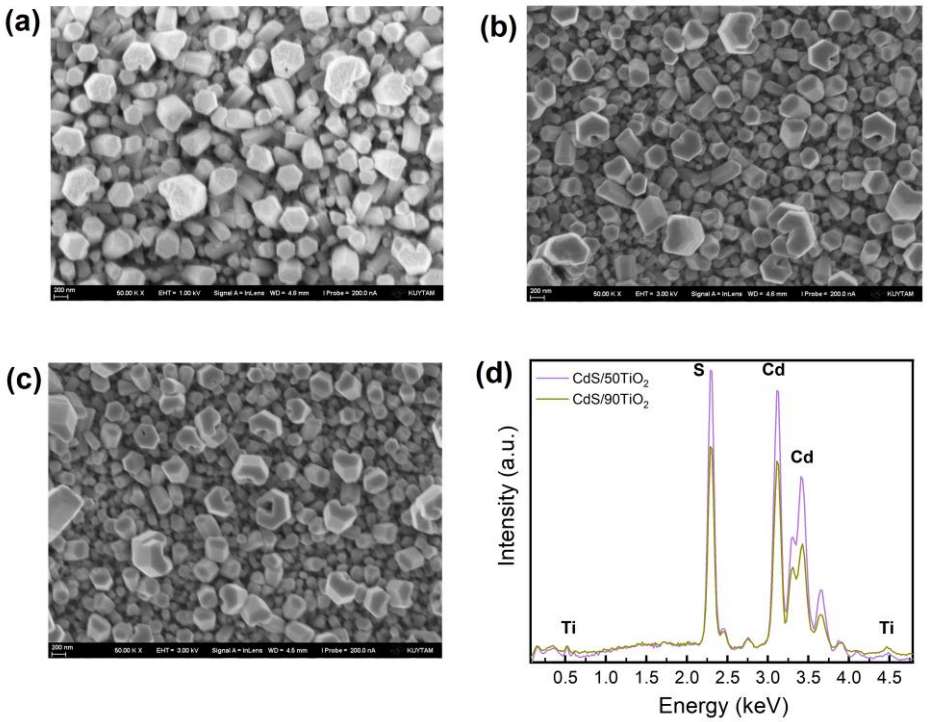

Figure 4.4 SEM images of (a) bare CdS, (b) CdS/50TiO₂, and (c) CdS/90TiO₂. (d) EDX spectra of CdS/50TiO₂, and CdS/90TiO₂.

The optical characteristics of the samples were investigated by UV-Vis and Raman spectroscopy. UV-vis absorbance data was used to see if the improvement with 50 cycles of TiO_2 was originated from a change in the band-gap energy. In Figure 4.5a, the absorbance of CdS is not improved by TiO_2, in fact it decreases. However, it does not have a significant effect on the band-gap energy. The band-gap energies of the bare CdS, CdS/50TiO_2, and CdS/90TiO_2 are calculated as 2.42, 2.41, and 2.41 which all are consistent with the literature value of CdS.

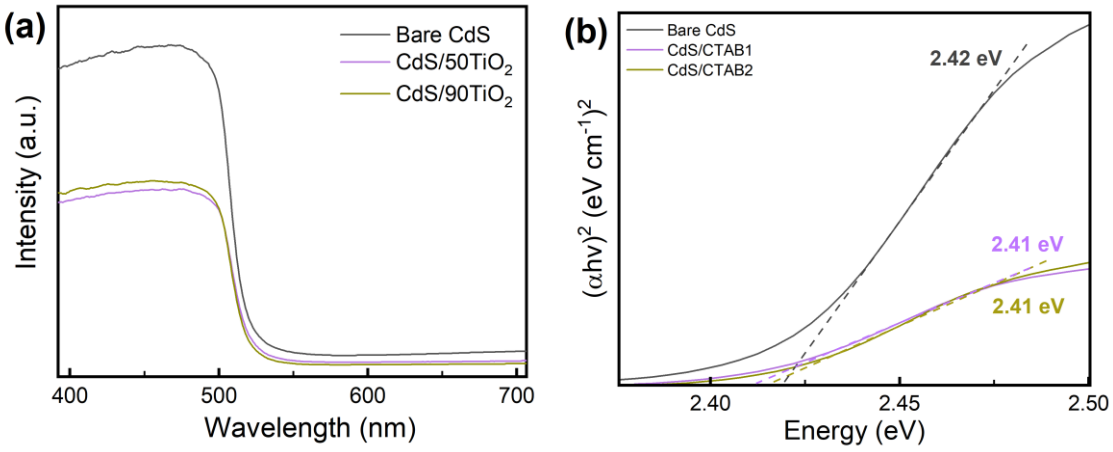

***Figure 4.5** (a) UV-Vis absorbance spectra and Tauc plots of bare CdS, CdS/50TiO₂, and CdS/90TiO₂.*

Raman spectroscopy has been used to investigate the in-depth structure of a $BiVO_4$ photoanode with Al_2O_3 passivation overlayer in another study. The results showed that

the ALD surface treatment and passivation have an effect on the V-O bond [139]. To find out if there is such change for CdS, Raman spectroscopy was conducted for all samples by using a 532 nm laser. In Figure 4B.2, the peaks located at 300.8, 601.5, and 908.9 cm^{-1} are attributed to first, second, and third order longitudinal optical (LO) modes, respectively [149]. TiO_2 coating does not cause any shift in Raman peaks, which means CdS chemical bond energy is not affected by the overlayer [150,151]. However, there is a significant drop in the peak intensities which corresponds to surface coverage but none of the samples show any characteristic peaks of TiO_2. Another outcome of Raman spectroscopy is the narrowing of 1LO and 2LO peaks after TiO_2 treatment. In the literature, narrowed Raman peak behavior is attributed to reduced lattice stress [152]. However, it is unlikely to expect such change after a mild surface treatment.

After the LSV and structural characterization experiments, the reason behind the negative effect of TiO_2 on CdS was further investigated by PEC characterization experiments. As a surface modification method, Liu et.al. used ALD TiO_2 overlayer on CdS as a fixation layer for surface defects, which prevents chemical corrosion, and acts as a hole blocking layer. The last one is very critical for this chapter because in this article, the main substrate is p-Si which is a photocathode and CdS is used to make a p/n heterojunction with strong light absorption characteristics [153]. It was constructed in a way that TiO_2 facilitates the extraction of electrons, rather than holes to have efficient HER on the surface. This can be related to the activity loss of CdS by TiO_2 overlayer at high thickness. Also, this behavior has been attributed to increased charge transfer resistance at photoanode/electrolyte interface due to overlayer deposition which EIS can be useful to explain [114,139]. We performed EIS spectroscopy to investigate how TiO_2 affects resistance and capacitive characteristics of CdS. In Figure 4.6a, Nyquist plots at 1 V, which are fitted by using the same Randles circuit presented in Chapter 3, are shown with the change in R_{CT} and C_{int} through the anodic potential sweep. All fittings and separate R_{CT} versus potential plots are given in Figure 4B.3 and B.4. Notice that in Figure 4.6a, the R_{CT} of CdS/50TiO_2 is the lowest which is unexpected because at 1 V, the photocurrent density of bare CdS is higher than CdS/50TiO_2 after the anodic jump. On the other side, the potential dependence of R_{CT} shows a switch around 0.8 V.

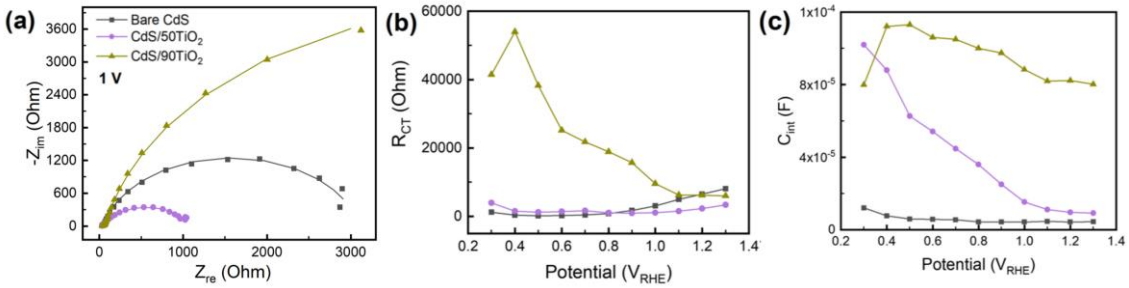

Figure 4.6 *(a) Nyquist plots recorded at 1V and (b) R_{CT} and (c) C_{int} versus potential plots of bare CdS, CdS/50TiO$_2$, and CdS/90TiO$_2$.*

Before 0.8 V, the R_{CT} of the bare CdS is lower than the TiO_2 treated samples, then it overcomes the R_{CT} of CdS/50TiO_2 at higher potentials. This can be caused by corrosion of TiO_2 layer and start of S^{-2} dissolution which was confirmed by the Ti 2p XPS plots of CdS/50TiO_2 sample before and after consecutive LSV scans. In Figure 4B.5, there is a drop in Ti 2p peak confirming the light-induced corrosion of TiO_2. The S 2p spectrum of CdS/50TiO_2 shows a drop as well, which means that the decreased Ti 2p peak is not related to blocking of TiO_2 layer by sulfide oxidation products, it is related to the photocorrosion of the sample. In addition to the dissolution of TiO_2, it might be also a result of CdS itself, dissolving to the electrolyte and carrying TiO_2 with it. Meanwhile, CdS/90TiO_2 has the highest resistance at all potentials due to the thick TiO_2 layer, and very close to bare CdS after 1.2 V. The important result in Figure 4B.4 is that the R_{CT} of bare CdS starts to increase after 0.6 V and increases by 20 times till 1.3 V. On the other side, CdS/50TiO_2 starts to show an R_{CT} increase after 0.9 V and it approximately triples at 1.3 V. Among all samples, CdS/90TiO_2 does not show any increase at all. This result is an indirect proof of our S^{2-} oxidation-related R_{CT} increase hypothesis in Chapter 3 since TiO_2 acts like a blocking layer which can suppress the light and chemical corrosion induced sulfide dissolution to the electrolyte. The change in interfacial capacitance (C_{int}) was analyzed in Figure 4.6c. Bare CdS shows almost a flat capacitive behavior compared to TiO_2 treated samples which show a decrease in C_{int} with increasing potential. The results also show that TiO_2 increases the C_{int} value of bare CdS at all potentials. The increased C_{int} can be attributed to accumulation of photogenerated charge carriers at TiO_2 overlayer instead of going to OER due to hole blocking effect. Another contributing factor to the capacitive built-up is the double layer capacitance at non-faradaic region [154] which is investigated by ECSA measurements. In Figure 4B.6, CV measurements at different scan rates are shown for all samples. The ECSA calculation was conducted by using the formula explained in the methodology section.

Results demonstrate that, ECSA of bare CdS is almost same as CdS/50TiO_2 but higher than that of CdS/90TiO_2. Therefore, TiO_2 overlayer does not have an increasing effect on double layer capacitance, surface hydrophilicity or it does not introduce an active site for OER.

TPC measurements with short light pulses were performed to understand the effect of TiO_2 on CdS charge carrier dynamics at different time scales. First of all, 1200 ms on 5 s off light pulse CA experiments at different potentials were performed, which is shown in Figure 4B.7. Firstly, all samples showed cathodic overshoot when light was off, which is associated with the activity loss caused by the recombination of remaining holes and the electrons. For bare CdS, CdS/50TiO_2, and CdS/90TiO_2 these cathodic overshoots continue till 0.6, 0.9, and 1.3 V, respectively. This result is consistent with the chopped illumination LSV experiment, where the photocurrent decay rate of bare CdS increases with TiO_2 overlayer. We compared the behavior of the samples at 0.4, 0.7, and 1 V as 3 different potential regions shown in Figure 4.7. CdS/90TiO_2 has the most intense cathodic overshoot at all potentials. The interesting outcome of this experiment is that, especially at low and moderate potentials, the activity loss with 90TiO_2 is not as much as in LSV measurements. Meaning that, in addition to increased charge transfer resistance at the photoanode/electrolyte interface, TiO_2 might have a positive effect on the passivation of surface states.

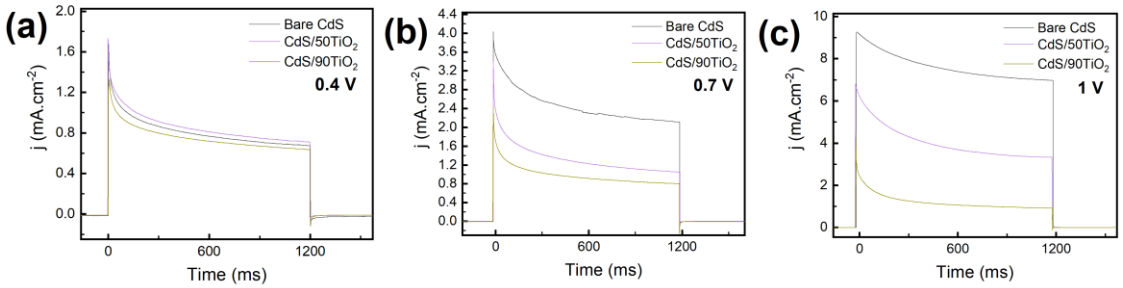

Figure 4.7 *1200 ms chopped light CA-TPC plots of bare CdS, CdS/50TiO_2, and CdS/90TiO_2 at (a) 0.4 V, (b) 0.7 V, and (c) 1 V.*

Notice that when light is on, CdS/50TiO_2 reaches the highest photocurrent density at 0.4 V followed by a subsequent decay. The decay rate of both CdS/50TiO_2 and CdS/90TiO_2 are higher than that of bare CdS which is consistent with the EIS results and capacitance measurements. However, the activity difference between CdS/90TiO_2 and bare CdS goes to a higher extent at high potentials, and it is smaller at low and moderate potentials.

Before deciding if TiO_2 can be a surface passivation layer for CdS, we performed 250 ms on 250 ms off LED light pulse TPC experiments to study the effect of TiO_2 more in detail. In Figure 4.8, comparison of the TPC behavior of all samples is shown. 0.7 V was chosen for this experiment because there are many processes happening at the same time such as OER, charge transport, possible charge trappings on the surface or S^{2-} oxidation. So, 0.7 V is ideal to investigate how TiO_2 affects these charge transfer and utilization mechanisms. Notice that, during 250 ms illumination, the photocurrent density of CdS/90TiO_2 and CdS/50TiO_2 are lower than that of bare CdS and their decay rates are higher as well. As can be seen from Figure 4.8a, CdS/90TiO_2 especially shows a significant decay after reaching a photocurrent density close to that of CdS/50TiO_2. Another important finding is that TiO_2 treated samples do not show the dip behavior as in bare CdS. We attributed this event to light-induced S^{2-} dissolution in section 3.3, Figure 3.5a. This result is in strong agreement with our EIS interpretation about the effect of TiO_2 on the R_{CT} increase caused by oxidation of S^{2-} on CdS surface.

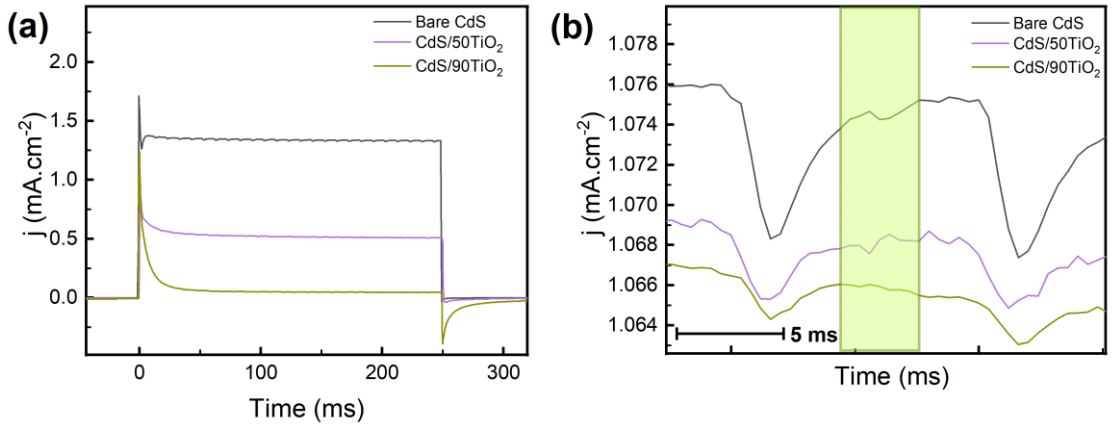

Figure 4.8 *(a) 250 ms on 250 ms off CA-TPC at 0.7 V and (b) stacked inset image of the wiggle behavior of bare CdS, CdS/50TiO_2, and CdS/90TiO_2.*

The wiggle behavior during steady state photocurrent was also investigated. In Figure 4.8b a stacked inset image of one wiggle is shown. This repeating pattern was used to propose possible activity loss tunnels where an electron trapping mechanism is involved. As mentioned, and explained in Section 3.3, there are 2 cathodic events contributing to electron trapping process. The drop in wiggle intensities and the disappearance of the cathodic event which is highlighted with green in Figure 4.8b indicate that that TiO_2 overlayer acts like a block on the surface that prevents electron trapping at surface sulfur vacancies and formation of vacancy sites on the surface for trapping. Another important parameter which might have caused this passivation effect

is the oxygen coming from OER which is also involved in the trapping/detrapping process. Since the high resistance of TiO_2 treated samples prevent hole injection to OER, it means there will be less oxygen to proceed the trapping process, which results in passivation of the cathodic events.

In addition to TPC experiments, we performed MS analysis to investigate the change in V_{fb} and N_d after TiO_2 deposition. MS plots of the samples are shown with their V_{fb} in Figure 4.9. There is a cathodic shift in V_{fb} after the TiO_2 treatment and $CdS/50TiO_2$ gives the lowest flat-band potential.

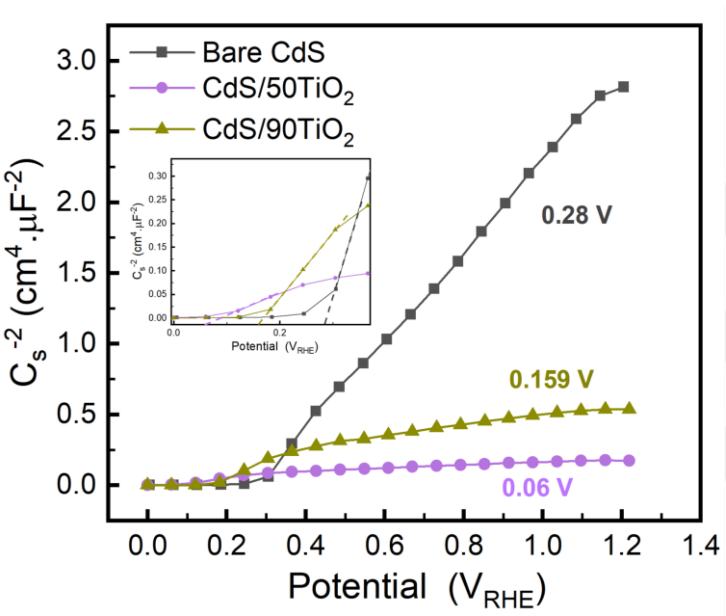

Figure 4.9 *Mott Schottky plots and of bare CdS, $CdS/50TiO_2$, and $CdS/90TiO_2$.*

N_d values of bare CdS, $CdS/50TiO_2$, and $CdS/90TiO_2$ were calculated as 2.8×10^{18}, 33.1×10^{18}, and 12.2×10^{18} cm^{-3}, respectively. It has been mentioned earlier in Chapter 3 that the cathodic shift in V_{fb} corresponds to enhanced charge separation in photoanodes. Notice that $CdS/90TiO_2$ shows an anodic shift after the significantly lowered V_{fb} of $CdS/50TiO_2$ due to the extra charge transfer resistance caused by thicker TiO_2. The same trend can be interpreted for N_d values where $CdS/50TiO_2$ has the highest N_d and there is a decrease in $CdS/90TiO_2$. Xi *et.al.* observed a similar trend in V_{fb} when they utilized a thin ZnO overlayer on Fe_2O_3 to reduce the recombination at surface defect sites[155]. They attributed this diminished V_{fb} to the lowered VB so that less bias is required to bring the bands to the flat position which corresponds to enhanced band bending. In this study, TiO_2 is used as a thin overlayer on the surface, so it can be said that it acts like a defect site on the surface rather than a pure TiO_2 layer to form a heterojunction structure. In fact, when TiO_2 is on top, it is a reversed type II

heterojunction, which means that it prevents utilization of holes in OER instead of facilitating upwards band bending. Even though ALD TiO_2 layer is not thick enough to form such heterostructure, the E_{VB} of TiO_2 being lower than that of CdS might cause a slight shift in the energy of holes in VB to decrease compared to bare CdS. At an optimum thickness, which was obtained with 50 ALD cycles, TiO_2 acts like a surface passivation layer, but thicker layer causes this shift in $E_{VB,}$ and it becomes more challenging to use holes at lower energy to drive OER. A similar scenario has been reported by Chen et.al. where they investigated the surface state passivation of $BiVO_4$ by TiO_2 overlayer and provided evidence for enhanced OER efficiency with deeper VB edge [156].

We also measured the transient OCP of the samples with solar simulator as the light source. In Figure 4.10, the transient behavior of OCP and the photovoltage change of the samples are given. The photovoltage values were calculated by the difference between dark OCP and steady state OCP upon illumination.

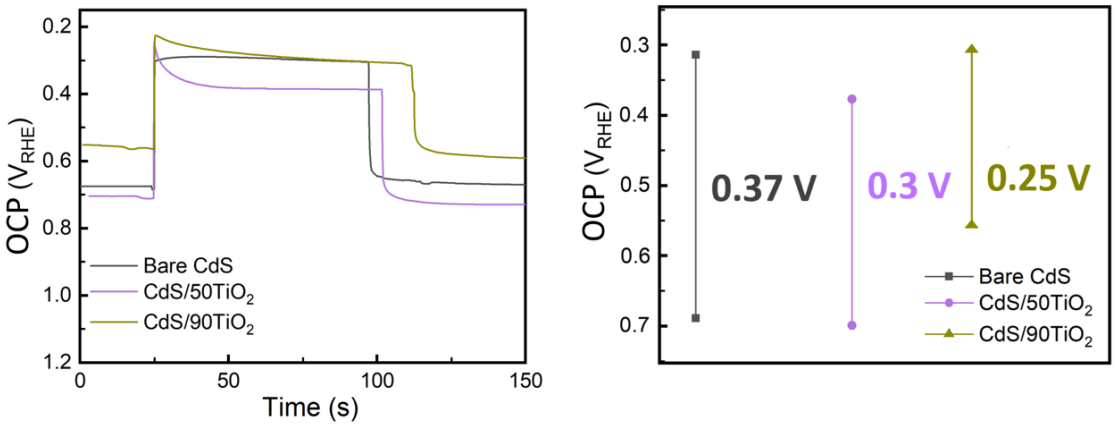

Figure 4.10 *(a) Chopped illumination OCP plots and (b) photovoltage change of bare CdS, CdS/50TiO₂, and CdS/90TiO₂.*

Figure 4.10a shows that dark OCP of $CdS/50TiO_2$ is slightly higher than that of bare CdS and $CdS/90TiO_2$ is the lowest one, which means $CdS/50TiO_2$ has the highest self-driven potential among all and it also reaches the highest photovoltage when the light is on, however, because of the higher R_{CT}, surface charge recombination takes place and its photovoltage at steady state is lower than that of bare CdS. This behavior is consistent with the activity measurements where $CdS/50TiO_2$ reaches the highest photocurrent density at anodic jumps. When the light is on, all photoanodes show a drop in OCP which is a characteristic of n-type semiconductors. Other than photovoltage, the steady state OCP behavior of CdS also changes after TiO_2 treatment. See that, bare CdS does not show any spike behavior while $CdS/50TiO_2$ and $CdS/90TiO_2$ show a cathodic

decay while reaching to steady state. The interesting result is that the spiking rate of CdS/50TiO_2 is higher than that of CdS/90TiO_2. However, CdS/90TiO_2 continues to decrease meanwhile the steady state OCP of CdS/50TiO_2 remains consistent upon illumination. This behavior can be caused by the high surface charge recombination of CdS/90TiO_2 due to high resistance at photoanode/electrolyte interface [157].

4.4 Conclusion

In this chapter, we showed the effect of TiO_2 overlayer on CdS by investigating the structural and PEC characteristics of CdS samples with different TiO_2 overlayer thicknesses. Results demonstrated that TiO_2 as a passivation overlayer is not as effective for CdS as it is for other photoanodes because of the high charge transfer resistance caused by TiO_2. However, the TPC measurements showed that TiO_2 can be tunable since it has positive contributions to the passivation of cathodic events that cause light-induced stability issues. We believe that this study can be critical since it reveals the negative sides of a very widely studied passivation overlayer, TiO_2, on CdS by detailed TPC and EIS measurements.

Chapter 5:

Photoelectrochemical H_2 Production from H_2S by Using CdS Photoanode with ALD TiO_2 Overlayer

5.1 Introduction

Solving the light-induced stability problem of CdS is extremely important to enhance its utilization among other semiconductor photoanode materials. There have been many efforts to modify CdS surface for water oxidation reaction which were discussed briefly in Section 3.1. and the introduction chapter. However, most of the reported studies showed that the research on CdS is more focused on increasing its PEC activity rather than fundamentals of its charge carrier dynamics. In chapter 3 and 4, we investigated the charge transfer and utilization mechanisms of CdS at photoanode/electrolyte interface by using TPC measurements at different time scales. Inspired by the findings of these studies and the fundamental mechanism behind the CdS photocorrosion, we hypothesized that CdS can be a very promising candidate for PEC H_2S splitting. In the literature, different materials were utilized for PEC and photocatalytic H_2S splitting but not as frequently as H_2O splitting due to the challenges and complexity of H_2S splitting which is explained in detail in Chapter 1. The reason why CdS is used for this reaction is, its stability in sulfide containing electrolytes has been reported before and its photocorrosion mechanism is strongly correlated to the extent of S^{2-} dissolution. In the literature CdS showed very promising stability in sulfide containing electrolytes, mostly Na_2SO_3/Na_2S, which means that its potential can be fully utilized in the presence of sulfides [158]. It is because of the low thermodynamic potential required for H_2S splitting which allows faster oxidation kinetics at photoanode/electrolyte interface.

Other than CdS, different semiconductor materials were utilized as photoanodes for H_2S splitting reaction. Bedoya *et.al.* reported that Sn doped Fe_2O_3 photoanodes give promising stability and PEC activity for alkaline H_2S splitting. They provided a detailed reaction mechanism for alkaline H_2S splitting with different polysulfide ions involved [159]. What makes alkaline conditions more challenging for H_2S splitting is that the dissolution and electrochemical oxidation of H_2S ions can interfere with each other, which makes quantification very difficult. In the literature, spectroscopic and electrochemical methods have been reported for the characterization of H_2S ions [160,161].

The oldest method is the methylene blue method were solutions with different H_2S concentrations were used to make a UV-Vis absorbance calibration curve. For acidic or neutral conditions, the quantification is mostly conducted through the sulfur since it is easier to measure than H_2. Luo *et.al.* used WO_3 photoanodes under acidic conditions and achieved selective oxidation of H_2S to elemental sulfur which was collected by centrifugation [162].

After investigating the challenges and the mechanisms behind the activity loss of CdS by TPC measurements and structural characterization experiments in the previous chapters, we utilized CdS for H_2S splitting and tested its activity and PEC characteristics for this reaction. Moreover, after seeing the poor improvement by TiO_2 overlayer, we tried it for H_2S splitting to see if it can be a useful passivation overlayer for a different reaction. We tested how H_2S affects the stability of CdS by PEC and structural characterization experiments.

5.2 Experimental

5.2.1 Fabrication of FTO/CdS Photoanodes

Fabrication of FTO/CdS Photoanodes

FTO/CdS photoanodes were synthesized by using the same hydrothermal deposition method described in section 3.2.2.

Fabrication of FTO/CdS/TiO_2 Photoanodes

ALD method was used to deposit ultrathin TiO_2 layer on CdS photoanode. Details of the method were described in section 4.2.

5.2.2 Photoelectrochemical Characterization

All PEC characterization experiments were conducted by the same 3 electrode configuration in a single quartz cell. H_2S experiments were done in H_2S feeded 0.1 M NaOH by controlling the H_2S flow with a mass flowmeter purchased from Alicat instruments.

5.3 Results & Discussion

As mentioned in section 5.1, the main reason behind choosing CdS for H_2S splitting is its stability in the presence of sulfide ions. Therefore, before the investigation of OER

kinetics, the stability of CdS for H_2O and H_2S splitting was tested by CA measurements and different structural characterization methods. To test the stability, H_2S feeding to 0.1 M NaOH electrolyte was performed at 10 sscm rate. The feeding was stopped after 30 min when the electrolyte pH reached 12.31. The first reason to stay in this pH was to have comparable results with alkaline H_2O splitting. Moreover, variety of H_2S ions change towards moderate pH values and it brings the possible crossover of many different reactions. Between pH 10 and 12, the majority sulfide ion species is HS^- and there is a minority of S^{2-} [163]. In order to assign the HS^- concentration, an electrochemical characterization method was used inspired by the paper of Ghayad et.al [164]. Solutions of different Na_2S concentrations dissolved in 0.1M NaOH were prepared to produce HS^- ions through the reaction below.

$$Na_2S + 2H_2O \rightleftharpoons 2Na^+ + 2OH^- + H_2S$$

$$H_2S \rightleftharpoons H^+ + HS^-$$

Considering the 1:1 stoichiometric ratio of Na_2S and HS^-, the concentration of dissolved Na_2S was taken as the HS^- concentration. The solutions were tested by CV with a 3-electrode configuration of Pt, Pt, and Ag/AgCl. The results are presented in Figure 5C.1 with the CV measured in 30 min H_2S feeded 0.1M NaOH. There is a gradual increase in the peak located at 0.94 V which can be attributed to electrochemical oxidation of HS^- ions. In the cathodic sweeps, the gradual decrease of the peak located at 0.64 V indicates an oxidative process which is disappearing as the pH decreases. It is important to note that unlike H_2S, Na_2S is strongly alkaline due to dissolution of OH- ions, so H_2S feeded electrolyte has the lowest pH among all. Since the intensity of the cathodic peaks is negligible compared to anodic events, it can be said that the majority ion is HS^-. In Figure 5C.1b, the calibration curve which was obtained by the anodic current at 0.94 V and the corresponding Na_2S concentration is given. The concentration of HS^- ions in the H_2S/NaOH was calculated as 0.05 M from the linear fit equation.

The first experiment performed in 0.1M NaOH/ H_2S electrolyte was CA at 0.8 V which is shown in Figure 5.1. The experiment was performed with bare CdS with and without H_2S feeding. The results show that in the first 30 min of CA, photocurrent density of CdS drops by 94 and 20% in 0.1M NaOH and 0.1M NaOH/ H_2S, respectively. It can be also seen from the color difference that CdS undergoes more corrosion in the absence of H_2S which is shown in Figure 5.1b. This result was supported by structural

characterization data. In the characterization data, the samples which were tested in the absence and presence of H_2S are labeled as after H_2O and after H_2S, respectively.

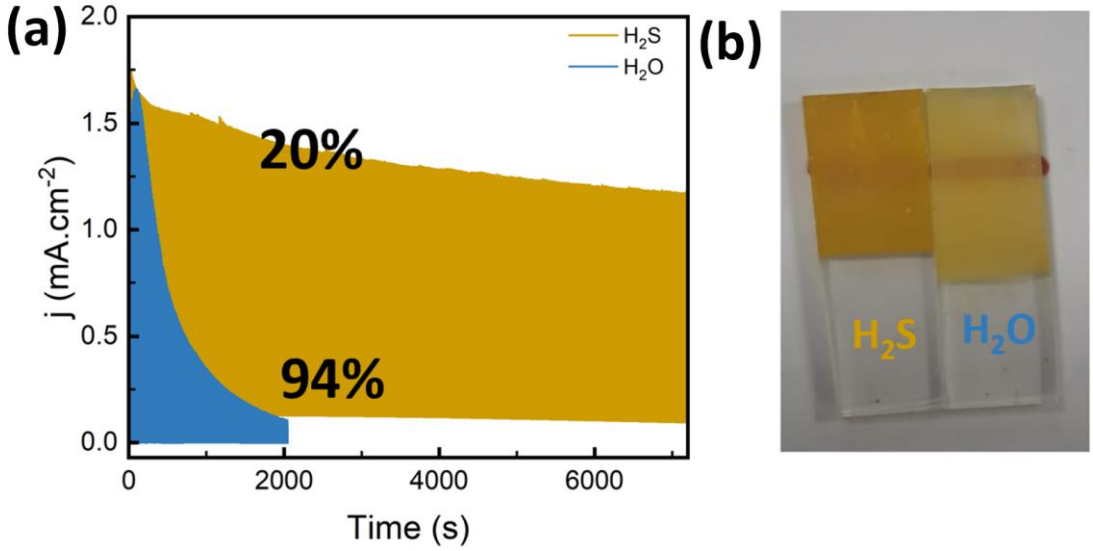

Figure 5.1 *(a) CA of bare CdS in 0.1M NaOH (H_2O) and 0.1M NaOH feeded with H_2S for 30 min (H_2S), (b) pictures of the CdS samples after CA with and without H_2S.*

In Figure 5C.2 and 3, SEM images and XRD spectra of fresh CdS, CdS after CA in 0.1M NaOH and H_2S/0.1M NaOH are presented. The morphology of CdS was significantly disturbed after CA experiment in 0.1 M NaOH due to photocorrosion and surface oxidation. Meanwhile CdS tested in 0.1M NaOH/ H_2S was almost unchanged. It is confirmed by XRD analysis where some of the characteristic peaks of hexagonal wurtzite structure are gone after CA. Moreover, some new peaks formed, which are shown by the green highlighted areas. These peaks which are located at 29.6, 35.3, and 49.3 degrees are attributed to CdO and FTO, which can be a sign for activity loss caused by surface oxidation and thinning after PEC [165,166]. Overall, it can be said that H_2S has a recovery effect on both surface oxidation and dissolution. Wang *et.al.* used WO_3/Bi_2O_3 heterojunction for dual mode PEC H_2S sensing, and they reported Bi_2S_3 formation by ion exchange reaction between S^{2-} and Bi_2O_3, which might be the case for CdS as well [167]. We also studied changes in the optical properties and surface structure. In Figure 5C.3a, the UV results show that there is a shift towards lower wavelength at the absorption edge after H_2O, which is not desirable, meanwhile the absorption characteristics did not show any change after H_2S. Such behavior has been attributed to photobleaching effect before [168]. On the other side, the intensity of raman peaks almost vanished after H_2O. Although there is also a drop after H_2S, the peak widths and peak to peak ratios do not show any significant change, meaning that H_2S prevents any

disturbance in the chemical bonding of CdS. On the other side, the red shift and peak broadening after H_2O shows disturbance in the lattice due to photocorrosion. This trend has been attributed to surface oxidation induced lattice expansion [169].

In addition to structural, and optical characterization, we performed XPS analysis to see how the surface structure is affected by H_2S feeding to the electrolyte. For this measurement, a CdS sample used in 5 consecutive LSV measurements was used instead of a sample used in CA. The reason is that the photocorrosion effect of CA is very strong, which makes it difficult to detect and compare the Cd and S peaks. Figure 5.2a and b show that the photocorrosion-induced dissolution of CdS is more from the S^{2-} side rather than Cd^{2+}. Moreover, the shift towards lower binding energies in Cd 3d, S 2p, and O 1s confirms the reaction of CdS with photogenerated holes and as a result, surface oxidation which causes O 1s peak intensity to increase.

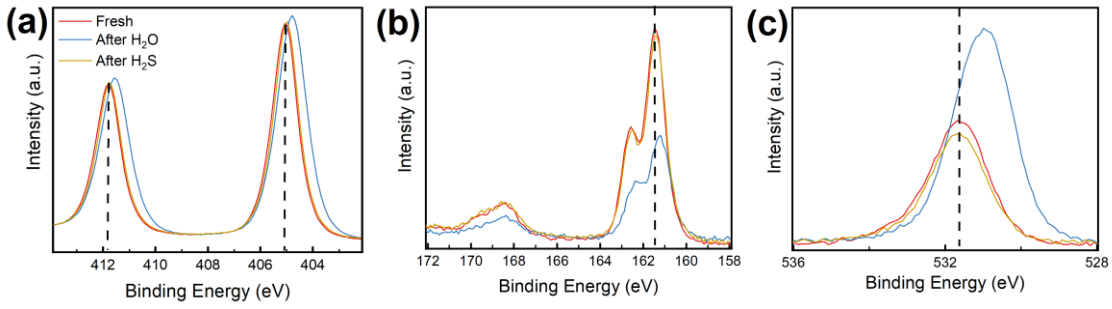

Figure 5.2 *(a) Cd 3d, (b) S 2p, and (c) O 1s spectra of fresh CdS and CdS after CA experiment at 0.8 V in 0.1M NaOH and 0.1M NaOH/H_2S electrolytes.*

After confirming the the significant stability improvement of CdS in 0.1M NaOH/ H_2S, the PEC activity of the CdS was measured by continuous and chopped light LSV measurements. Furthermore, CdS samples with different thicknesses of TiO_2 overlayers were tested since the ultrathin TiO_2 did not show a significant improvement for the water oxidation kinetics of CdS, especially with high thickness due to increased R_{CT}. However, the potential barrier for H_2S splitting is lower than that of H_2O splitting so, TiO_2 can in fact work as a surface passivation layer on CdS for H_2S splitting and improve the activity. 3 samples with 15, 25, and 50 cycles of ALD TiO_2 coating were prepared. The activity increase after surface TiO_2 decoration was promising. In Figure 5.3, LSV results under continuous and chopped illumination are shown. In Figure 5.3a, it is shown that the onset potential of bare CdS shifts more than 0.4V to the cathodic direction and gives 1.7 times higher photocurrent density at 1.2 V in the presence of H_2S. However, the activity decrease at higher thickness TiO_2 overlayer trend is still

valid here which is shown in Figure 5.3b where the activity of bare CdS reaches a maximum at 25TiO_2 and decreases with 50TiO_2.

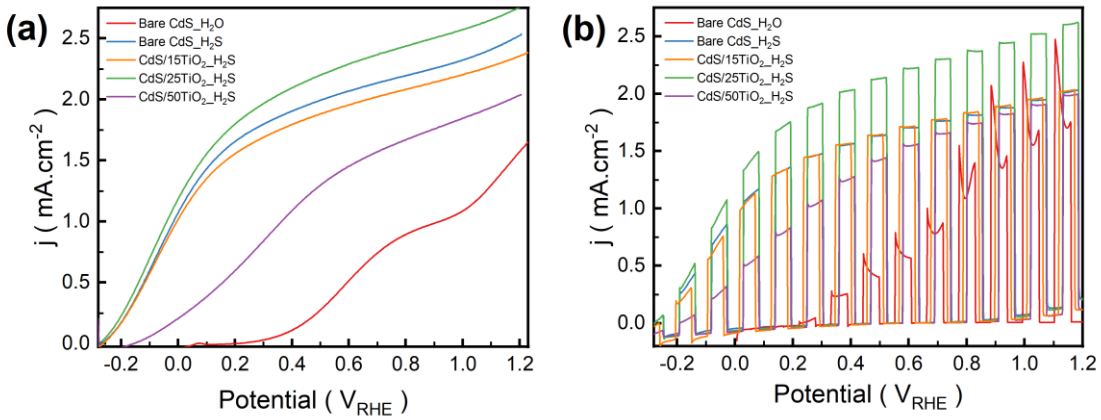

Figure 5.3 *(a) Continuous illumination and (b) chopped light illumination LSV of bare CdS in 0.1M NaOH and 0.1M NaOH/ H_2S electrolytes and 15-25-50 cycles TiO_2 coated CdS in 0.1M NaOH/H_2S.*

This improvement is related to fast oxidation kinetics which is shown by the TPC behavior in Figure 5.3b. Compared to H_2O splitting, CdS did not give any photocurrent decay after the anodic jumps when the light was on, which is a typical behavior of photoanodes in electrolytes with hole scavenger [48]. Moreover, the cathodic overshoot when the light was off completely disappeared in H_2S feeded electrolyte, which is a good sign for the suppressed photocorrosion and surface charge recombination. As mentioned earlier, H_2S splitting is a thermodynamically less hindered process. In Figure 5.3b, the higher dark photocurrent density of bare CdS and CdS/25TiO_2 in 0.1M NaOH/H_2S between 1 and 1.2 V is a result of electrochemical oxidation of H_2S ions. Notice that dark photocurrent of CdS/50TiO_2 is the lowest in this potential window, which means that TiO_2 does not contribute to the activity as a co-catalyst.

Since the structural and optical properties of ALD TiO_2 coated CdS were investigated and explained in Chapter 4, rest of this chapter will be more focused on understanding the reason behind the activity increase through PEC characterization experiments by using the findings from Chapter 4. First, ECSA measurement was performed to investigate the effect of TiO_2 on double layer capacitance and how H_2S affects bare CdS itself. The important part for this experiment is that ECSA measurement via CV scans at different scan rates should be performed in the non-faradaic region, which means between 2 potentials where there is no significant current. Due to the difference in required overpotential for H_2O and H_2S splitting reactions, the potential window was shifted towards the cathodic direction for 0.1M NaOH/H_2S electrolyte to have a reasonable comparison of double layer capacitance with and without H_2S. The CV scans

of 0.1M NaOH/H_2S measurements are shown in Figure 5C.5. ECSA plots of all samples are presented in Figure 5.4 where TiO_2 shows an increase in the double layer capacitance, which is different from the results obtained in Chapter 4.

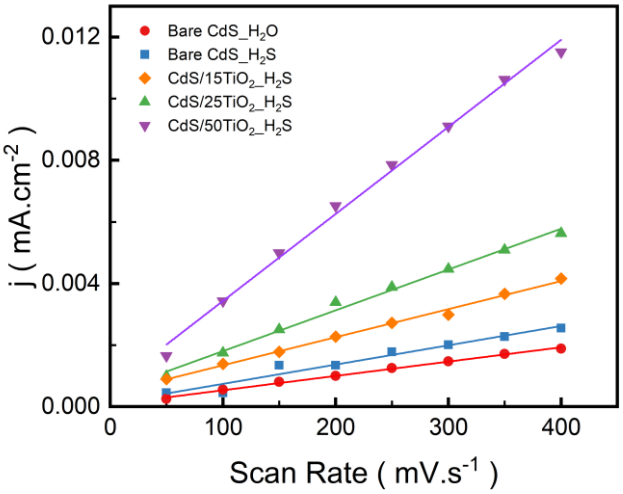

Figure 5.4 *ECSA plots of bare CdS in 0.1M NaOH and H_2S/0.1M NaOH electrolytes and 15-25-50 cycles TiO_2 coated CdS in 0.1M NaOH/H_2S.*

Firstly, ECSA of bare CdS is higher in 0.1M NaOH/H_2S. It can be resulted from the high affinity of the surface to HS^-/S^{2-} since the photoanode itself is also a sulfide [170]. ECSA of CdS increases even more with higher TiO_2 overlayer thickness. Since TiO_2 gave the exact opposite effect in 0.1M NaOH, the reason behind this change must be a result of TiO_2 introducing active sites for HS^-/S^{2-} ions, which results in enhanced oxidation kinetics. EIS analysis was conducted to see how increased ECSA affected the overall capacitive behavior of the samples through the LSV potential range. In Figure 5.5, the change in R_{CT} and C_{int} of the samples are given. For the 0.1M NaOH/H_2S electrolyte, the measurements were performed starting from a lower potential to not miss the onset potential for H_2S splitting. The Nyquist fittings were done by using Randles circuit and presented in Figure 5C. 6. Before discussing the effect of TiO_2, see the trend for bare CdS in 0.1M NaOH and 0.1M NaOH/H_2S. At 0.2 and 0.3 V, the R_{CT} of bare CdS is higher without H_2S because 0.2 is already higher than the onset potential. However, it is not even kinetic overpotential for H_2O splitting so, the extent of charge separation is higher in 0.1M NaOH/H_2S at this potential interval. However, between 0.4 and 0.8 V, the R_{CT} of bare CdS is higher in 0.1M NaOH/H_2S. Considering the high affinity of photoanode surface to HS^-/S^{2-} this behavior is due to fast sulfide oxidation at the photoanode/electrolyte interface and consistent with our S^{2-} oxidation related R_{CT} increase hypothesis in Chapter 3. This trend was reversed after 0.9V where R_{CT} in 0.1

M NaOH became dominant again. The reason is that R_{CT} for hole transfer increases when the charge separation is poor and the photogenerated holes cannot be injected to the electrolyte. Because of the difference in the required overpotential, the region between 1 and 1.2 V can be considered as high overpotentials providing boosted band bending and charge separation for H_2S splitting, which results in decreasing R_{CT}.

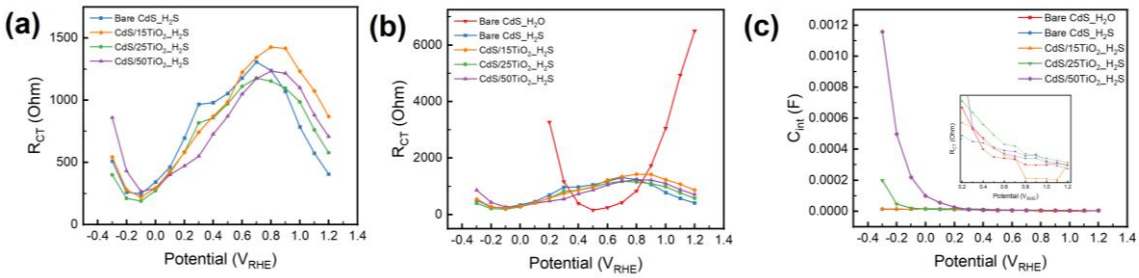

Figure 5.5 *R_{CT} versus potential plots of only (a) bare CdS and 15-25-50 cycles TiO_2 coated CdS in 0.1M NaOH/H_2S and (b) comparison of these plots with that of bare CdS in 0.1M NaOH. (c)Interfacial capacitance versus potential plots of bare CdS in 0.1M NaOH and 0.1M NaOH/ H_2S electrolytes and 15-25-50 cycles TiO_2 coated CdS in 0.1M NaOH/H_2S.*

In 0.1M NaOH/H_2S sample set, R_{CT} of 50TiO_2 has the highest potential at low potentials which might be resulted from the contribution of double layer capacitance from the non-faradaic region. At moderate potentials, the positive effect of TiO_2 becomes more dominant where R_{CT} of bare CdS is decreased with TiO_2 treatment. On the other side, the trend in C_{int} is in strong agreement with ECSA and R_{CT} measurements since the capacitive behavior of bare CdS increases with thicker TiO_2 overlayer. The C_{int} of the samples decrease with higher applied bias due to enhanced charge separation and they become almost flat, which indicates successful hole utilization.

Transient photovoltage behavior of the samples was also investigated by chopped light illumination OCP measurement in Figure 5.6. The dark OCP of the bare CdS showed a slight decrease in the presence of H_2S and the 0.1M NaOH/H_2S sample set showed a trend where the dark OCP decreases as the TiO_2 overlayer becomes thicker. The similar trend with TiO_2 surface modification was discussed in the previous chapter. However, considering the photovoltage change when the samples are illuminated, it is shown that the self-driven potential of the system can be utilized more efficiently in the presence of H_2S.

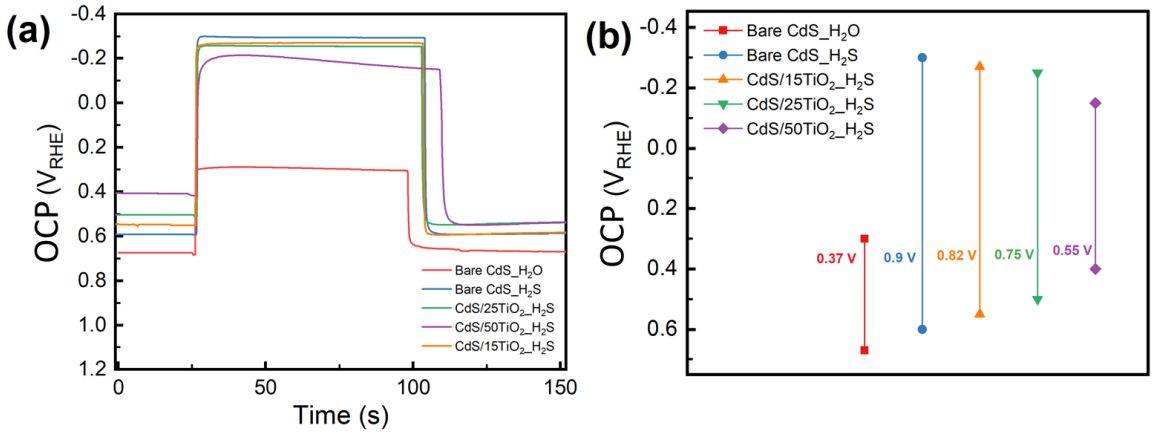

Figure 5.6 *(a) Chopped illumination OCP plots and (b) photovoltage change bare CdS in 0.1M NaOH and H_2S/0.1M NaOH electrolytes and 15-25-50 cycles TiO_2 coated CdS in 0.1M NaOH/H_2S.*

When the light is on, the photovoltage difference in the presence of H_2S is more than 2 times higher than that of H_2O splitting. The photovoltage change is decreasing with higher TiO_2 thickness in 0.1M NaOH/H_2S as shown in Figure 5.6b. The decrease in photovoltage with TiO_2 overlayer was also observed in Chapter 4 and attributed to increased R_{CT}. It is also consistent with the decay in steady state photovoltage of CdS/50TiO_2. It is important to note that photovoltage drop after TiO_2 deposition can be considered as a negative contribution to the PEC activity, considering the fast kinetics of H_2S splitting, but it does not have a significant effect on the activity of CdS with an optimum TiO_2 overlayer thickness in 0.1M NaOH/H_2S electrolyte, which was obtained by 25 cycles of ALD deposition.

Lastly, MS analysis was performed and presented in Figure 5.7 to see the change V_{fb} and N_d in 0.1M NaOH/H_2S. The V_{fb} of bare CdS shifted almost 0.4 V towards the cathodic direction in the presence of H_2S proving the enhanced band bending in H_2S splitting. Moreover, among 0.1M NaOH/H_2S samples, CdS/25TiO_2 gave the lowest V_{fb} which is consistent with the PEC activity results.

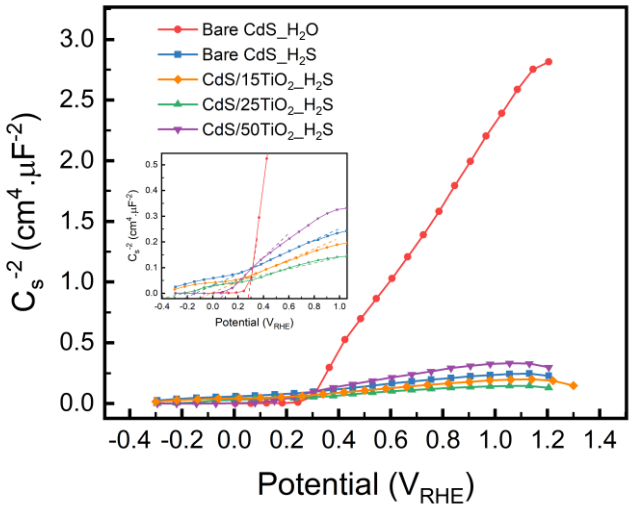

Figure 5.7 *MS plots of bare CdS in 0.1M NaOH and H_2S/0.1M NaOH electrolytes and 15-25-50 cycles TiO_2 coated CdS in 0.1M NaOH/H_2S.*

Furthermore, N_d of bare CdS showed a significant increase with H_2S. It has been reported that higher S^{2-} concentration in the electrolyte can cause an increase in N_d of semiconductor photoanodes [171]. Among TiO_2 treated samples, CdS/25TiO_2 and CdS/5OTiO_2 have the highest and lowest N_ds, respectively. A similar trend was observed with CdS/50TiO_2 and CdS/90TiO_2 for H_2O splitting, which shows that high R_{CT} due to thick TiO_2 overlayer can cause N_d drop in H_2S splitting too.

5.4 Conclusion

In this chapter, we utilized CdS photoanodes for PEC H_2S splitting reaction under alkaline conditions. Within the light of the findings from Chapter 3 and 4, CdS was chosen to be a promising candidate for H_2S splitting to enhance its stability by providing a surface recovery effect. The activity and stability measurement results were promising and in accordance with the findings from the other chapters. After confirming the stability and higher activity of CdS for H_2S splitting by various structural characterization methods, we utilized ultrathin ALD TiO_2 overlayer on CdS for H_2S splitting to see if it can improve the activity with less surface charge recombination in a thermodynamically less hindered process. Results were more promising in the presence of H_2S which was proven by extensive PEC characterization experiments.

Chapter 6:**Summary and Future Work**

Overall purpose of this study was to understand the reasons behind the activity loss of CdS photoanodes by monitoring the effect of different parameters, such as potential and light intensity, on the TPC behavior and provide mild surface treatment methods to improve the activity for PEC H_2O and H_2S splitting. To provide a fundamental understanding and propose activity loss mechanisms, various structural and PEC characterization methods were extensively utilized.

PEC water oxidation activity and structural properties of bare CdS were studied in detail to provide a strong background for the charge carrier utilization. TPC measurements were analyzed to give a mechanism for electron trapping on CdS, which was much less studied in the literature compared to metal oxide photoanodes. Results showed that surface sulfur vacancies were very critical in surface charge recombination due to electron trapping. After that, CTAB was used to enhance the charge transfer properties of CdS by passivation of surface trap sites. Although the increase in the photocurrent density with CTAB treatment is significant, it did not provide a solution for the long-term stability. Hence, it can be further improved by another surface modification method, such as utilization of another semiconductor material to make heterojunction with CdS. In this way, electron trapping passivation by CTAB can be even more promising with enhanced band-bending of heterojunction structure. Moreover, a surface protecting layer which is resistant to light-induced and chemical corrosion to suppress dissolution of CdS to the electrolyte.

Ultrathin TiO_2 overlayers with different thicknesses were grown on CdS by ALD and tested for PEC activity to see if it can prevent electron trapping and enhance OER kinetics at photoanode/electrolyte interface. The improvement with TiO_2 overlayer was not as significant as in Chapter 3 after CTAB treatment. However, light pulse CA TPC measurements showed that TiO_2 overlayer can passivate surface charge trapping at an optimum thickness. The reason why the improvement was mild was the extra charge transfer resistance at photoanode/electrolyte interface caused by TiO_2 overlayer. A solution to that problem might be the utilization of TiO_2 on a thinner CdS layer to reduce R_{CT}. In this way, the photocurrent density may drop but overall stability in the long run might be improved. Since the critical process to prevent photocorrosion of CdS is the

utilization of holes, modification of the surface with OER co-catalysts can also be effective to improve the PEC performance of CdS.

CdS was tested for H_2S splitting which turned out to be a very promising reaction for PEC H_2 production where CdS can reach higher activities and improved stability for long term applications. Results showed that H_2S splitting can provide a recovery effect for the activity loss of CdS caused by surface charge recombination and light-induced corrosion, which was proven by different spectroscopy and imaging techniques to compare the change in the sample in the presence and absence of dissolved H_2S. To further improve the activity of CdS for H_2S splitting reaction, ALD TiO_2 layer was utilized and after the findings of Chapter 4, the results for H_2S were surprising and promising. After the analysis of fundamental PEC characterization, it was concluded that ultrathin TiO_2 can provide active sites on the surface to facilitate the oxidation kinetics by increasing ECSA. Since the stability of CdS in the presence of dissolve H_2S is already promising, methods for increasing the oxidation kinetics such as co-catalyst loading, or heterojunction engineering can be utilized to achieve significantly high efficiencies. Moreover, construction of a tandem cell by using CdS as the photoanode and a photovoltaic device to drive the reaction is an appealing approach since the thermodynamic potential required for H_2S splitting is less than that of H_2O. Other than modifying the CdS itself, the design of special PEC cells is critical for the efficiency and quantitative analysis of H_2S splitting reaction. Utilization of different H-cell configurations can be an important advancement to have selective and precise reactions for industrial applications.

All in all, this work can be an important insight and contribution for the utilization of CdS in PEC hydrogen production applications by also providing simple surface modification methods which can be used for other semiconductor photoanodes as well.

References

(1) Li, S.; Kang, Q.; Baeyens, J.; Zhang, H. L.; Deng, Y. M. Hydrogen Production: State of Technology. *IOP Conf. Ser.: Earth Environ. Sci.* **2020**, *544* (1), 012011. https://doi.org/10.1088/1755-1315/544/1/012011.

(2) Sivula, K.; van de Krol, R. Semiconducting Materials for Photoelectrochemical Energy Conversion. *Nat Rev Mater* **2016**, *1* (2), 1–16. https://doi.org/10.1038/natrevmats.2015.10.

(3) Hisatomi, T.; Kubota, J.; Domen, K. Recent Advances in Semiconductors for Photocatalytic and Photoelectrochemical Water Splitting. *Chem. Soc. Rev.* **2014**, *43* (22), 7520–7535. https://doi.org/10.1039/C3CS60378D.

(4) Fujishima, A.; Honda, K. Electrochemical Photolysis of Water at a Semiconductor Electrode. *Nature* **1972**, *238* (5358), 37–38. https://doi.org/10.1038/238037a0.

(5) Fernández-Climent, R.; Giménez, S.; García-Tecedor, M. The Role of Oxygen Vacancies in Water Splitting Photoanodes. *Sustainable Energy & Fuels* **2020**, *4* (12), 5916–5926. https://doi.org/10.1039/D0SE01305F.

(6) Kahn, A. Fermi Level, Work Function and Vacuum Level. *Materials Horizons* **2016**, *3* (1), 7–10. https://doi.org/10.1039/C5MH00160A.

(7) Ling Tan, H.; F. Abdi, F.; Hau Ng, Y. Heterogeneous Photocatalysts: An Overview of Classic and Modern Approaches for Optical, Electronic, and Charge Dynamics Evaluation. *Chemical Society Reviews* **2019**, *48* (5), 1255–1271. https://doi.org/10.1039/C8CS00882E.

(8) Xiang, C.; Papadantonakis, K. M.; Lewis, N. S. Principles and Implementations of Electrolysis Systems for Water Splitting. *Mater. Horiz.* **2016**, *3* (3), 169–173. https://doi.org/10.1039/C6MH00016A.

(9) Jiang, C.; A. Moniz, S. J.; Wang, A.; Zhang, T.; Tang, J. Photoelectrochemical Devices for Solar Water Splitting – Materials and Challenges. *Chemical Society Reviews* **2017**, *46* (15), 4645–4660. https://doi.org/10.1039/C6CS00306K.

(10) Pan, H.; Zhu, S.; Lou, X.; Mao, L.; Lin, J.; Tian, F.; Zhang, D. Graphene-Based Photocatalysts for Oxygen Evolution from Water. *RSC Adv.* **2015**, *5* (9), 6543–6552. https://doi.org/10.1039/C4RA09546D.

(11) Murphy, A. B.; Barnes, P. R. F.; Randeniya, L. K.; Plumb, I. C.; Grey, I. E.; Horne, M. D.; Glasscock, J. A. Efficiency of Solar Water Splitting Using Semiconductor Electrodes. *International Journal of Hydrogen Energy* **2006**, *31* (14), 1999–2017. https://doi.org/10.1016/j.ijhydene.2006.01.014.

(12) Eichler, H. J.; Hermerschmidt, A. Light-Induced Dynamic Gratings and Photorefraction. In *Photorefractive Materials and Their Applications 1: Basic Effects*; Günter, P., Huignard, J.-P., Eds.; Springer Series in Optical Sciences; Springer: New York, NY, 2006; pp 7–42. https://doi.org/10.1007/0-387-25192-8_2.

(13) Peng, X.; Wei, Q.; Copple, A. Strain-Engineered Direct-Indirect Band Gap Transition and Its Mechanism in Two-Dimensional Phosphorene. *Phys. Rev. B* **2014**, *90* (8), 085402. https://doi.org/10.1103/PhysRevB.90.085402.

(14) Corby, S.; Rao, R. R.; Steier, L.; Durrant, J. R. The Kinetics of Metal Oxide Photoanodes from Charge Generation to Catalysis. *Nat Rev Mater* **2021**, *6* (12), 1136–1155. https://doi.org/10.1038/s41578-021-00343-7.

(15) Pudi, A.; Rezaei, M.; Signorini, V.; Andersson, M. P.; Baschetti, M. G.; Mansouri, S. S. Hydrogen Sulfide Capture and Removal Technologies: A Comprehensive Review of Recent Developments and Emerging Trends. *Separation and*

Purification Technology **2022**, *298*, 121448. https://doi.org/10.1016/j.seppur.2022.121448.
(16) Dan, M.; Yu, S.; Li, Y.; Wei, S.; Xiang, J.; Zhou, Y. Hydrogen Sulfide Conversion: How to Capture Hydrogen and Sulfur by Photocatalysis. *Journal of Photochemistry and Photobiology C: Photochemistry Reviews* **2020**, *42*, 100339. https://doi.org/10.1016/j.jphotochemrev.2019.100339.
(17) Zaman, J.; Chakma, A. Production of Hydrogen and Sulfur from Hydrogen Sulfide. *Fuel Processing Technology* **1995**, *41* (2), 159–198. https://doi.org/10.1016/0378-3820(94)00085-8.
(18) Raj, A.; Thiraviam, P.; Elkadi, M. A Reaction Kinetics Study on Benzene Oxidation in the Claus Process by Sulfur Monoxide. *J. Phys. Chem. A* **2023**, *127* (4), 1013–1025. https://doi.org/10.1021/acs.jpca.2c06586.
(19) van Nisselrooya, P. F. M. T.; Lagasb, J. A. Superclaus Reduces SO2, Emission by the Use of a New Selective Oxidation Catalyst. *Catalysis Today* **1993**, *16* (2), 263–271. https://doi.org/10.1016/0920-5861(93)85023-S.
(20) Dan, M.; Xiang, J.; Wu, F.; Yu, S.; Cai, Q.; Ye, L.; Ye, Y.; Zhou, Y. Rich Active-Edge-Site MoS2 Anchored on Reduction Sites in Metal Sulfide Heterostructure: Toward Robust Visible Light Photocatalytic Hydrogen Sulphide Splitting. *Applied Catalysis B: Environmental* **2019**, *256*, 117870. https://doi.org/10.1016/j.apcatb.2019.117870.
(21) Bedoya-Lora, F.; Hankin, A.; Kelsall, G. H. Photo-Electrochemical Hydrogen Sulfide Splitting Using Sn IV -Doped Hematite Photo-Anodes. *Electrochemistry Communications* **2016**, *68*, 19–22. https://doi.org/10.1016/j.elecom.2016.04.010.
(22) Zong, X.; Han, J.; Seger, B.; Chen, H.; Lu, G. (Max); Li, C.; Wang, L. An Integrated Photoelectrochemical–Chemical Loop for Solar-Driven Overall Splitting of Hydrogen Sulfide. *Angewandte Chemie* **2014**, *126* (17), 4488–4492. https://doi.org/10.1002/ange.201400571.
(23) Ma, W.; Han, J.; Yu, W.; Yang, D.; Wang, H.; Zong, X.; Li, C. Integrating Perovskite Photovoltaics and Noble-Metal-Free Catalysts toward Efficient Solar Energy Conversion and H_2S Splitting. *ACS Catal.* **2016**, *6* (9), 6198–6206. https://doi.org/10.1021/acscatal.6b01772.
(24) Nan, W.; Niu, Y.; Qin, H.; Cui, F.; Yang, Y.; Lai, R.; Lin, W.; Peng, X. Crystal Structure Control of Zinc-Blende CdSe/CdS Core/Shell Nanocrystals: Synthesis and Structure-Dependent Optical Properties. *J. Am. Chem. Soc.* **2012**, *134* (48), 19685–19693. https://doi.org/10.1021/ja306651x.
(25) Bao, N.; Shen, L.; Takata, T.; Domen, K.; Gupta, A.; Yanagisawa, K.; Grimes, C. A. Facile Cd−Thiourea Complex Thermolysis Synthesis of Phase-Controlled CdS Nanocrystals for Photocatalytic Hydrogen Production under Visible Light. *J. Phys. Chem. C* **2007**, *111* (47), 17527–17534. https://doi.org/10.1021/jp076566s.
(26) Nishino, J.; Chatani, S.; Uotani, Y.; Nosaka, Y. Electrodeposition Method for Controlled Formation of CdS Films from Aqueous Solutions. *Journal of Electroanalytical Chemistry* **1999**, *473* (1), 217–222. https://doi.org/10.1016/S0022-0728(99)00250-8.
(27) Liu, F.; Lai, Y.; Liu, J.; Wang, B.; Kuang, S.; Zhang, Z.; Li, J.; Liu, Y. Characterization of Chemical Bath Deposited CdS Thin Films at Different Deposition Temperature. *Journal of Alloys and Compounds* **2010**, *493* (1), 305–308. https://doi.org/10.1016/j.jallcom.2009.12.088.
(28) Moualkia, H.; Hariech, S.; Aida, M. S. Structural and Optical Properties of CdS Thin Films Grown by Chemical Bath Deposition. *Thin Solid Films* **2009**, *518* (4), 1259–1262. https://doi.org/10.1016/j.tsf.2009.04.067.

(29) Seon, J.-B.; Lee, S.; Kim, J. M.; Jeong, H.-D. Spin-Coated CdS Thin Films for n-Channel Thin Film Transistors. *Chem. Mater.* **2009**, *21* (4), 604–611. https://doi.org/10.1021/cm801557q.
(30) Liu, B.; Wang, D.; Wang, L.; Sun, Y.; Lin, Y.; Zhang, X.; Xie, T. Glutathione-Assisted Hydrothermal Synthesis of CdS-Decorated TiO2 Nanorod Arrays for Quantum Dot-Sensitized Solar Cells. *Electrochimica Acta* **2013**, *113*, 661–667. https://doi.org/10.1016/j.electacta.2013.09.143.
(31) Sang, P.; Kim, J. H. Hydrothermal Synthesis of the CdS Nanorods on Electrochemically Deposited Fe2O3 Thin Film for Improving Photoelectrochemical Performance. *Journal of Environmental Chemical Engineering* **2023**, *11* (3), 110197. https://doi.org/10.1016/j.jece.2023.110197.
(32) Wang, Z.; Nguyen, T. D.; Yeo, L. P.; Tan, C. K.; Gan, L.; Tok, A. I. Y. Periodic FTO IOs/CdS NRs/CdSe Clusters with Superior Light Scattering Ability for Improved Photoelectrochemical Performance. *Small* **2020**, *16* (6), 1905826. https://doi.org/10.1002/smll.201905826.
(33) Song, Z.; Zhu, X.; Zeng, Y.; Wang, A.; Li, S.; Fan, Y.; Cai, M.; Cheng, Q.; Wei, Y.; Sun, S. Cobalt Phosphate Cocatalyst Loaded-CdS Nanorod Photoanode with Well-Defined Junctions for Highly Efficient Photoelectrochemical Water Splitting. *Catal Lett* **2020**, *150* (7), 1878–1889. https://doi.org/10.1007/s10562-019-03084-z.
(34) Huang, G.; Lu, C.-H.; Yang, H.-H. Chapter 3 - Magnetic Nanomaterials for Magnetic Bioanalysis. In *Novel Nanomaterials for Biomedical, Environmental and Energy Applications*; Wang, X., Chen, X., Eds.; Micro and Nano Technologies; Elsevier, 2019; pp 89–109. https://doi.org/10.1016/B978-0-12-814497-8.00003-5.
(35) Ullah, H.; Barzgar Vishlaghi, M.; Balkan, T.; ur Rehman, Z.; Kaya, S. Scaling-up Photocatalytic Activity of CdS from Nanorods to Nanowires for the MB Degradation. *Inorganic Chemistry Communications* **2021**, *130*, 108744. https://doi.org/10.1016/j.inoche.2021.108744.
(36) *The Effect of Thermal Treatment on the Morphology and Charge Carrier Dynamics in a Polythiophene–Fullerene Bulk Heterojunction - Savenije - 2005 - Advanced Functional Materials - Wiley Online Library*. https://onlinelibrary.wiley.com/doi/abs/10.1002/adfm.200400559 (accessed 2023-08-08).
(37) Han, S.; Pu, Y.-C.; Zheng, L.; Zhong Zhang, J.; Fang, X. Shell-Thickness Dependent Electron Transfer and Relaxation in Type-II Core–Shell CdS/TiO 2 Structures with Optimized Photoelectrochemical Performance. *Journal of Materials Chemistry A* **2015**, *3* (45), 22627–22635. https://doi.org/10.1039/C5TA07100C.
(38) Skafte, T. L.; Blennow, P.; Hjelm, J.; Graves, C. Carbon Deposition and Sulfur Poisoning during CO2 Electrolysis in Nickel-Based Solid Oxide Cell Electrodes. *Journal of Power Sources* **2018**, *373*, 54–60. https://doi.org/10.1016/j.jpowsour.2017.10.097.
(39) Papurello, D.; Lanzini, A.; Fiorilli, S.; Smeacetto, F.; Singh, R.; Santarelli, M. Sulfur Poisoning in Ni-Anode Solid Oxide Fuel Cells (SOFCs): Deactivation in Single Cells and a Stack. *Chemical Engineering Journal* **2016**, *283*, 1224–1233. https://doi.org/10.1016/j.cej.2015.08.091.
(40) Senadeera, G. K. R.; Sandamali, W. I.; Kumari, J. M. K. W.; Jaseetharan, T.; Weerasinghe, J.; Sonar, P.; Perera, V. P. S.; Rajendra, J. C. N.; Karthikeyan, N.; Dissanayake, M. A. K. L. Morphological and Structural Study on Low Cost SnO2 Counter Electrode and Its Applications in Quantum Dot Sensitized Solar Cells

with Polysulfide Electrolyte. *Materials Science and Engineering: B* **2022**, *286*, 116075. https://doi.org/10.1016/j.mseb.2022.116075.
(41) Zhu, Q.; Xu, Z.; Yi, Q.; Nasir, M.; Xing, M.; Qiu, B.; Zhang, J. Prolonged Electron Lifetime in Sulfur Vacancy-Rich ZnCdS Nanocages by Interstitial Phosphorus Doping for Photocatalytic Water Reduction. *Mater. Chem. Front.* **2020**, *4* (11), 3234–3239. https://doi.org/10.1039/D0QM00464B.
(42) Li, S.; Xu, W.; Meng, L.; Tian, W.; Li, L. Recent Progress on Semiconductor Heterojunction-Based Photoanodes for Photoelectrochemical Water Splitting. *Small Science* **2022**, *2* (5), 2100112. https://doi.org/10.1002/smsc.202100112.
(43) Wang, J.; Pan, Y.; Jiang, L.; Liu, M.; Liu, F.; Jia, M.; Li, J.; Lai, Y. Photoelectrochemical Determination of Cu2+ Using a WO3/CdS Heterojunction Photoanode. *ACS Appl. Mater. Interfaces* **2019**, *11* (41), 37541–37549. https://doi.org/10.1021/acsami.9b10256.
(44) Li, Y.; Wu, Q.; Bu, Q.; Zhang, K.; Lin, Y.; Wang, D.; Zou, X.; Xie, T. An Effective CdS/Ti-Fe2O3 Heterojunction Photoanode: Analyzing Z-Scheme Charge-Transfer Mechanism for Enhanced Photoelectrochemical Water-Oxidation Activity. *Chinese Journal of Catalysis* **2021**, *42* (5), 762–771. https://doi.org/10.1016/S1872-2067(20)63700-7.
(45) Bai, S.; Li, Q.; Han, J.; Yang, X.; Shu, X.; Sun, J.; Sun, L.; Luo, R.; Li, D.; Chen, A. Photoanode of LDH Catalyst Decorated Semiconductor Heterojunction of BiVO4/CdS to Enhance PEC Water Splitting Efficiency. *International Journal of Hydrogen Energy* **2019**, *44* (45), 24642–24652. https://doi.org/10.1016/j.ijhydene.2019.07.214.
(46) Bhat, S. S. M.; Pawar, S. A.; Potphode, D.; Moon, C.-K.; Suh, J. M.; Kim, C.; Choi, S.; Patil, D. S.; Kim, J.-J.; Shin, J. C.; Jang, H. W. Substantially Enhanced Photoelectrochemical Performance of TiO2 Nanorods/CdS Nanocrystals Heterojunction Photoanode Decorated with MoS2 Nanosheets. *Applied Catalysis B: Environmental* **2019**, *259*, 118102. https://doi.org/10.1016/j.apcatb.2019.118102.
(47) Rosman, N. N.; Yunus, R. M.; Shah, N. R. A. M.; Shah, R. M.; Arifin, K.; Minggu, L. J.; Ludin, N. A. An Overview of Co-Catalysts on Metal Oxides for Photocatalytic Water Splitting. *International Journal of Energy Research* **2022**, *46* (9), 11596–11619. https://doi.org/10.1002/er.8001.
(48) Ahmed, R.; Xu, Y.; Zangari, G. Water Splitting vs. Sulfite Oxidation: An Assessment of Photoelectrochemical Performance of TiO2 Nanotubes Modified by CdS/CdSe Nanoparticles. *Electrochimica Acta* **2018**, *259*, 1095–1103. https://doi.org/10.1016/j.electacta.2017.12.088.
(49) Li, H.; Cheng, M.; Zhang, J.; Liu, X.; Zhang, X. MoS2 Co-Catalyst Sensitized 3D TiO2/CdS Photoanodes with Enhanced Photoelectrochemical Performances. *Journal of the American Ceramic Society* **2020**, *103* (10), 5778–5786. https://doi.org/10.1111/jace.17309.
(50) Li, Y.; Liu, Z.; Zhang, J.; Guo, Z.; Xin, Y.; Zhao, L. 1D/0D WO3/CdS Heterojunction Photoanodes Modified with Dual Co-Catalysts for Efficient Photoelectrochemical Water Splitting. *Journal of Alloys and Compounds* **2019**, *790*, 493–501. https://doi.org/10.1016/j.jallcom.2019.03.178.
(51) Wei, L.; Guo, Z.; Jia, X. Probing Photocorrosion Mechanism of CdS Films and Enhancing Photoelectrocatalytic Activity via Cocatalyst. *Catal Lett* **2021**, *151* (1), 56–66. https://doi.org/10.1007/s10562-020-03275-z.
(52) He, J.; Hu, L.; Shao, C.; Jiang, S.; Sun, C.; Song, S. Photocatalytic H2O Overall Splitting into H2 Bubbles by Single Atomic Sulfur Vacancy CdS with Spin

Polarization Electric Field. *ACS Nano* **2021**, *15* (11), 18006–18013. https://doi.org/10.1021/acsnano.1c06524.
(53) Pareek, A.; Thotakuri, R.; Dom, R.; Kim, H. G.; Borse, P. H. Nanostructure Zn–Cu Co-Doped CdS Chalcogenide Electrodes for Opto-Electric-Power and H2 Generation. *International Journal of Hydrogen Energy* **2017**, *42* (1), 125–132. https://doi.org/10.1016/j.ijhydene.2016.10.029.
(54) Liu, B.; Wang, S.; Zhang, G.; Gong, Z.; Wu, B.; Wang, T.; Gong, J. Tandem Cells for Unbiased Photoelectrochemical Water Splitting. *Chemical Society Reviews* **2023**. https://doi.org/10.1039/D3CS00145H.
(55) Chen, Q.; Fan, G.; Fu, H.; Li, Z.; Zou, Z. Tandem Photoelectrochemical Cells for Solar Water Splitting. *Advances in Physics: X* **2018**, *3* (1), 1487267. https://doi.org/10.1080/23746149.2018.1487267.
(56) Chong, R.; Wang, Z.; Lv, J.; Rong, J.; Zhang, L.; Jia, Y.; Wang, L.; Chang, Z.; Wang, X. A Hybrid CoOOH-RGO/Fe2O3 Photoanode with Spatial Charge Separation and Charge Transfer for Efficient Photoelectrochemical Water Oxidation. *Journal of Catalysis* **2021**, *399*, 170–181. https://doi.org/10.1016/j.jcat.2021.05.006.
(57) Guang-Lei, T.; Hong-Bo, H.; Jian-Da, S. Effect of Microstructure of TiO2 Thin Films on Optical Band Gap Energy. *Chinese Phys. Lett.* **2005**, *22* (7), 1787. https://doi.org/10.1088/0256-307X/22/7/062.
(58) Lee, M. G.; Yang, J. W.; Park, I. J.; Lee, T. H.; Park, H.; Cheon, W. S.; Lee, S. A.; Lee, H.; Ji, S. G.; Suh, J. M.; Moon, J.; Kim, J. Y.; Jang, H. W. Tailored BiVO4/In2O3 Nanostructures with Boosted Charge Separation Ability toward Unassisted Water Splitting. *Carbon Energy* **2023**, *5* (6), e321. https://doi.org/10.1002/cey2.321.
(59) Bao, Z.; Li, Z.; Du, Y.; Zhang, M.; Wang, J.; Cai, J.; Lv, J.; Cheng, H.; Zhang, Y.; Wu, Y. A Solid-State Carrier Transport-Prompted Z-Scheme BiVO4 Quantum Dots-Based Photocatalyst for Boosted Photocatalytic Degradation of Antibiotics. *Energy Technology* **2022**, *10* (12), 2200536. https://doi.org/10.1002/ente.202200536.
(60) Batista Deroco, P.; Giarola, J. de F.; Wachholz Júnior, D.; Arantes Lorga, G.; Tatsuo Kubota, L. Chapter Four - Paper-Based Electrochemical Sensing Devices. In *Comprehensive Analytical Chemistry*; Merkoçi, A., Ed.; Paper Based Sensors; Elsevier, 2020; Vol. 89, pp 91–137. https://doi.org/10.1016/bs.coac.2019.11.001.
(61) Cardeña, R.; Cercado, B.; Buitrón, G. Chapter 7 - Microbial Electrolysis Cell for Biohydrogen Production. In *Biohydrogen (Second Edition)*; Pandey, A., Mohan, S. V., Chang, J.-S., Hallenbeck, P. C., Larroche, C., Eds.; Biomass, Biofuels, Biochemicals; Elsevier, 2019; pp 159–185. https://doi.org/10.1016/B978-0-444-64203-5.00007-1.
(62) Devadiga, D.; Selvakumar, M.; Shetty, P.; Santosh, M. S. The Integration of Flexible Dye-Sensitized Solar Cells and Storage Devices towards Wearable Self-Charging Power Systems: A Review. *Renewable and Sustainable Energy Reviews* **2022**, *159*, 112252. https://doi.org/10.1016/j.rser.2022.112252.
(63) Chen, Z.; Deutsch, T. G.; Dinh, H. N.; Domen, K.; Emery, K.; Forman, A. J.; Gaillard, N.; Garland, R.; Heske, C.; Jaramillo, T. F.; Kleiman-Shwarsctein, A.; Miller, E.; Takanabe, K.; Turner, J. Incident Photon-to-Current Efficiency and Photocurrent Spectroscopy. In *Photoelectrochemical Water Splitting: Standards, Experimental Methods, and Protocols*; Chen, Z., Dinh, H. N., Miller, E., Eds.; SpringerBriefs in Energy; Springer: New York, NY, 2013; pp 87–97. https://doi.org/10.1007/978-1-4614-8298-7_7.

(64) Cossar, E.; Houache, M. S. E.; Zhang, Z.; Baranova, E. A. Comparison of Electrochemical Active Surface Area Methods for Various Nickel Nanostructures. *Journal of Electroanalytical Chemistry* **2020**, *870*, 114246. https://doi.org/10.1016/j.jelechem.2020.114246.
(65) Choi, W.; Shin, H.-C.; Kim, J. M.; Choi, J.-Y.; Yoon, W.-S. Modeling and Applications of Electrochemical Impedance Spectroscopy (EIS) for Lithium-Ion Batteries. *J. Electrochem. Sci. Technol* **2020**, *11* (1), 1–13. https://doi.org/10.33961/jecst.2019.00528.
(66) Anantharaj, S.; Noda, S. Appropriate Use of Electrochemical Impedance Spectroscopy in Water Splitting Electrocatalysis. *ChemElectroChem* **2020**, *7* (10), 2297–2308. https://doi.org/10.1002/celc.202000515.
(67) Ciucci, F. Modeling Electrochemical Impedance Spectroscopy. *Current Opinion in Electrochemistry* **2019**, *13*, 132–139. https://doi.org/10.1016/j.coelec.2018.12.003.
(68) Córdoba-Torres, P.; Mesquita, T. J.; Nogueira, R. P. Relationship between the Origin of Constant-Phase Element Behavior in Electrochemical Impedance Spectroscopy and Electrode Surface Structure. *J. Phys. Chem. C* **2015**, *119* (8), 4136–4147. https://doi.org/10.1021/jp512063f.
(69) Bredar, A. R. C.; Chown, A. L.; Burton, A. R.; Farnum, B. H. Electrochemical Impedance Spectroscopy of Metal Oxide Electrodes for Energy Applications. *ACS Appl. Energy Mater.* **2020**, *3* (1), 66–98. https://doi.org/10.1021/acsaem.9b01965.
(70) Gelderman, K.; Lee, L.; Donne, S. W. Flat-Band Potential of a Semiconductor: Using the Mott–Schottky Equation. *J. Chem. Educ.* **2007**, *84* (4), 685. https://doi.org/10.1021/ed084p685.
(71) Fadley, C. S. X-Ray Photoelectron Spectroscopy: Progress and Perspectives. *Journal of Electron Spectroscopy and Related Phenomena* **2010**, *178–179*, 2–32. https://doi.org/10.1016/j.elspec.2010.01.006.
(72) Jiang, N.; Zhang, H. J.; Bao, S. N.; Shen, Y. G.; Zhou, Z. F. XPS Study for Reactively Sputtered Titanium Nitride Thin Films Deposited under Different Substrate Bias. *Physica B: Condensed Matter* **2004**, *352* (1), 118–126. https://doi.org/10.1016/j.physb.2004.07.001.
(73) Li, Q.; Anpo, M.; Wang, X. Application of Photoluminescence Spectroscopy to Elucidate Photocatalytic Reactions at the Molecular Level. *Res Chem Intermed* **2020**, *46* (10), 4325–4344. https://doi.org/10.1007/s11164-020-04209-5.
(74) Gilliland, G. D. Photoluminescence Spectroscopy of Crystalline Semiconductors. *Materials Science and Engineering: R: Reports* **1997**, *18* (3), 99–399. https://doi.org/10.1016/S0927-796X(97)80003-4.
(75) Bunaciu, A. A.; Udriştioiu, E. gabriela; Aboul-Enein, H. Y. X-Ray Diffraction: Instrumentation and Applications. *Critical Reviews in Analytical Chemistry* **2015**, *45* (4), 289–299. https://doi.org/10.1080/10408347.2014.949616.
(76) Hong, S.; Kim, E.; Kim, D.-W.; Sung, T.-H.; No, K. On Measurement of Optical Band Gap of Chromium Oxide Films Containing Both Amorphous and Crystalline Phases. *Journal of Non-Crystalline Solids* **1997**, *221* (2), 245–254. https://doi.org/10.1016/S0022-3093(97)00367-0.
(77) Makuła, P.; Pacia, M.; Macyk, W. How To Correctly Determine the Band Gap Energy of Modified Semiconductor Photocatalysts Based on UV–Vis Spectra. *J. Phys. Chem. Lett.* **2018**, *9* (23), 6814–6817. https://doi.org/10.1021/acs.jpclett.8b02892.
(78) Zhang, S.-L. *Raman Spectroscopy and Its Application in Nanostructures*; John Wiley & Sons, 2012.

(79) Wen, S.; Liu, J.; Deng, J. Chapter 3 - Methods for the Detection and Composition Study of Fluid Inclusions. In *Fluid Inclusion Effect in Flotation of Sulfide Minerals*; Wen, S., Liu, J., Deng, J., Eds.; Elsevier, 2021; pp 27–68. https://doi.org/10.1016/B978-0-12-819845-2.00003-X.
(80) Prabhu, R. S.; Priyanka, R.; Vijay, M.; Vikashini, G. R. K. Field Emission Scanning Electron Microscopy (Fesem) with A Very Big Future in Pharmaceutical Research. *International Journal of Pharmacy and Biological Sciences*.
(81) Titus, D.; James Jebaseelan Samuel, E.; Roopan, S. M. Chapter 12 - Nanoparticle Characterization Techniques. In *Green Synthesis, Characterization and Applications of Nanoparticles*; Shukla, A. K., Iravani, S., Eds.; Micro and Nano Technologies; Elsevier, 2019; pp 303–319. https://doi.org/10.1016/B978-0-08-102579-6.00012-5.
(82) Lone, I. H.; Aslam, J.; Akhter, A. 3 - Characterization of Advanced Green Materials. In *Advanced Green Materials*; Ahmed, S., Ed.; Woodhead Publishing in Materials; Woodhead Publishing, 2021; pp 31–41. https://doi.org/10.1016/B978-0-12-819988-6.00003-3.
(83) Yen, H.-W. Advanced Characterization on Nanostructure in Steels. In *Encyclopedia of Materials: Metals and Alloys*; Caballero, F. G., Ed.; Elsevier: Oxford, 2022; pp 250–279. https://doi.org/10.1016/B978-0-12-819726-4.00133-2.
(84) Chen, X.; Zhang, Z.; Chi, L.; Nair, A. K.; Shangguan, W.; Jiang, Z. Recent Advances in Visible-Light-Driven Photoelectrochemical Water Splitting: Catalyst Nanostructures and Reaction Systems. *Nano-Micro Lett.* **2016**, *8* (1), 1–12. https://doi.org/10.1007/s40820-015-0063-3.
(85) Prasad, C.; Madkhali, N.; Won, J. S.; Lee, J. E.; Sangaraju, S.; Choi, H. Y. CdS Based Heterojunction for Water Splitting: A Review. *Materials Science and Engineering: B* **2023**, *292*, 116413. https://doi.org/10.1016/j.mseb.2023.116413.
(86) Chen, S.; Li, C.; Hou, Z. A Novel in Situ Synthesis of TiO2/CdS Heterojunction for Improving Photoelectrochemical Water Splitting. *International Journal of Hydrogen Energy* **2019**, *44* (47), 25473–25485. https://doi.org/10.1016/j.ijhydene.2019.08.049.
(87) Ruan, M.; Cai, X.; Lan, Y.; Xing, H. Hexagonal CdS Photoanode Modified with Pt and Cobalt Phosphate Cocatalyst for Efficient Photoelectrochemical Performance. *Materials Letters* **2020**, *260*, 126947. https://doi.org/10.1016/j.matlet.2019.126947.
(88) Zhang, J.; Cui, J.; Eslava, S. Oxygen Evolution Catalysts at Transition Metal Oxide Photoanodes: Their Differing Roles for Solar Water Splitting. *Advanced Energy Materials* **2021**, *11* (13), 2003111. https://doi.org/10.1002/aenm.202003111.
(89) Sun, M.-H.; Qi, M.-Y.; Tang, Z.-R.; Xu, Y.-J. Dual Cocatalysts Decorated CdS Nanoparticles for Efficient Dehydrocoupling of Thiols into Disulfides. *Applied Catalysis B: Environmental* **2023**, *321*, 122019. https://doi.org/10.1016/j.apcatb.2022.122019.
(90) Zheng, S.; Han, L.; Luo, X.; Sun, L.; Li, N.; Zhang, Z.; Li, X. Polydopamine and Nafion Bi-Layer Passivation Modified CdS Photoanode for Photoelectrochemical Hydrogen Evolution. *International Journal of Energy Research* **2022**, *46* (4), 4506–4515. https://doi.org/10.1002/er.7444.
(91) Wang, R.; Wang, L.; Zhou, Y.; Zou, Z. Al-ZnO/CdS Photoanode Modified with a Triple Functions Conformal TiO2 Film for Enhanced Photoelectrochemical Efficiency and Stability. *Applied Catalysis B: Environmental* **2019**, *255*, 117738. https://doi.org/10.1016/j.apcatb.2019.05.040.

(92) Vanalakar, S. A.; Suryawanshi, M. P.; Mali, S. S.; Moholkar, A. V.; Kim, J. Y.; Patil, P. S.; Kim, J. H. Simplistic Surface Active Agents Mediated Morphological Tweaking of CdS Thin Films for Photoelectrochemical Solar Cell Performance. *Current Applied Physics* **2014**, *14* (12), 1669–1676. https://doi.org/10.1016/j.cap.2014.09.011.
(93) Dumbrava, A.; Prodan, G.; Berger, D.; Bica, M. Properties of PEG-Capped CdS Nanopowders Synthesized under Very Mild Conditions. *Powder Technology* **2015**, *270*, 197–204. https://doi.org/10.1016/j.powtec.2014.10.012.
(94) Senasu, T.; Chankhanittha, T.; Hemavibool, K.; Nanan, S. Visible-Light-Responsive Photocatalyst Based on ZnO/CdS Nanocomposite for Photodegradation of Reactive Red Azo Dye and Ofloxacin Antibiotic. *Materials Science in Semiconductor Processing* **2021**, *123*, 105558. https://doi.org/10.1016/j.mssp.2020.105558.
(95) Ben Brahim, N.; Poggi, M.; Lambry, J.-C.; Bel Haj Mohamed, N.; Ben Chaâbane, R.; Negrerie, M. Density of Grafted Chains in Thioglycerol-Capped CdS Quantum Dots Determines Their Interaction with Aluminum(III) in Water. *Inorg. Chem.* **2018**, *57* (9), 4979–4988. https://doi.org/10.1021/acs.inorgchem.7b03254.
(96) Muniyappan, S.; Solaiyammal, T.; Keerthana, B. G. T.; Vivek, P.; Murugakoothan, P. Influence of Annealing Temperature on Structural, Morphological and Optical Properties of CTAB Assisted Cadmium Sulphide (CdS) Quantum Dots: Promising Candidate for Quantum Dot Sensitized Solar Cell (QDSSC) Applications. *J Mater Sci: Mater Electron* **2017**, *28* (15), 11317–11324. https://doi.org/10.1007/s10854-017-6924-4.
(97) Li, Q.; Antony, R. P.; Wong, L. H.; Ng, D. H. L. Promotional Effects of Cetyltrimethylammonium Bromide Surface Modification on a Hematite Photoanode for Photoelectrochemical Water Splitting. *RSC Adv.* **2015**, *5* (121), 100142–100146. https://doi.org/10.1039/C5RA20529H.
(98) Sun, J.; Wang, Y.; Guo, S.; Wan, B.; Dong, L.; Gu, Y.; Song, C.; Pan, C.; Zhang, Q.; Gu, L.; Pan, F.; Zhang, J. Lateral 2D WSe2 p–n Homojunction Formed by Efficient Charge-Carrier-Type Modulation for High-Performance Optoelectronics. *Advanced Materials* **2020**, *32* (9), 1906499. https://doi.org/10.1002/adma.201906499.
(99) Song, Z.; Zhu, X.; Zeng, Y.; Wang, A.; Li, S.; Fan, Y.; Cai, M.; Cheng, Q.; Wei, Y.; Sun, S. Cobalt Phosphate Cocatalyst Loaded-CdS Nanorod Photoanode with Well-Defined Junctions for Highly Efficient Photoelectrochemical Water Splitting. *Catal Lett* **2020**, *150* (7), 1878–1889. https://doi.org/10.1007/s10562-019-03084-z.
(100) Alkuam, E.; Mohammed, M.; Chen, T.-P. Fabrication of CdS Nanorods and Nanoparticles with PANI for (DSSCs) Dye-Sensitized Solar Cells. *Solar Energy* **2017**, *150*, 317–324. https://doi.org/10.1016/j.solener.2017.04.056.
(101) Dong, Y.-J.; Liao, J.-F.; Kong, Z.-C.; Xu, Y.-F.; Chen, Z.-J.; Chen, H.-Y.; Kuang, D.-B.; Fenske, D.; Su, C.-Y. Conformal Coating of Ultrathin Metal-Organic Framework on Semiconductor Electrode for Boosted Photoelectrochemical Water Oxidation. *Applied Catalysis B: Environmental* **2018**, *237*, 9–17. https://doi.org/10.1016/j.apcatb.2018.05.059.
(102) Zhao, Q.; Liu, Z.; Guo, Z.; Ruan, M.; Yan, W. The Collaborative Mechanism of Surface S-Vacancies and Piezoelectric Polarization for Boosting CdS Photoelectrochemical Performance. *Chemical Engineering Journal* **2022**, *433*, 133226. https://doi.org/10.1016/j.cej.2021.133226.

(103) Niu, S.; Li, S.; Du, Y.; Han, X.; Xu, P. How to Reliably Report the Overpotential of an Electrocatalyst. *ACS Energy Lett.* **2020**, *5* (4), 1083–1087. https://doi.org/10.1021/acsenergylett.0c00321.
(104) Mahdi, H. S.; Parveen, A.; Agrawal, S.; Azam, A. Microstructural and Optical Properties of Sol Gel Synthesized CdS Nano Particles Using CTAB as a Surfactant. *AIP Conference Proceedings* **2017**, *1832* (1), 050012. https://doi.org/10.1063/1.4980245.
(105) Lippitz, A.; Friedrich, J. F.; Unger, W. E. S. Plasma Bromination of HOPG Surfaces: A NEXAFS and Synchrotron XPS Study. *Surface Science* **2013**, *611*, L1–L7. https://doi.org/10.1016/j.susc.2013.01.020.
(106) Hota, G.; Idage, S. B.; Khilar, K. C. Characterization of Nano-Sized CdS–Ag2S Core-Shell Nanoparticles Using XPS Technique. *Colloids and Surfaces A: Physicochemical and Engineering Aspects* **2007**, *293* (1–3), 5–12. https://doi.org/10.1016/j.colsurfa.2006.06.036.
(107) Innocenzi, P.; Falcaro, P.; Grosso, D.; Babonneau, F. Order−Disorder Transitions and Evolution of Silica Structure in Self-Assembled Mesostructured Silica Films Studied through FTIR Spectroscopy. *J. Phys. Chem. B* **2003**, *107* (20), 4711–4717. https://doi.org/10.1021/jp026609z.
(108) De Barros, M. I.; Bouchet, J.; Raoult, I.; Le Mogne, Th.; Martin, J. M.; Kasrai, M.; Yamada, Y. Friction Reduction by Metal Sulfides in Boundary Lubrication Studied by XPS and XANES Analyses. *Wear* **2003**, *254* (9), 863–870. https://doi.org/10.1016/S0043-1648(03)00237-0.
(109) Xiao, F.-X.; Hung, S.-F.; Tao, H. B.; Miao, J.; Yang, H. B.; Liu, B. Spatially Branched Hierarchical ZnO Nanorod-TiO2 Nanotube Array Heterostructures for Versatile Photocatalytic and Photoelectrocatalytic Applications: Towards Intimate Integration of 1D–1D Hybrid Nanostructures. *Nanoscale* **2014**, *6* (24), 14950–14961. https://doi.org/10.1039/C4NR04886E.
(110) Thangadurai, P.; Balaji, S.; Manoharan, P. T. Growth and Mechanism of CdS Nanorods by Microstructure Analysis. *Materials Chemistry and Physics* **2009**, *114* (1), 420–424. https://doi.org/10.1016/j.matchemphys.2008.09.048.
(111) Na, Y.; Hu, B.; Yang, Q.-L.; Liu, J.; Zhou, L.; Fan, R.-Q.; Yang, Y.-L. CdS Quantum Dot Sensitized P-Type NiO as Photocathode with Integrated Cobaloxime in Photoelectrochemical Cell for Water Splitting. *Chinese Chemical Letters* **2015**, *26* (1), 141–144. https://doi.org/10.1016/j.cclet.2014.09.011.
(112) Orazem, M. E.; Frateur, I.; Tribollet, B.; Vivier, V.; Marcelin, S.; Pébère, N.; Bunge, A. L.; White, E. A.; Riemer, D. P.; Musiani, M. Dielectric Properties of Materials Showing Constant-Phase-Element (CPE) Impedance Response. *J. Electrochem. Soc.* **2013**, *160* (6), C215. https://doi.org/10.1149/2.033306jes.
(113) Jostar. T, S.; Devadason, S.; Suthagar, J. Effect of CdS Layers on Opto-Electrical Properties of Chemically Prepared ZnS/CdS/TiO2 Photoanodes. *Materials Science in Semiconductor Processing* **2015**, *34*, 65–73. https://doi.org/10.1016/j.mssp.2015.02.021.
(114) Usman, E.; Barzgar Vishlaghi, M.; Kahraman, A.; Solati, N.; Kaya, S. Modifying the Electron-Trapping Process at the BiVO4 Surface States via the TiO2 Overlayer for Enhanced Water Oxidation. *ACS Appl. Mater. Interfaces* **2021**, *13* (50), 60602–60611. https://doi.org/10.1021/acsami.1c16847.
(115) Corby, S.; Pastor, E.; Dong, Y.; Zheng, X.; Francàs, L.; Sachs, M.; Selim, S.; Kafizas, A.; Bakulin, A. A.; Durrant, J. R. Charge Separation, Band-Bending, and Recombination in WO3 Photoanodes. *J. Phys. Chem. Lett.* **2019**, *10* (18), 5395–5401. https://doi.org/10.1021/acs.jpclett.9b01935.

(116) Guo, C.; Tian, K.; Wang, L.; Liang, F.; Wang, F.; Chen, D.; Ning, J.; Zhong, Y.; Hu, Y. Approach of Fermi Level and Electron-Trap Level in Cadmium Sulfide Nanorods via Molybdenum Doping with Enhanced Carrier Separation for Boosted Photocatalytic Hydrogen Production. *Journal of Colloid and Interface Science* **2021**, *583*, 661–671. https://doi.org/10.1016/j.jcis.2020.09.093.

(117) Kasem, K. K. Long-Term Activity of Thermoplastic Gel Electrolyte in a Photo-Electrochemical Assembly Involving Poly Bithiophene (PBTh) as Photoactive Working Electrode. *Journal of Materials Science and Chemical Engineering* **2021**, *9* (6), 1–11. https://doi.org/10.4236/msce.2021.96001.

(118) Fermín, D. J.; Ponomarev, E. A.; Peter, L. M. A Kinetic Study of CdS Photocorrosion by Intensity Modulated Photocurrent and Photoelectrochemical Impedance Spectroscopy. *Journal of Electroanalytical Chemistry* **1999**, *473* (1), 192–203. https://doi.org/10.1016/S0022-0728(99)00109-6.

(119) Caliari, P. C.; Pacheco, M. J.; Ciríaco, L. F.; Lopes, A. M. C. Anodic Oxidation of Sulfide to Sulfate: Effect of the Current Density on the Process Kinetics. *J. Braz. Chem. Soc.* **2017**, *28*, 557–566. https://doi.org/10.5935/0103-5053.20160197.

(120) Attias, R.; Dlugatch, B.; Chae, M. S.; Goffer, Y.; Aurbach, D. Changes in the Interfacial Charge-Transfer Resistance of Mg Metal Electrodes, Measured by Dynamic Electrochemical Impedance Spectroscopy. *Electrochemistry Communications* **2021**, *124*, 106952. https://doi.org/10.1016/j.elecom.2021.106952.

(121) deQuilettes, D. W.; Frohna, K.; Emin, D.; Kirchartz, T.; Bulovic, V.; Ginger, D. S.; Stranks, S. D. Charge-Carrier Recombination in Halide Perovskites: Focus Review. *Chem. Rev.* **2019**, *119* (20), 11007–11019. https://doi.org/10.1021/acs.chemrev.9b00169.

(122) Lee, Y.-G.; Park, S.; Cho, W.; Son, T.; Sudhagar, P.; Jung, J. H.; Wooh, S.; Char, K.; Kang, Y. S. Effective Passivation of Nanostructured TiO_2 Interfaces with PEG-Based Oligomeric Coadsorbents To Improve the Performance of Dye-Sensitized Solar Cells. *J. Phys. Chem. C* **2012**, *116* (11), 6770–6777. https://doi.org/10.1021/jp210360n.

(123) Burke, T. M.; Sweetnam, S.; Vandewal, K.; McGehee, M. D. Beyond Langevin Recombination: How Equilibrium Between Free Carriers and Charge Transfer States Determines the Open-Circuit Voltage of Organic Solar Cells. *Advanced Energy Materials* **2015**, *5* (11), 1500123. https://doi.org/10.1002/aenm.201500123.

(124) Su, J.; Liu, C.; Liu, D.; Li, M.; Zhou, J. Enhanced Photoelectrochemical Performance of the BiVO4/Zn:BiVO4 Homojunction for Water Oxidation. *ChemCatChem* **2016**, *8* (20), 3279–3286. https://doi.org/10.1002/cctc.201600767.

(125) Chakhari, W.; Ben Naceur, J.; Ben Taieb, S.; Ben Assaker, I.; Chtourou, R. Fe-Doped TiO2 Nanorods with Enhanced Electrochemical Properties as Efficient Photoanode Materials. *Journal of Alloys and Compounds* **2017**, *708*, 862–870. https://doi.org/10.1016/j.jallcom.2016.12.181.

(126) Roh, B.; Macdonald, D. D. Effect of Oxygen Vacancies in Anodic Titanium Oxide Films on the Kinetics of the Oxygen Electrode Reaction. *Russ J Electrochem* **2007**, *43* (2), 125–135. https://doi.org/10.1134/S1023193507020012.

(127) Fu, Y.; Dong, C.-L.; Zhou, Z.; Lee, W.-Y.; Chen, J.; Guo, P.; Zhao, L.; Shen, S. Solution Growth of Ta-Doped Hematite Nanorods for Efficient Photoelectrochemical Water Splitting: A Tradeoff between Electronic Structure and Nanostructure Evolution. *Physical Chemistry Chemical Physics* **2016**, *18* (5), 3846–3853. https://doi.org/10.1039/C5CP07479G.

(128) Sharma, K.; Kumar, A.; Ahamad, T.; Le, Q. V.; Raizada, P.; Singh, A.; Nguyen, L. H.; Thakur, S.; Nguyen, V.-H.; Singh, P. Sulphur Vacancy Defects Engineered Metal Sulfides for Amended Photo(Electro)Catalytic Water Splitting: A Review. *Journal of Materials Science & Technology* **2023**, *152*, 50–64. https://doi.org/10.1016/j.jmst.2022.11.053.

(129) Cheng, L.; Li, Y.; Chen, A.; Zhu, Y.; Li, C. Impacts on Carbon Dioxide Electroreduction of Cadmium Sulfides via Continuous Surface Sulfur Vacancy Engineering. *Chemical Communications* **2020**, *56* (4), 563–566. https://doi.org/10.1039/C9CC08330H.

(130) Shi, Q.; Murcia-López, S.; Tang, P.; Flox, C.; Morante, J. R.; Bian, Z.; Wang, H.; Andreu, T. Role of Tungsten Doping on the Surface States in BiVO4 Photoanodes for Water Oxidation: Tuning the Electron Trapping Process. *ACS Catal.* **2018**, *8* (4), 3331–3342. https://doi.org/10.1021/acscatal.7b04277.

(131) Bassi, P. S.; Antony, R. P.; Boix, P. P.; Fang, Y.; Barber, J.; Wong, L. H. Crystalline Fe2O3/Fe2TiO5 Heterojunction Nanorods with Efficient Charge Separation and Hole Injection as Photoanode for Solar Water Oxidation. *Nano Energy* **2016**, *22*, 310–318. https://doi.org/10.1016/j.nanoen.2016.02.013.

(132) Wang, H.; Lindgren, T.; He, J.; Hagfeldt, A.; Lindquist, S.-E. Photolelectrochemistry of Nanostructured WO $_3$ Thin Film Electrodes for Water Oxidation: Mechanism of Electron Transport. *J. Phys. Chem. B* **2000**, *104* (24), 5686–5696. https://doi.org/10.1021/jp0002751.

(133) Liu, C.; Zhang, C.; Yin, G.; Zhang, T.; Wang, W.; Ou, G.; Jin, H.; Chen, Z. A Three-Dimensional Branched TiO $_2$ Photoanode with an Ultrathin Al $_2$ O $_3$ Passivation Layer and a NiOOH Cocatalyst toward Photoelectrochemical Water Oxidation. *ACS Appl. Mater. Interfaces* **2021**, *13* (11), 13301–13310. https://doi.org/10.1021/acsami.1c00948.

(134) Marandi, M.; Nazari, M. Application of TiO2 Hollow Spheres and ZnS/SiO2 Double-Passivaiting Layers in the Photoanode of the CdS/CdSe QDs Sensitized Solar Cells for the Efficiency Enhancement. *Solar Energy* **2021**, *216*, 48–60. https://doi.org/10.1016/j.solener.2020.11.057.

(135) Maity, D.; Pal, D.; Saha, S.; Punetha, P.; Sarkar, D.; De, D.; Khan, G. G.; Mandal, K. CeOx as Surface Passivation and Hole Transfer Catalyst Layer Boosting Solar Water Oxidation of ZnFe2O4 Nanorods Photoanode. *Advanced Materials Interfaces* **2023**, *10* (2), 2201645. https://doi.org/10.1002/admi.202201645.

(136) Hsu, S.-H.; Hung, S.-F.; Chien, S.-H. CdS Sensitized Vertically Aligned Single Crystal TiO2 Nanorods on Transparent Conducting Glass with Improved Solar Cell Efficiency and Stability Using ZnS Passivation Layer. *Journal of Power Sources* **2013**, *233*, 236–243. https://doi.org/10.1016/j.jpowsour.2013.01.089.

(137) Wang, L.; Liu, Z.; Zhang, J.; Jia, Y.; Huang, J.; Mei, Q.; Wang, Q. Boosting Charge Separation of BiVO4 Photoanode Modified with 2D Metal-Organic Frameworks Nanosheets for High-Performance Photoelectrochemical Water Splitting. *Chinese Chemical Letters* **2023**, *34* (6), 108007. https://doi.org/10.1016/j.cclet.2022.108007.

(138) Ahmed, M. G.; Kretschmer, I. E.; Kandiel, T. A.; Ahmed, A. Y.; Rashwan, F. A.; Bahnemann, D. W. A Facile Surface Passivation of Hematite Photoanodes with TiO2 Overlayers for Efficient Solar Water Splitting. *ACS Appl. Mater. Interfaces* **2015**, *7* (43), 24053–24062. https://doi.org/10.1021/acsami.5b07065.

(139) Wan, X.; Xu, Y.; Wang, X.; Guan, X.; Fu, Y.; Hu, C.; Hu, H.; Rong, N. Atomic Layer Deposition Assisted Surface Passivation on Bismuth Vanadate Photoanodes

for Enhanced Solar Water Oxidation. *Applied Surface Science* **2022**, *573*, 151492. https://doi.org/10.1016/j.apsusc.2021.151492.
(140) Imrich, T.; Neumann-Spallart, M.; Krýsová, H.; Tarábková, H.; Nebel, R.; Krýsa, J. Ti Doped Hematite Photoanodes: Protective Coverage by Titania Overlayers. *Journal of Photochemistry and Photobiology A: Chemistry* **2023**, *445*, 115026. https://doi.org/10.1016/j.jphotochem.2023.115026.
(141) Johnson, R. W.; Hultqvist, A.; Bent, S. F. A Brief Review of Atomic Layer Deposition: From Fundamentals to Applications. *Materials Today* **2014**, *17* (5), 236–246. https://doi.org/10.1016/j.mattod.2014.04.026.
(142) Wang, Z.; Wang, L. Role of Oxygen Vacancy in Metal Oxide Based Photoelectrochemical Water Splitting. *EcoMat* **2021**, *3* (1), e12075. https://doi.org/10.1002/eom2.12075.
(143) Ahmed, M. G.; Kretschmer, I. E.; Kandiel, T. A.; Ahmed, A. Y.; Rashwan, F. A.; Bahnemann, D. W. A Facile Surface Passivation of Hematite Photoanodes with TiO $_2$ Overlayers for Efficient Solar Water Splitting. *ACS Appl. Mater. Interfaces* **2015**, *7* (43), 24053–24062. https://doi.org/10.1021/acsami.5b07065.
(144) She, H.; Yue, P.; Huang, J.; Wang, L.; Wang, Q. One-Step Hydrothermal Deposition of F:FeOOH onto BiVO4 Photoanode for Enhanced Water Oxidation. *Chemical Engineering Journal* **2020**, *392*, 123703. https://doi.org/10.1016/j.cej.2019.123703.
(145) Gao, X.-F.; Sun, W.-T.; Hu, Z.-D.; Ai, G.; Zhang, Y.-L.; Feng, S.; Li, F.; Peng, L.-M. An Efficient Method To Form Heterojunction CdS/TiO2 Photoelectrodes Using Highly Ordered TiO2 Nanotube Array Films. *J. Phys. Chem. C* **2009**, *113* (47), 20481–20485. https://doi.org/10.1021/jp904320d.
(146) Momtazi, L.; Sønsteby, H. H.; Nilsen, O. Biocompatible Organic–Inorganic Hybrid Materials Based on Nucleobases and Titanium Developed by Molecular Layer Deposition. *Beilstein J. Nanotechnol.* **2019**, *10* (1), 399–411. https://doi.org/10.3762/bjnano.10.39.
(147) Hino, M.; Kurashige, M.; Matsuhashi, H.; Arata, K. The Surface Structure of Sulfated Zirconia: Studies of XPS and Thermal Analysis. *Thermochimica Acta* **2006**, *441* (1), 35–41. https://doi.org/10.1016/j.tca.2005.11.042.
(148) Wang, Y.; Zhu, L.; Liu, Y.; Vovk, E. I.; Lang, J.; Zhou, Z.; Gao, P.; Li, S.; Yang, Y. Understanding Surface Structures of In2O3 Catalysts during CO2 Hydrogenation Reaction Using Time-Resolved IR, XPS with in Situ Treatment, and DFT Calculations. *Applied Surface Science* **2023**, *631*, 157534. https://doi.org/10.1016/j.apsusc.2023.157534.
(149) Kumar, P.; Saxena, N.; Chandra, R.; Gupta, V.; Agarwal, A.; Kanjilal, D. Nanotwinning and Structural Phase Transition in CdS Quantum Dots. *Nanoscale Res Lett* **2012**, *7* (1), 584. https://doi.org/10.1186/1556-276X-7-584.
(150) Sun, Q.; Yu, Z.; Jiang, R.; Hou, Y.; Sun, L.; Qian, L.; Li, F.; Li, M.; Ran, Q.; Zhang, H. CoP QD Anchored Carbon Skeleton Modified CdS Nanorods as a Co-Catalyst for Photocatalytic Hydrogen Production. *Nanoscale* **2020**, *12* (37), 19203–19212. https://doi.org/10.1039/D0NR05268J.
(151) Kumar Vishwakarma, A.; Majid, S. S.; Yadava, L. XANES Analysis and Structural Properties of CdS-Doped TiO2. *Vacuum* **2019**, *165*, 239–245. https://doi.org/10.1016/j.vacuum.2019.04.040.
(152) Martínez-Landeros, V. H.; Hernandez-Como, N.; Gutierrez-Heredia, G.; Quevedo-Lopez, M. A.; Aguirre-Tostado, F. S. Structural, Chemical and Electrical Properties of CdS Thin Films Fabricated by Pulsed Laser Deposition Using

Varying Background Gas Pressure. *Thin Solid Films* **2019**, *682*, 24–28. https://doi.org/10.1016/j.tsf.2019.05.014.
(153) Chandiran, A. K.; Yella, A.; Mayer, M. T.; Gao, P.; Nazeeruddin, M. K.; Grätzel, M. Sub-Nanometer Conformal TiO2 Blocking Layer for High Efficiency Solid-State Perovskite Absorber Solar Cells. *Advanced Materials* **2014**, *26* (25), 4309–4312. https://doi.org/10.1002/adma.201306271.
(154) Brezesinski, T.; Wang, J.; Polleux, J.; Dunn, B.; Tolbert, S. H. Templated Nanocrystal-Based Porous TiO2 Films for Next-Generation Electrochemical Capacitors. *J. Am. Chem. Soc.* **2009**, *131* (5), 1802–1809. https://doi.org/10.1021/ja8057309.
(155) Xi, L.; Bassi, P. S.; Chiam, S. Y.; Mak, W. F.; Tran, P. D.; Barber, J.; Chye Loo, J. S.; Wong, L. H. Surface Treatment of Hematite Photoanodes with Zinc Acetate for Water Oxidation. *Nanoscale* **2012**, *4* (15), 4430. https://doi.org/10.1039/c2nr30862b.
(156) Chen, H.; Li, J.; Yang, W.; Balaghi, S. E.; Triana, C. A.; Mavrokefalos, C. K.; Patzke, G. R. The Role of Surface States on Reduced TiO2@BiVO4 Photoanodes: Enhanced Water Oxidation Performance through Improved Charge Transfer. *ACS Catal.* **2021**, *11* (13), 7637–7646. https://doi.org/10.1021/acscatal.1c00686.
(157) Zhong, M.; Hisatomi, T.; Kuang, Y.; Zhao, J.; Liu, M.; Iwase, A.; Jia, Q.; Nishiyama, H.; Minegishi, T.; Nakabayashi, M.; Shibata, N.; Niishiro, R.; Katayama, C.; Shibano, H.; Katayama, M.; Kudo, A.; Yamada, T.; Domen, K. Surface Modification of CoOx Loaded BiVO4 Photoanodes with Ultrathin P-Type NiO Layers for Improved Solar Water Oxidation. *J. Am. Chem. Soc.* **2015**, *137* (15), 5053–5060. https://doi.org/10.1021/jacs.5b00256.
(158) Licht, S.; Hodes, G.; Manassen, J. Numerical Analysis of Aqueous Polysulfide Solutions and Its Application to Cadmium Chalcogenide/Polysulfide Photoelectrochemical Solar Cells. *Inorg. Chem.* **1986**, *25* (15), 2486–2489. https://doi.org/10.1021/ic00235a003.
(159) *Hydrogen sulfide splitting using solar energy and hematite photo-anodes | Elsevier Enhanced Reader*. https://doi.org/10.1016/j.electacta.2019.05.031.
(160) Yuan, Y. J.; Kuriyama, H. Determination of Hydrogen Sulfide in a Yeast Culture Solution by Flow Analysis Utilising Methylene Blue Spectrophotometric Detection. *Biotechnology Letters* **2000**, *22* (9), 795–799. https://doi.org/10.1023/A:1005616505959.
(161) Rozan, T. F.; Theberge, S. M.; Luther, G. Quantifying Elemental Sulfur (S0), Bisulfide (HS−) and Polysulfides (Sx2−) Using a Voltammetric Method. *Analytica Chimica Acta* **2000**, *415* (1), 175–184. https://doi.org/10.1016/S0003-2670(00)00844-8.
(162) Luo, T.; Bai, J.; Li, J.; Zeng, Q.; Ji, Y.; Qiao, L.; Li, X.; Zhou, B. Self-Driven Photoelectrochemical Splitting of H_2S for S and H_2 Recovery and Simultaneous Electricity Generation. *Environ. Sci. Technol.* **2017**, *51* (21), 12965–12971. https://doi.org/10.1021/acs.est.7b03116.
(163) *Frontiers | Sulfide intrusion in seagrasses assessed by stable sulfur isotopes—a synthesis of current results*. https://www.frontiersin.org/articles/10.3389/fmars.2014.00064/full (accessed 2023-07-30).
(164) Ghayad, I. M.; Al Kharafi, F. M.; Saad, A. Y.; Ateya, B. G. Electrochemical Oxidation of Sulfide Ions on Platinum Electrodes. *MAS* **2010**, *4* (3), p2. https://doi.org/10.5539/mas.v4n3p2.

(165) Kong, Y.; Sun, H.; Fan, W.; Wang, L.; Zhao, H.; Zhao, X.; Yuan, S. Enhanced Photoelectrochemical Performance of Tungsten Oxide Film by Bifunctional Au Nanoparticles. *RSC Advances* **2017**, *7* (25), 15201–15210. https://doi.org/10.1039/C7RA01426K.

(166) Kaviyarasu, K.; Manikandan, E.; Paulraj, P.; Mohamed, S. B.; Kennedy, J. One Dimensional Well-Aligned CdO Nanocrystal by Solvothermal Method. *Journal of Alloys and Compounds* **2014**, *593*, 67–70. https://doi.org/10.1016/j.jallcom.2014.01.071.

(167) Wang, J.; Chen, J.; Liu, F.; Jia, M.; Zhang, Z.; Liu, M.; Jiang, L. Renewable WO3/Bi2O3 Heterojunction for Photoelectrochemical and Visual Dual-Mode Detection of Hydrogen Sulfide. *Sensors and Actuators B: Chemical* **2022**, *369*, 132274. https://doi.org/10.1016/j.snb.2022.132274.

(168) El-Denglawey, A.; Dongol, M.; El-Nahass, M. M. Photoinduced Absorption Edge Shift of As20Se60Tl20 Films. *Journal of Luminescence* **2010**, *130* (5), 801–804. https://doi.org/10.1016/j.jlumin.2009.11.036.

(169) Maabong, K.; Machatine, A. G.; Hu, Y.; Braun, A.; Nambala, F. J.; Diale, M. Morphology, Structural and Optical Properties of Iron Oxide Thin Film Photoanodes in Photoelectrochemical Cell: Effect of Electrochemical Oxidation. *Physica B: Condensed Matter* **2016**, *480*, 91–94. https://doi.org/10.1016/j.physb.2015.08.010.

(170) Li, H.; Li, J.; Zhu, Y.; Xie, W.; Shao, R.; Yao, X.; Gao, A.; Yin, Y. Cd2+-Doped Amorphous TiO2 Hollow Spheres for Robust and Ultrasensitive Photoelectrochemical Sensing of Hydrogen Sulfide. *Anal. Chem.* **2018**, *90* (8), 5496–5502. https://doi.org/10.1021/acs.analchem.8b01178.

(171) Li, D. G.; Wang, J. D.; Chen, D. R.; Liang, P. Influences of PH Value, Temperature, Chloride Ions and Sulfide Ions on the Corrosion Behaviors of 316L Stainless Steel in the Simulated Cathodic Environment of Proton Exchange Membrane Fuel Cell. *Journal of Power Sources* **2014**, *272*, 448–456. https://doi.org/10.1016/j.jpowsour.2014.06.121.

(172) Proskuryakov, Y. Y.; Durose, K.; Al Turkestani, M. K.; Mora-Seró, I.; Garcia-Belmonte, G.; Fabregat-Santiago, F.; Bisquert, J.; Barrioz, V.; Lamb, D.; Irvine, S. J. C.; Jones, E. W. Impedance Spectroscopy of Thin-Film CdTe/CdS Solar Cells under Varied Illumination. *Journal of Applied Physics* **2009**, *106* (4), 044507. https://doi.org/10.1063/1.3204484.

Appendix A: Supporting Information for Chapter 3

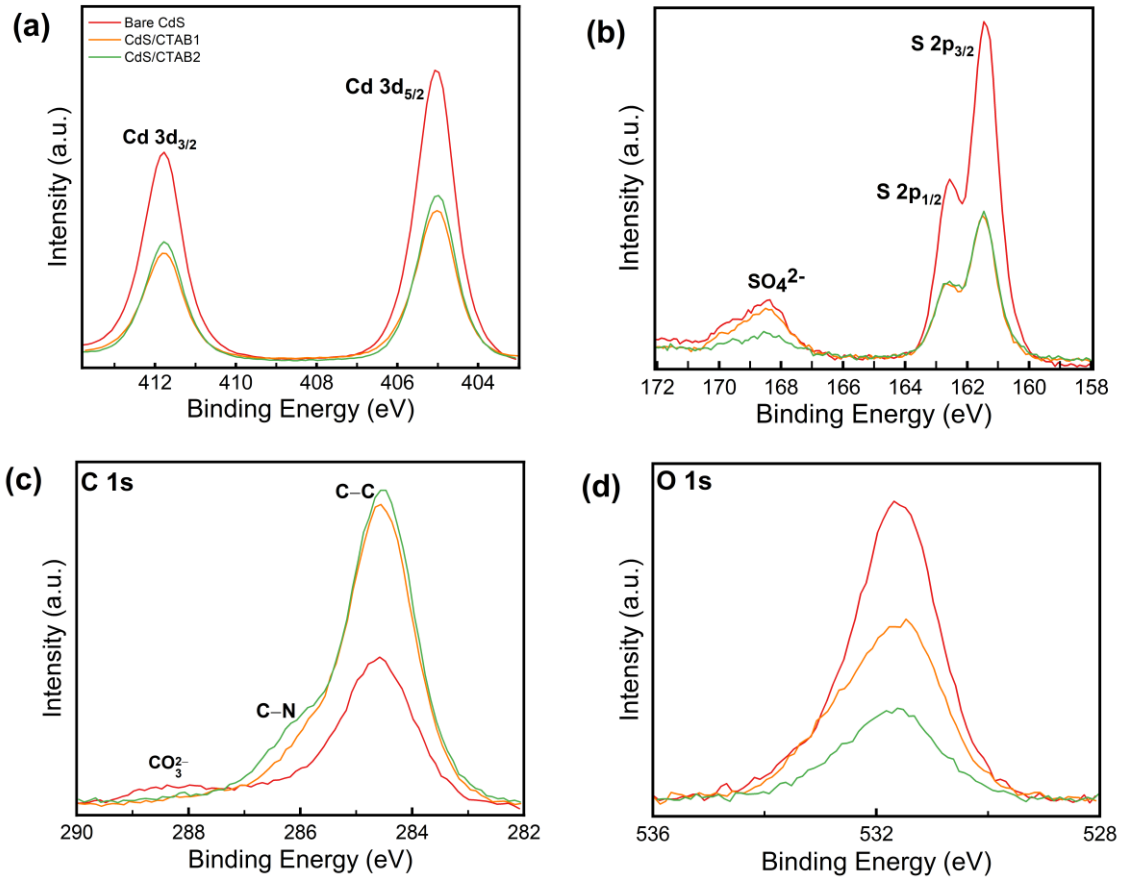

Figure 3A.1 *(a) Cd 3d, (b) S 2p, (c) C 1s, and (d) O 1s XPS spectra of bare CdS, CdS/CTAB1, and CdS/CTAB2.*

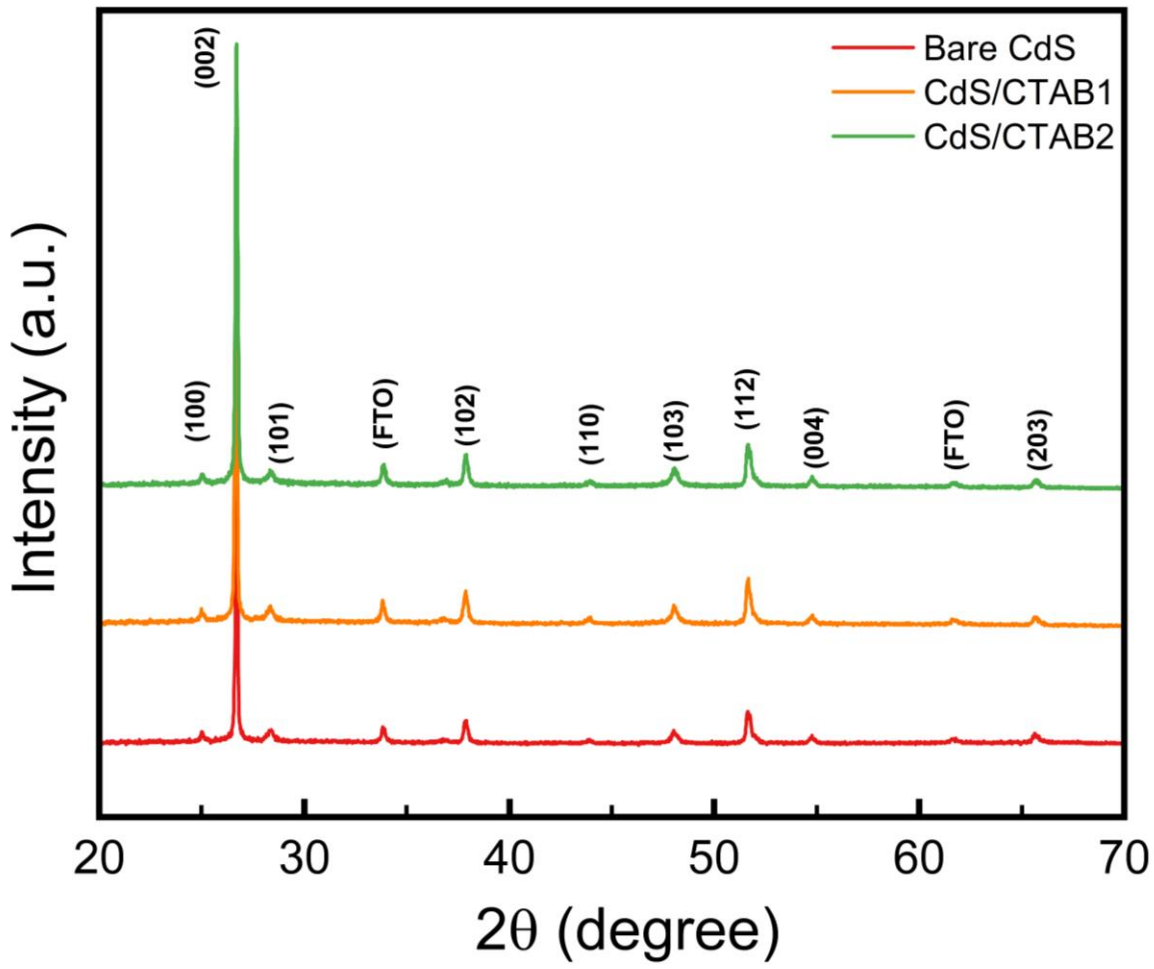

Figure 3A.2 *XRD spectra of bare CdS, CdS/CTAB1, and CdS/CTAB2.*

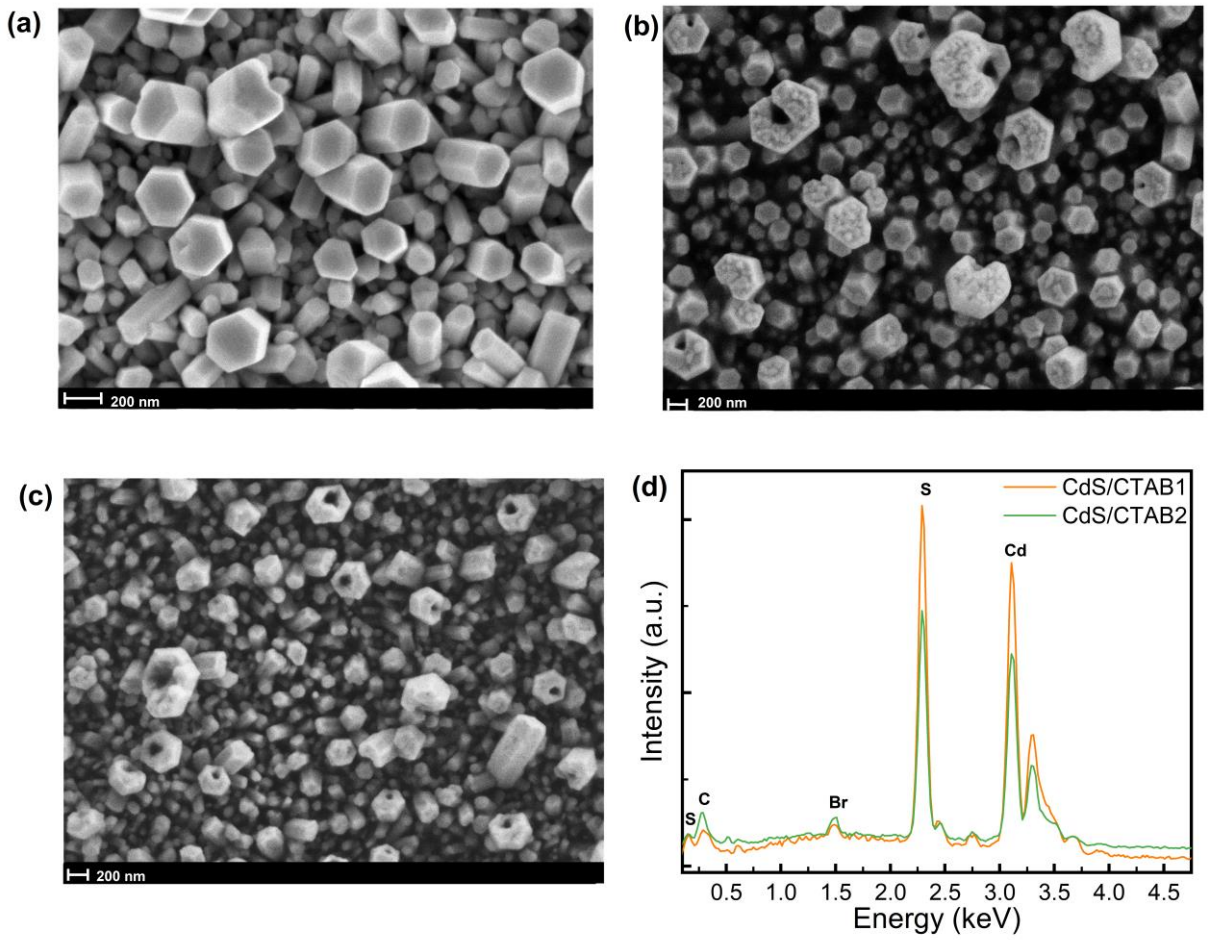

Figure 3A.3 *FESEM images of (a) bare CdS, (b) CdS/CTAB1, and (c) CdS/CTAB2. EDS spectra of (d) CdS/CTAB1 and (e) CdS/CTAB2.*

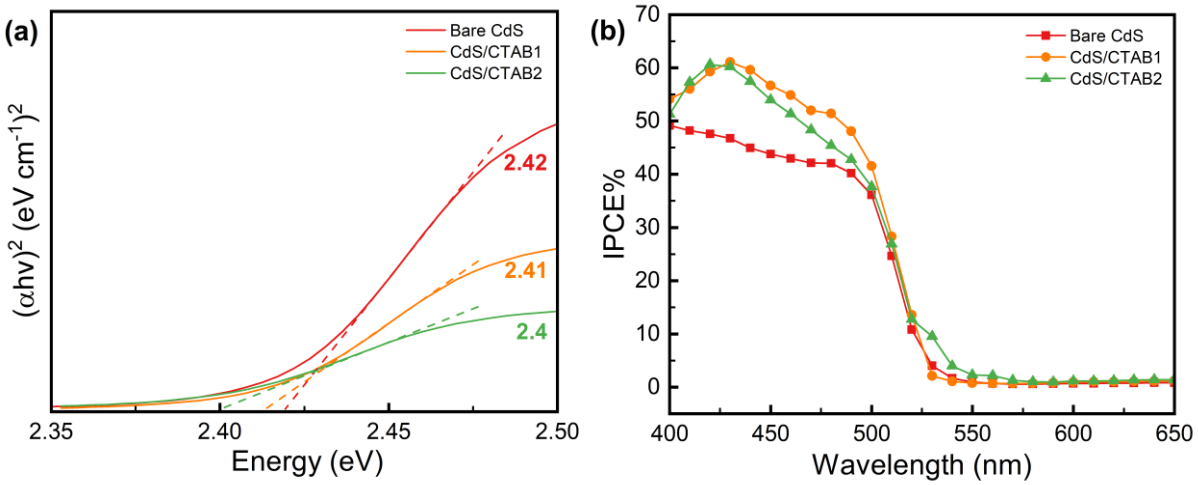

Figure 3A.4 *Tauc plots and IPCE efficiencies of (a) bare CdS, (b) CdS/CTAB1, and (c) CdS/CTAB2.*

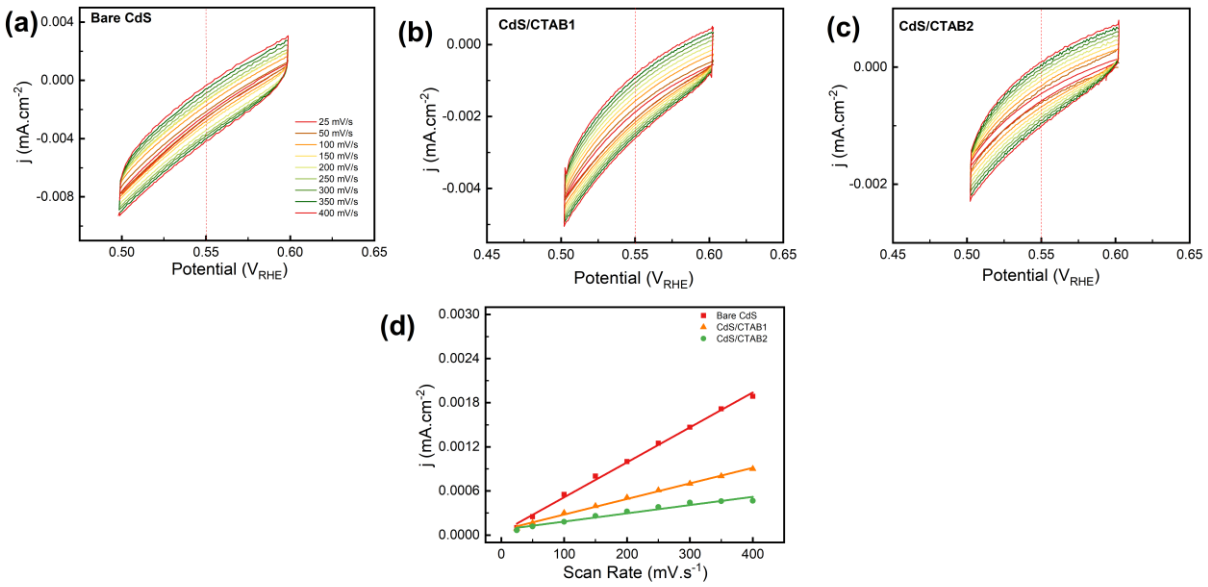

Figure 3A.5 *CV measurements at different scan rates of (a) bare CdS, (b) CdS/CTAB1 and (c) CdS/CTAB2. (d) ECSA plots of the photoanodes.*

The voltammograms shown in Figure 3A.6 below were used to calculate η_{inj}.

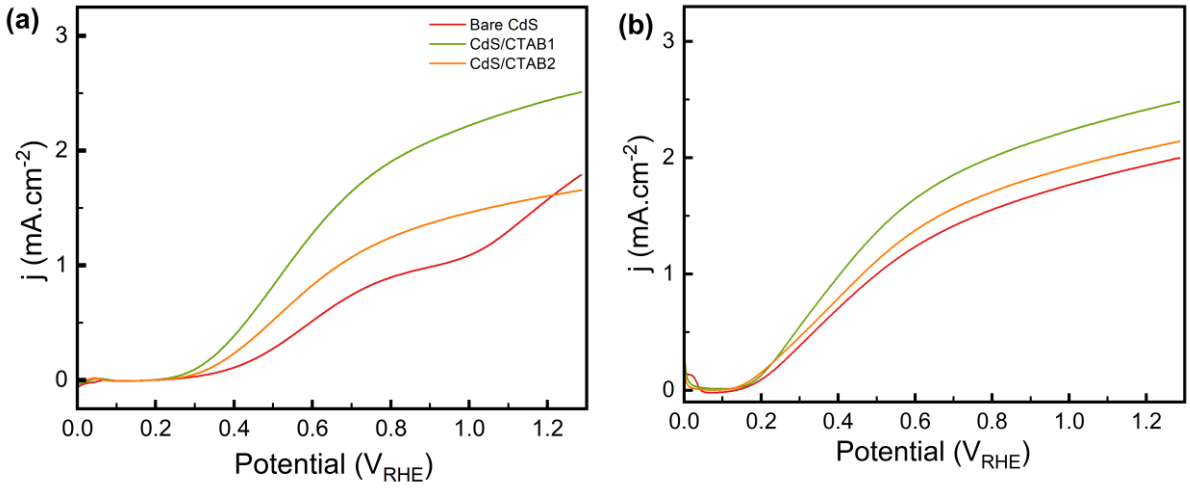

Figure 3A.6 *LSV of bare CdS, CdS/CTAB1, and CdS/CTAB2 in (a) 0.1M NaOH and (b) 0.1M NaOH / 0.25 M Na_2SO_3. Measurements were performed with a 50 $mV.s^{-1}$ potential scan rate under continuous illumination.*

Nyquist plots were fitted using Randles model given in Figure 3A.7a. In this model, R_S is the resistance of the electrolyte, R_{CT} is the charge transfer resistance at the photoanode/electrolyte interface, and CPE is the constant phase element to represent the imperfect capacitive behavior of CdS [172]. R_{CT} values in Figure 3.3 were determined from the second x-intercept of the Nyquist plots shown in Figure 3A.7b, c, and d.

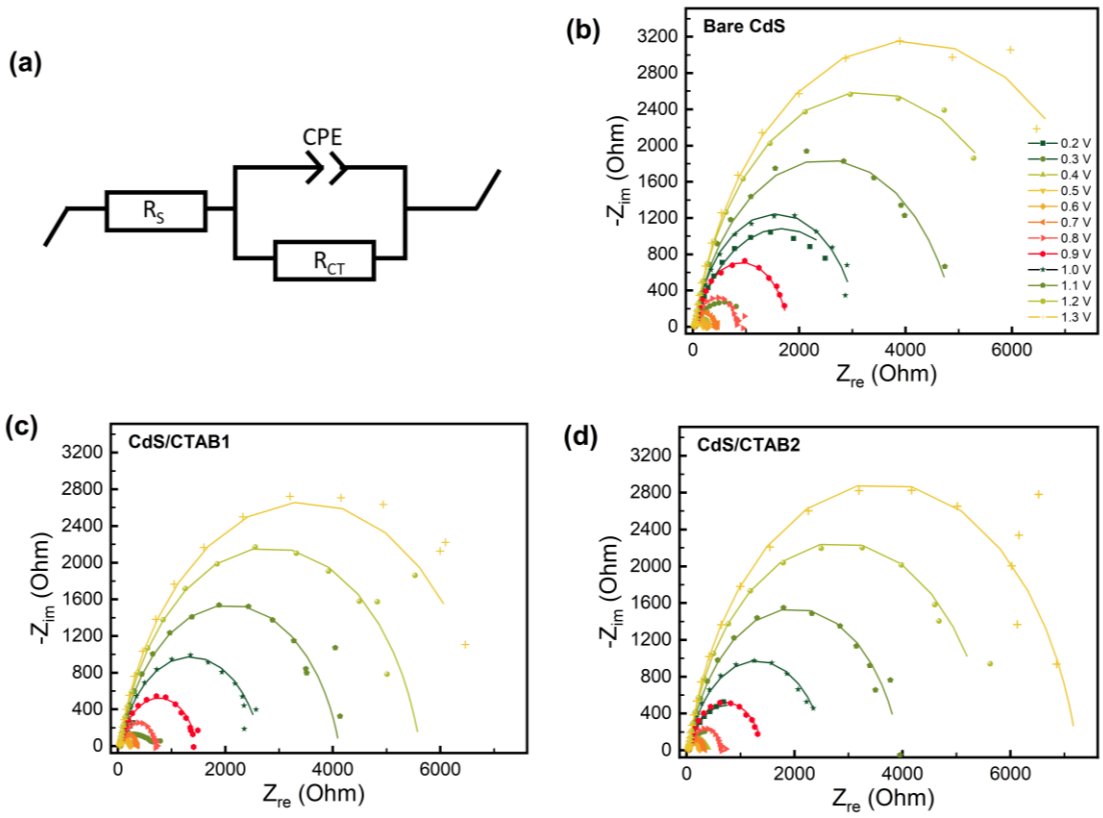

Figure 3A.7 *(a) Randles model circuit used for Nyquist plot fittings of bare CdS, CdS/CTAB1, and CdS/CTAB2. EIS fittings of (b) bare CdS, (c) CdS/CTAB1, and (d) CdS/CTAB2.*

Table 3A.1 *Potential versus R_{CT} data of bare CdS, CdS/CTAB1, and CdS/CTAB2.*

Potential (V_{RHE})	R_{CT} (Ohm)		
	Bare CdS	CdS/CTAB1	CdS/CTAB2
0.2	3270	2260	1496
0.3	1170	570	671
0.4	400	270	400
0.5	157	172	224
0.6	245	202	216
0.7	425	360	314
0.8	842	750	630
0.9	1740	1516	1353
1.0	3056	2600	2449
1.1	4939	4052	3873
1.2	6504	5453	5534
1.3	8105	6900	7116

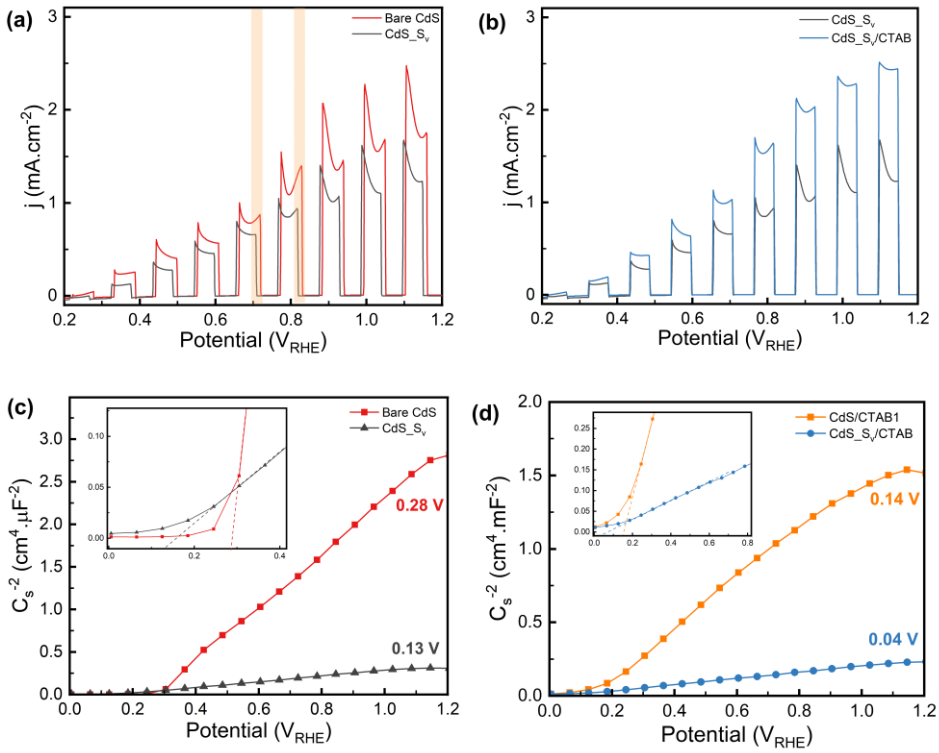

Figure 3A.8 *Chopped light LSV of (a) bare CdS after and CdS_Sv, (b) CdS_Sv and CdS_Sv/CTAB. MS plots of (c) bare CdS and CdS_Sv, (d) CdS/CTAB1 and CdS_Sv/CTAB.*

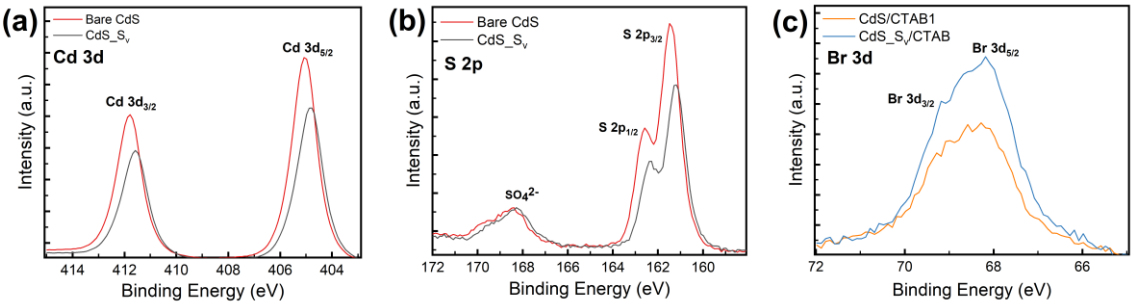

Figure 3A.9 *(a) Cd 3d and (b) S 2p spectra of bare CdS and CdS_Sv, and (c) Br 3d spectra of CdS/CTAB1 and CdS_Sv/CTAB.*

Table 3A.2 *Surface sulfur vacancy content of bare CdS and CdS_Sv calculated by Cd and S atomic percent on the surface.*

Sample	S atomic %	Cd atomic %	S_v
Bare CdS	49.97	50.03	0.001
CdS_Sv	49.25	50.74	0.029

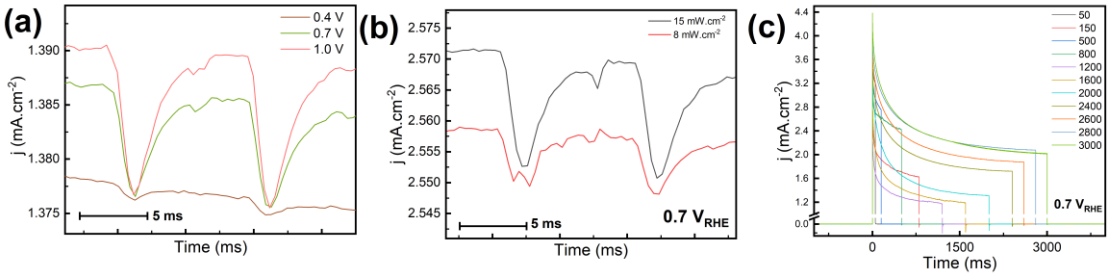

Figure 3A.10 *TPC of bare CdS at different illumination times by LED light at 0.7 V.*

Appendix B: Supporting Information for Chapter 4

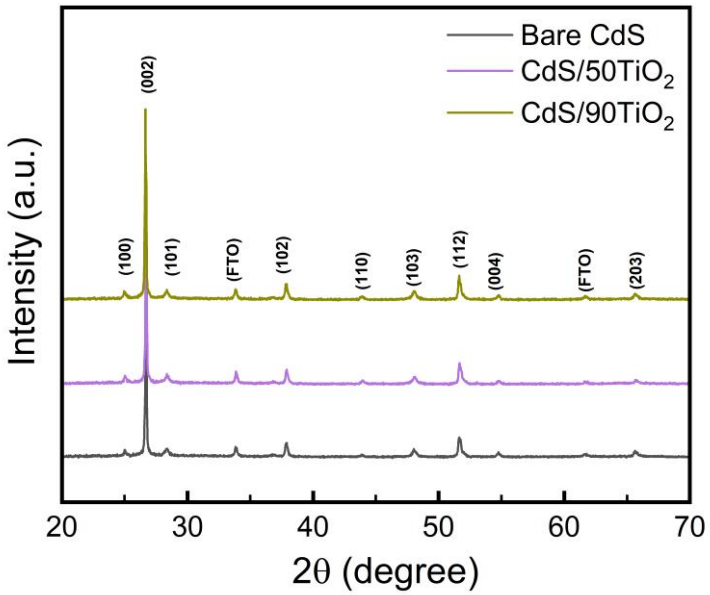

Figure 4B.1 *XRD spectra of bare CdS, CdS/50TiO₂, and CdS/90TiO₂.*

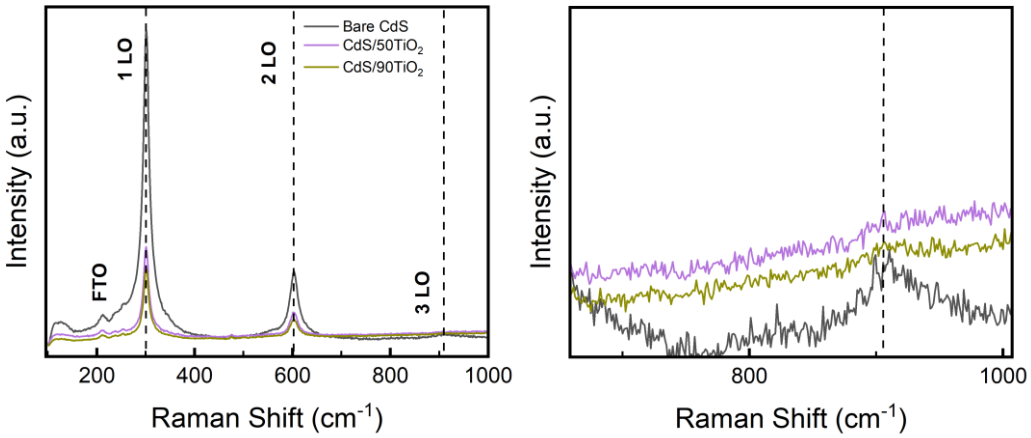

Figure 4B.2 *(a) Raman spectra of bare CdS, CdS/50TiO₂, and CdS/90TiO₂, and (b) inset of 3LO.*

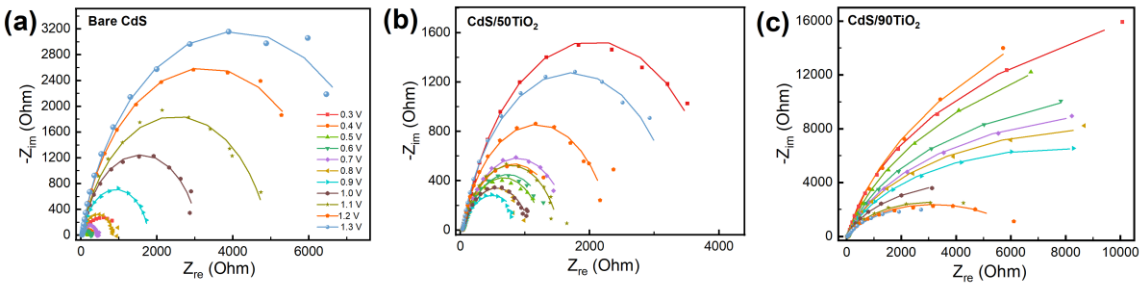

Figure 4B.3 *Potential dependent Nyquist fittings of (a) bare CdS, (b) CdS/50TiO₂, and (c) CdS/90TiO₂.*

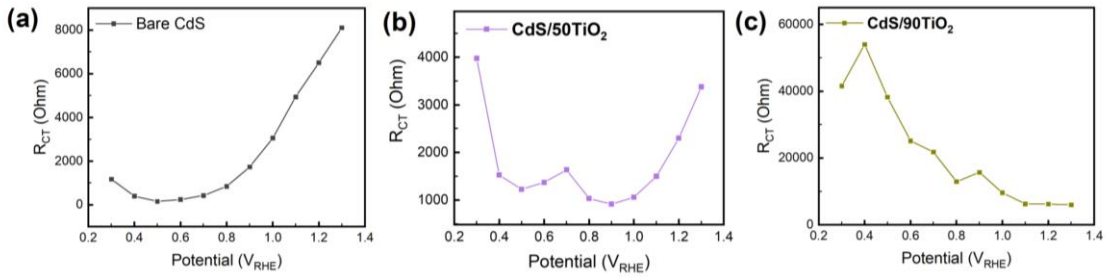

Figure 4B.4 *R_{CT} versus potential plots of (a) bare CdS, (b) CdS(50TiO_2, and (c) CdS/90TiO_2.*

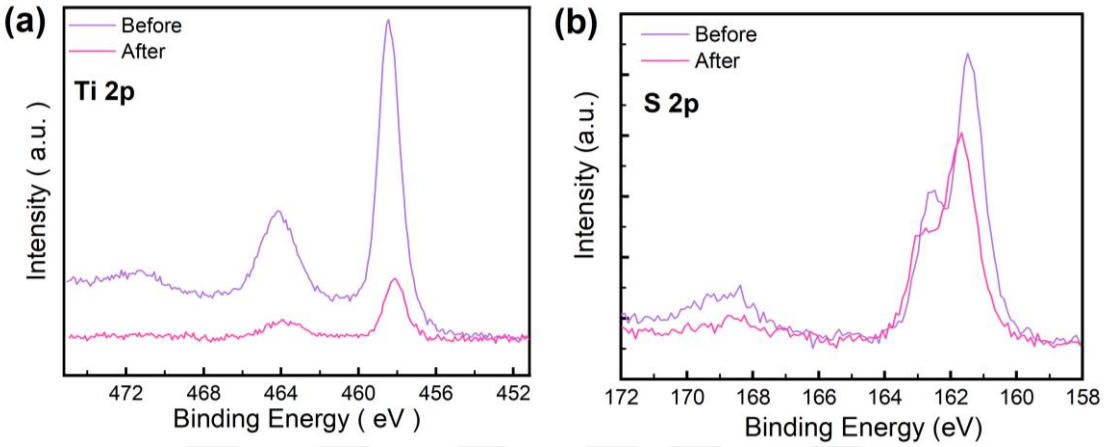

Figure 4B.5 *(a)Ti 2p and (b)S 2p XPS spectra of CdS/50TiO_2 before and after consecutive front illumination LSV measurements.*

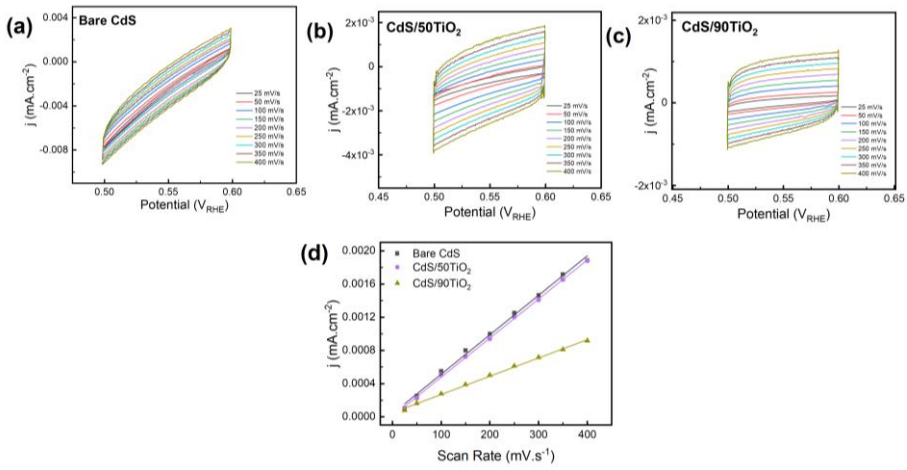

Figure 4B.6 *CV of (a)bare CdS, (b)CdS/50TiO_2, (c) CdS/90TiO_2 at different scan rates and (d) ECSA comparison.*

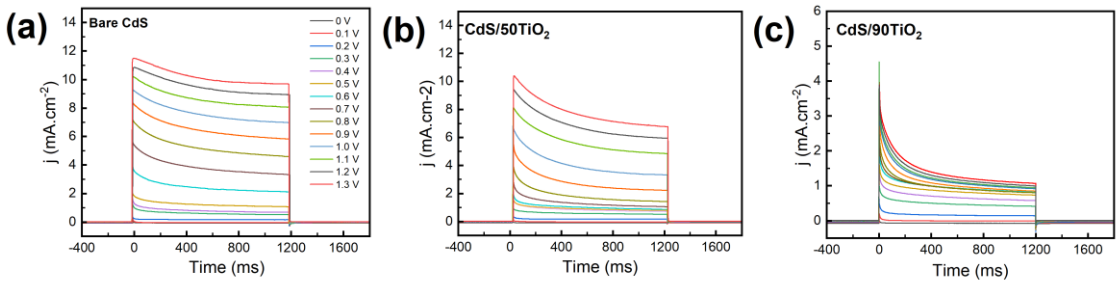

Figure 4B.7 *Potential dependent 1200 ms light pulse TPC measurements of (a) bare CdS, (b) CdS(50TiO₂, and (c) CdS/90TiO₂.*

Appendix C: Supporting Information for Chapter 5

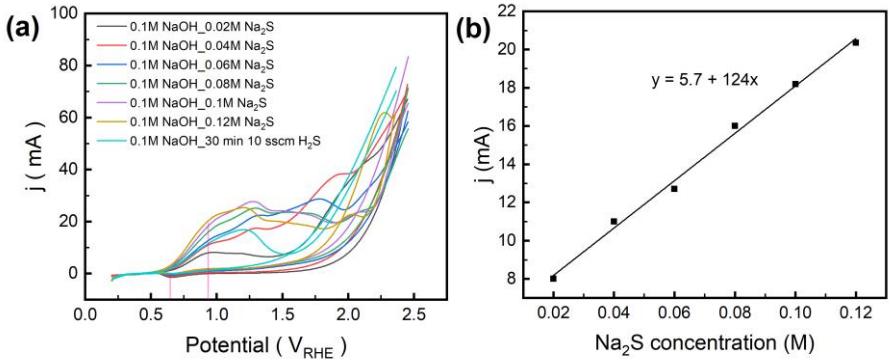

Figure 5C.1 *(a) CV scans of electrolytes with different Na_2S concentrations in 0.1 M NaOH and 30 min H_2S feeded 0.1 M NaOH, (b) calibration curve obtained by dissolved Na_2S concentration versus current at 0.94 V during anodic scan.*

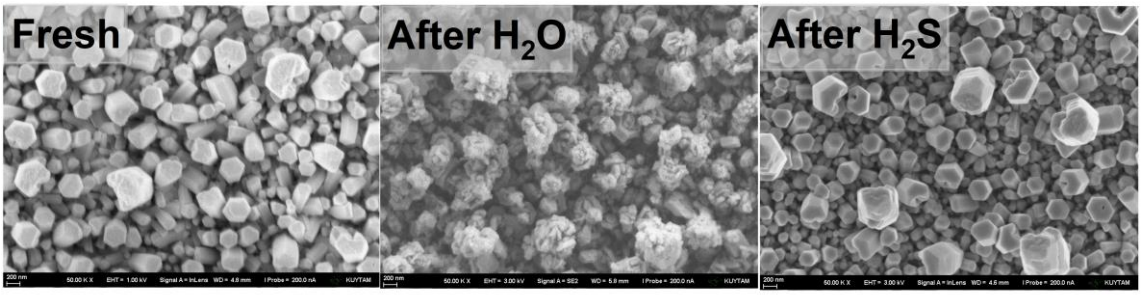

Figure 5C.2 *FESEM images of fresh CdS and CdS after CA experiment at 0.8 V in 0.1M NaOH and 0.1M NaOH/ H_2S electrolytes.*

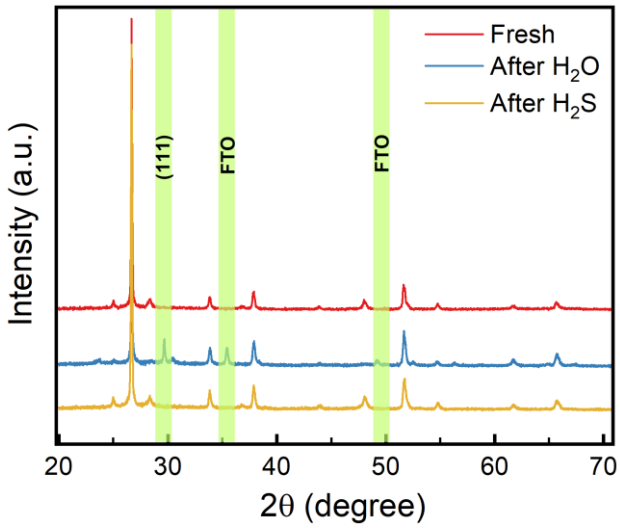

Figure 5C.3 *XRD spectra of fresh CdS and CdS after CA experiment at 0.8 V in 0.1M NaOH and 0.1M NaOH/H_2S electrolytes.*

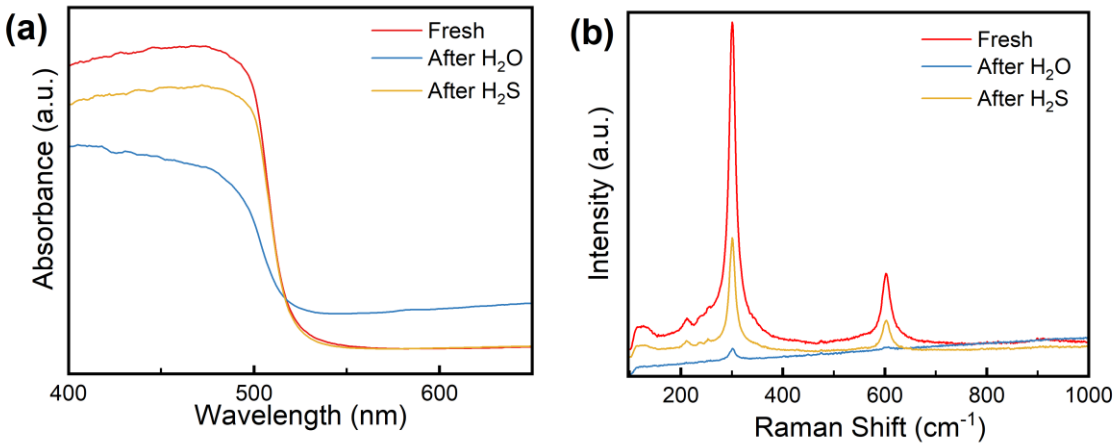

Figure 5C.4 *(a)UV-Vis and (b)Raman spectra of fresh CdS and CdS after CA experiment at 0.8 V in 0.1M NaOH and 0.1M NaOH/ H_2S electrolytes.*

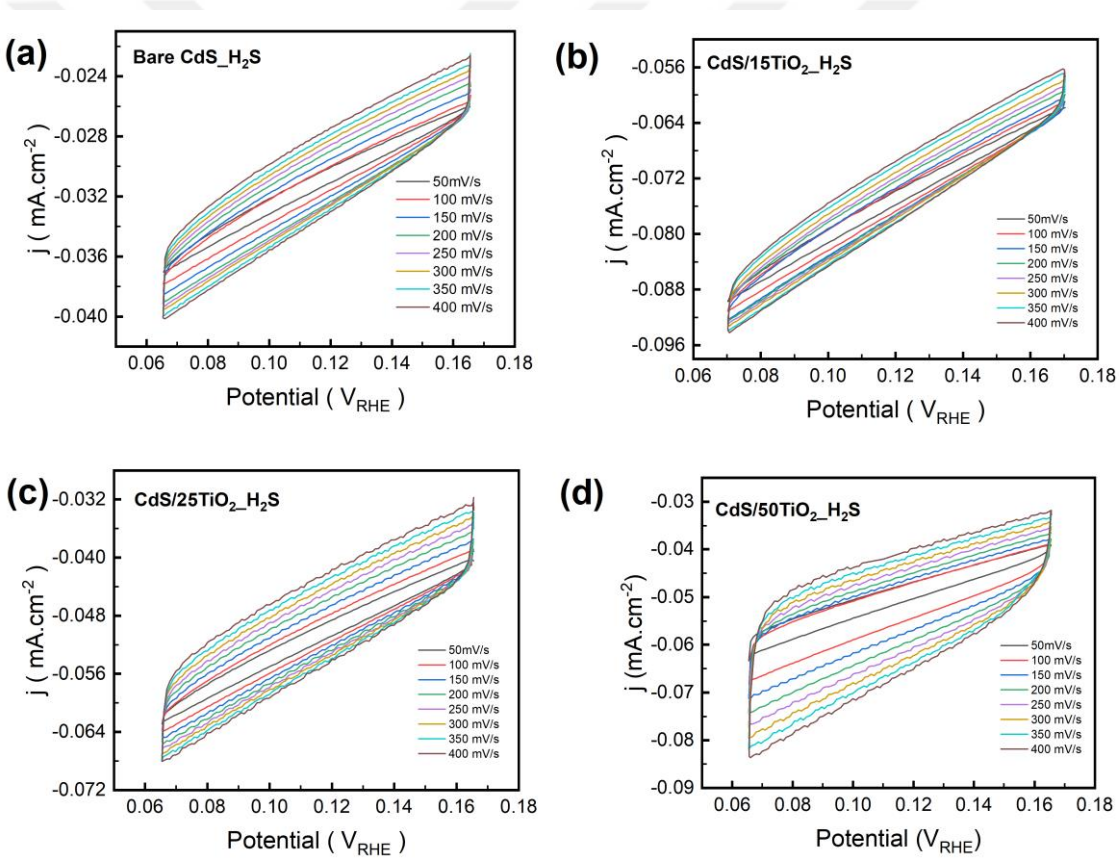

Figure 5C.5 *CV scans of (a) Bare CdS, (b) CdS/15TiO_2, (c) CdS/25TiO_2, (d) CdS/50 TiO_2 in 0.1M NaOH/H_2S.*

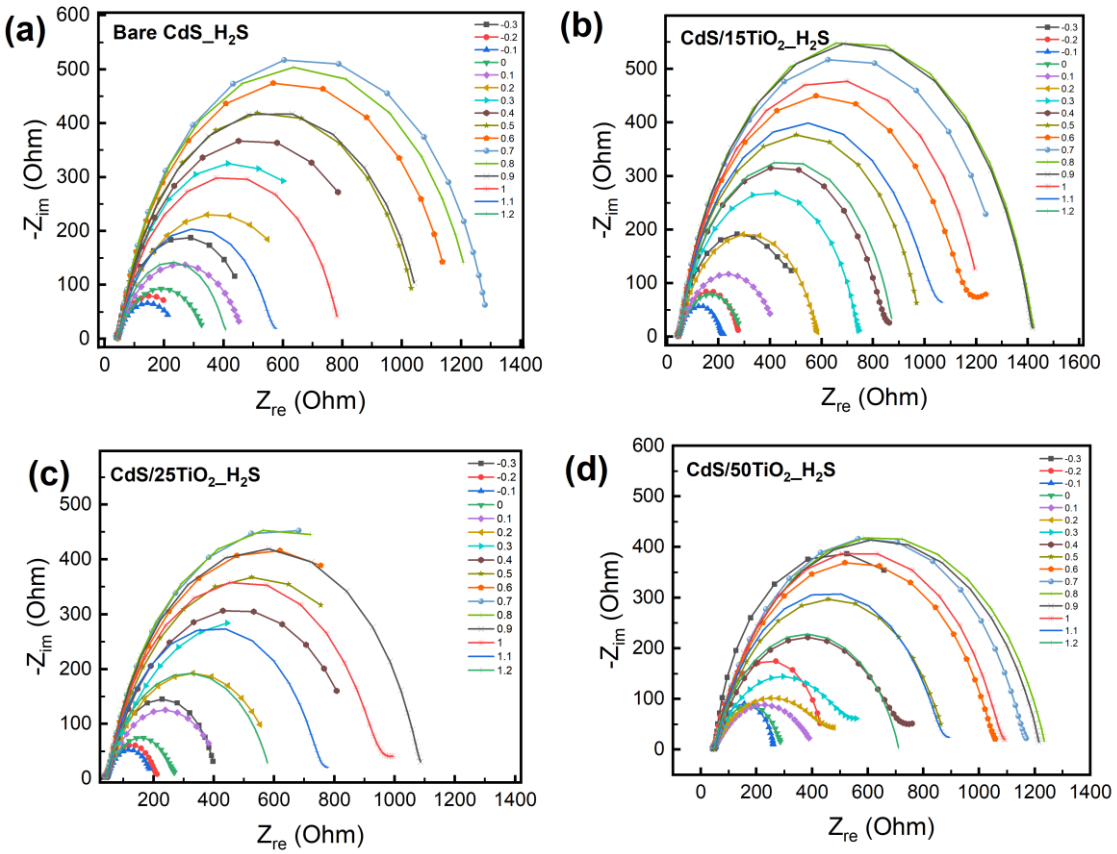

Figure 5C.6 *Nyquist fittings of (a) bare CdS, (b) CdS/15TiO$_2$, (c) CdS/25TiO$_2$, (d) CdS/50 TiO$_2$ in 0.1M NaOH/H$_2$S at different potentials.*